

**PROCESSING AND PROPERTIES OF MULTIPHASE IRON**

**ALUMINIDE AND IRON-IRON ALUMINIDE**

**COMPOSITES BY P/M ROUTES**

A Thesis Submitted

In Partial Fulfilment of the Requirements

For the Degree of

**MASTER OF TECHNOLOGY**

BY

**MANASIJ KUMAR YADAVA**

To The

DEPARTMENT OF MATERIALS AND METALLURGICAL ENGINEERING

INDIAN INSTITUTE OF TECHNOLOGY, KANPUR

AUGUST , 1999

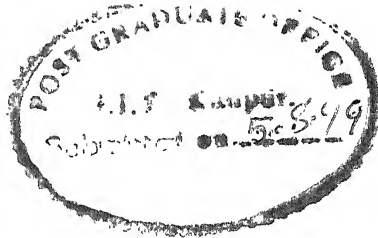
2 MAR 2000 (MME  
U.S. LIBRARY  
I.I.T. KANPUR  
A 130443

2000

2000

2000

## CERTIFICATE



This is to certify that the thesis entitled, PROCESSING AND PROPERTIES OF MULTIPHASE IRON ALUMINIDE AND IRON-IRON ALUMINIDE COMPOSITES BY P/M ROUTES , is the record of the work carried out by MANASIJ KUMAR YADAVA under my supervision and has not been submitted else where for the award of a degree.



(Prof. S. Bhargava)

Department of Materials and Metallurgical Engineering  
Indian Institute of Technology  
Kanpur

August ,1999

**DEDICATED**

**TO**

***SATYAM***

## ACKNOWLEDGEMENTS

I would like to express my deep sense of gratitude and indebtedness to Prof. S. Bhargava for his valuable guidance, encouragement and inspirational discussions throughout the course of this investigation. It has truly been a learning experience to associate with him and work towards the completion of this work.

I am indebted to Prof. R. K. Ray for his moral support.

I am extremely thankful to Dr. S. Suwas for whole-heartedly extending his valuable time as well as encouraging moral support during the course of this thesis.

I have no words to thank Kumar ji for the care he has taken of me throughout the period of my thesis work.

I am grateful to Umashankar ji, Mr. B. Shrama, Dr. M. N. Mungole, Srivastava ji, Malhotra ji and all staffs of MME dept. for their assistance in the experimental work.

I can not forget association and cooperation of my friends Vineet, Sanjit, Patro and specially Lahiri , without whose name my thesis is incomplete.

December 1<sup>st</sup> 1999  
I.I.T. Kanpur

(Manasij Kumar Yadava)

## CONTENTS

### Chapter

1	INTRODUCTION	1
2	LITERATURE REVIEW	3
2.1	Intermetallics	3
2.2	Aluminides	5
2.3	Iron Aluminides	9
2.3.1	Iron-Aluminium Binary System	
2.3.1.1	Phase Diagram	
2.3.1.2	Crystal Structure	
2.3.2	Defects in Ordered Fe-Al Intermetallics	
2.3.3	Properties of Ordered Fe-Al Alloys	
2.3.3.1	Crystallography of Slip and Twinning	
2.3.3.2	Strength	
2.3.3.3	Work Hardening	
2.3.3.4	Ductility	
2.3.3.5	Fracture	
2.3.3.6	Creep and Fatigue	
2.3.3.7	Weldability & Corrosion Resistance	

## 2.3.4 Ternary Additions to Iron Aluminides

2.4 Processing Routes for Iron Aluminids 34

### 2.4.1 Ingot Metallurgy Route

2.4.1.1 Melting

2.4.1.2 Casting

2.4.1.3 Mechanical Working

### 2.4.2 Powder Metallurgy Route

2.4.2.1 Powder Metallurgical

Processes Based on

Elemental Powders

2.4.2.2 Powder Metallurgical

Processes Based on

Pre Alloyed Powders

3 EXPERIMENTAL PROCEDURE 44

3.1 Starting Material 44

3.1.1 Iron Powder

3.1.2 Iron Aluminide Powder

3.2 Reduction of Iron Powder 48

3.3 Cold Compaction and Sintering of Iron and Iron Aluminide  
Powder Mixture 51

3.3.1 Cold Compaction

3.3.2 Sintering of Green Compacts

3.4 Hot Rolling of Sintered Compacts 51

3.5	Hot Pressing of Iron-Iron Aluminide Powder Mixture	52
3.6	Characterization of Powders, Sintered and Hot Pressed Samples	54
	3.6.1 X-ray Diffraction Analysis	
	3.6.2 Scanning Electron Microscopy	
	3.6.3 Density Measurements	
	3.6.4 Hardness Testing	
	3.6.5 Compression Testing	
	3.6.6 Electron Probe Micro Analysis	
4	RESULTS AND DISCUSSION	56
4.1	Identification of Phases in The Starting Iron Aluminide Powder	56
4.2	Cold Compaction Behaviour of Iron Aluminide & Iron-Iron Aluminide Powder Mixture	59
	4.2.1 Compaction behaviour of Iron Aluminide Powder	
	4.2.2 Effect of Iron Addition	
	4.2.3 Effect of Pressure	
4.3	Sintering of Iron-Iron Aluminide Green Compacts	66
	4.3.1 Microstructural Evolution during Sintering	
	4.3.2 Hardness of Sintered Compacts	
4.4	Hot Pressing of Iron Aluminide and Iron-Iron Aluminide Powder Mixture	82
	4.4.1 General	

4.4.2 Identification of Phases Formed During Hot  
Pressing

4.4.3 Densification and Microstructural Evolution  
during Hot Pressing

4.4.4 Compressive Strength of Hot Pressed  
Samples

5	CONCLUSIONS	119
6	SUGGESTIONS FOR FUTURE WORKS	122
	REFERENCES	123

## LIST OF FIGURES

Figure 2.1 Crystal structures of some ordered intermetallics.

Figure 2.2 Fe-Al binary phase diagram.

Figure 2.3 Crystal structures of FeAl and  $Fe_3Al$  phases.

Figure 2.4 Unit cell and antiphase vectors associated with B2 FeAl.

Figure 2.5 Dislocation configuration in ordered Fe-Al alloys.

Figure 2.6 Effect of Al content on the yield strength and ductility of  $Fe_3Al$ .

Figure 2.7 Effect of temperature on yield strength of  $Fe_3Al$ .

Figure 2.8 Effect of temperature on yield stress of  $Fe_3Al$ , alloyed with Mo and Ti (with their respective transition temperatures).

Figure 2.9 Flow Chart of processing routes used to produce intermetallic parts.

Figure 2.10 Schematic diagram showing reactive sintering mechanism.

Figure 2.11 Effect of pressure on density in hot pressing of iron aluminides.

Figure 3.1 SEM micrograph of Fe powders.

Figure 3.2 Histogram showing size distribution of Fe powder.

Figure 3.3 SEM micrograph of iron aluminide powder.

Figure 3.4 Histogram showing size distribution of iron aluminide powders.

Figure 3.5 Schematic diagram of the arrangement made for reduction of Fe powder.

Figure 3.6 Schematic diagram showing the hot pressing unit used.

Figure 4.1 X-ray diffraction pattern of iron-aluminide powder.

Figure 4.2 Plot of relative density of green compact( $\rho_{rel}$ ) vs %Fe.

Figure 4.3 Plot of green density of compacts( $\rho$ ) vs %Fe .

Figure 4.4 Plot of density of fully dense material( $\rho_0$ ) vs %Fe.

Figure 4.5 Plot of relative density of green compacts( $\rho_{rel}$ ) vs compaction pressure.

Figure 4.6 Optical micrograph of Iron aluminide compact sintered at  $1100^0\text{C}$  for 1 hr.

Figure 4.7 Optical micrograph of Iron aluminide compact sintered at  $1200^0\text{C}$  for 1 hr.

Figure 4.8 Optical micrograph of Iron aluminide compact sintered at  $1200^0\text{C}$  for 2 hrs.

Figure 4.9(a) Optical micrograph of Iron(5%)-Iron aluminide compact sintered at  $1100^0\text{C}$  for 2 hrs.

Figure 4.9(b) Optical micrograph of Iron(5%)-Iron aluminide compact sintered at  $1100^0\text{C}$  for 3 hrs.

Figure 4.10(a) Optical micrograph of Iron(5%)-Iron aluminide compact sintered at  $1150^0\text{C}$  for 4 hrs.

Figure 4.10(b) Optical micrograph of Iron(5%)-Iron aluminide compact sintered at  $1200^0\text{C}$  for 2 hrs.

Figure 4.11(a) Optical micrograph of Iron(12%)-Iron aluminide compact sintered at  $1150^0\text{C}$  for 4 hrs.

Figure 4.11(b) Optical micrograph of Iron(5%)-Iron aluminide compact sintered at  $1200^0\text{C}$  for 2 hrs.

Figure 4.12 Optical micrograph of Iron(12%)-Iron aluminide compact sintered at  $1200^0\text{C}$  for 1 hr.

Figure 4.13 Variation of microhardness with time in samples with 12%Fe and sintered at  $1100^0\text{C}$ .

Figure 4.14 Variation of microhardness of Iron-Iron aluminide compacts sintered at  $1150^0\text{C}$  for 4 hrs with %Fe.

Figure 4.15 X-ray diffraction pattern of 50%Fe sample Hot pressed at  $650^0\text{C}$ .

Figure 4.16 X-ray diffraction pattern of 40%Fe sample Hot pressed at  $650^0\text{C}$ .

Figure 4.17 X-ray diffraction pattern of 30%Fe sample Hot pressed at  $700^0\text{C}$ .

Figure 4.18 X-ray diffraction pattern of 40%Fe sample Hot pressed at  $700^0\text{C}$ .

Figure 4.19 X-ray diffraction pattern of 15%Fe sample Hot pressed at  $800^0\text{C}$ .

Figure 4.20 X-ray diffraction pattern of 40%Fe sample Hot pressed at  $800^0\text{C}$ .

Figure 4.21 Full density optical micrograph of 10%Fe sample Hot pressed at  $800^0\text{C}$ .

Figure 4.22 Full density scanning electron micrograph of 15%Fe sample Hot pressed at  $800^0\text{C}$ .

Figure 4.23 Full density optical micrograph of 40%Fe sample Hot pressed at  $800^0\text{C}$ .

Figure 4.24 Optical micrographs of 10%Fe sample hot pressed at  $800^0\text{C}$  in different regions

Figure 4.25 Micrographs of Hot pressed sample showing advanced stages of densification during hot pressing at  $800^0\text{C}$ :

- Optical micrograph of 40%Fe sample.
- Scanning micrograph of 15%Fe sample.
- Scanning micrograph of 15%Fe sample.
- Scanning micrograph of 40%Fe sample.

Figure 4.26(a) Scanning micrograph of 40%Fe sample Hot pressed at  $800^0\text{C}$  showing lamellar microstructure.

Figure 4.26(b) Similar micrograph as 4.26(a) but taken on EPMA at lower magnification.

Figure 4.27 Scanning micrograph of 15%Fe sample Hot pressed at  $800^0\text{C}$  showing

lamellar microstructure.

Figure 4.28 An EPMA micrograph of 40% Fe sample(Hot pressed at  $800^0\text{C}$ ) showing typical trace of electron probe.

Figure 4.29(a) Plot showing variation of %Al in the 15%Fe sample(Hot pressed at  $800^0\text{C}$ ) around lamellar region.

Figure 4.29(b) Plot showing variation of %Al in 40%Fe sample (Hot pressed at  $800^0\text{C}$ ) around lamellar region.

Figure 4.30(a) EDAX dot map showing distribution of Al in 40% sample.

Figure 4.30(b) EDAX dot map showing distribution of Fe in 40% sample.

Figure 4.31 Plots showing variation of %Al in 40%Fe sample((Hot pressed at  $800^0\text{C}$ ) in non lamellar region in two mutually perpendicular direction.

Figure 4.32 Compression test results of hot pressed samples.

Figure 4.33 Plot showing compression strength variation with %Fe for two different temperatures of hot pressing.

Figure 4.34(a) Scanning electron photograph showing fracture surface in 20%Fe Sample hot pressed at  $700^0\text{C}$ .

Figure 4.34(b) Scanning electron photograph showing fracture surface in 50%Fe Sample hot pressed at  $700^0\text{C}$ .

## LIST OF TABLES

Table 2.1 Applications of Intermetallics.

Table 2.2 Applications of Aluminides.

Table 2.3 Important aluminides and their properties.

Table 2.4 Crystal structure data of iron aluminide intermetallic compounds.

Table 2.5 Lattice parameters of iron aluminides.

Table 2.6 Modes of failure of Fe-Al alloys.

Table 2.7 Reaction chemistry in Fe-Al alloys.

Table 4.1 First five high intensity peaks of intermetallic phases in Fe-Al system.

Table 4.2 Density of green compacts of varying iron contents.

Table 4.3 Densities of green compacts with 50%Fe under different compaction pressures.

Table 4.4 X-ray diffraction results of Hot pressed samples.

Table 4.5 Compression strength of hot pressed samples.

## ABSTRACT

Iron-aluminium binary system contains several aluminides, which are found to be attractive from the point of view of several engineering applications. These aluminides are, however, brittle in nature and therefore production of components from them requires novel processing routes to be developed. The present study is aimed to process single/multi-phase iron aluminide(s) and iron-iron aluminide composites by a P/M route. Thus a prealloyed iron aluminide powder comprising  $Fe_2Al_5$  and  $FeAl_2$  phases was mixed with up to 50 wt% of pure iron powder and was processed via cold compaction-sintering and hot pressing routes under different processing conditions. The iron addition was found to improve the compressibility of iron aluminide powder and also resulted in higher relative density of green compacts. Sintering behaviour of compacts with no iron addition was found to be poor even at temperature as high as 0.94  $T_m$  but improved considerably by the addition of iron. On the other hand, hot pressing was found to be a more suitable route for the preparation of fully dense microstructures of single/multi-phase iron aluminide and iron-iron aluminide composites. While iron-iron aluminide composites were produced from powder mixtures containing up to 50 wt% Fe by their hot pressing up to 700°C, single-phase  $FeAl$  compacts with full density microstructures were produced by hot pressing of 15 wt% Fe-iron aluminide powder mixture at the temperature of 800°C. Moreover,  $FeAl_2$ - $FeAl$  two-phase iron aluminide structures were obtained by the hot pressing of 40 wt% Fe-iron aluminide powder mixture by hot pressing

at the temperature of  $800^{\circ}\text{C}$ . Hot pressing at  $700^{\circ}\text{C}$  provided better compressive strength to iron-iron aluminide composites of all compositions than those obtained by hot pressing at  $650^{\circ}\text{C}$ . Similarly, the compressive strength as well as the toughness of composites was found to be increasing with increase in the iron content of the initial powder mixture.

## CHAPTER 1

### INTRODUCTION

Among the intermetallic compounds aluminide intermetallics are of much interest for future high temperature applications. This is primarily due to the benefits gained from their much lower densities and ability to withstand high temperature and corrosive environments as compared to existing alloys. Iron-aluminium binary system entails five stable intermetallic phases and three two phase regions in different composition ranges. Much of the work done on iron aluminides has been focussed on only FeAl (B2) and  $Fe_3Al$  (DO<sub>3</sub>) single phase materials. Though several two phase regions are present in iron aluminium system, very little work has been done to process such materials and to study the processing-structure-properties relationships existing in such materials.

It has also been established that as %Al in iron aluminides increases, their brittleness increases and hence it is difficult to process two phase iron aluminide alloys by the conventional ingot metallurgy (I/M) routes. In contrast, routes based on powder processing offer the possibility of synthesizing such intermetallic alloys. Also if powder based routes have to be adopted they can also be utilised for the preparation of various multiphase aluminide based composites.

It is worth mentioning that such multiphase iron aluminides have been synthesized from elemental Fe and Al powders by the reactive sintering (RS) /reactive hot pressing (RHP) routes. In contrast, the present study for synthesizing multiphase iron aluminide and iron- iron aluminide composites, involves pre-alloyed iron aluminide and iron powders.

Chapter two of the thesis briefly summarizes the literature on iron-aluminides, their properties & processing routes and ends with aims of present study. Details of the experimental procedure adopted have been presented in chapter three. Results obtained from the present study are discussed in chapter four. Conclusions from present study have been summarized in chapter five.

## CHAPTER 2

### LITERATURE REVIEW

#### 2.1 INTERMETALLICS

Materials having high strength with the promise of sustainability at high temperatures have always been the prime focus of research in 20<sup>th</sup> century. This search for high temperature structural materials has stimulated much interest in the ordered intermetallics. Ordered intermetallics constitute an unique class of metallic materials that form long-range-ordered crystal structure (Figure 2.1)<sup>[2]</sup> below a critical temperature that is generally referred to as the critical ordering temperature ( $T_c$ )<sup>[1]</sup>. These compounds are phases, which occur in the central part of the phase diagram between two or more metals with a characteristic crystal structure, and may have a very specific composition or a range of composition. Because of the strong attraction between the unlike atoms involved, there is strong preference in the selection of nearest neighbours which in turn can lead to an ordered structure, a high resistance to deformation i.e. movements of lattice defects, and high melting point. The high melting point in combination with the difficulty of movements of lattice defects, leads to high strength and retention of strength to elevated temperatures. However, these same features, lead to very low ductility i.e. brittleness at ambient temperatures<sup>[11-13]</sup>. Various techniques have been used to get rid of this brittleness problem, though

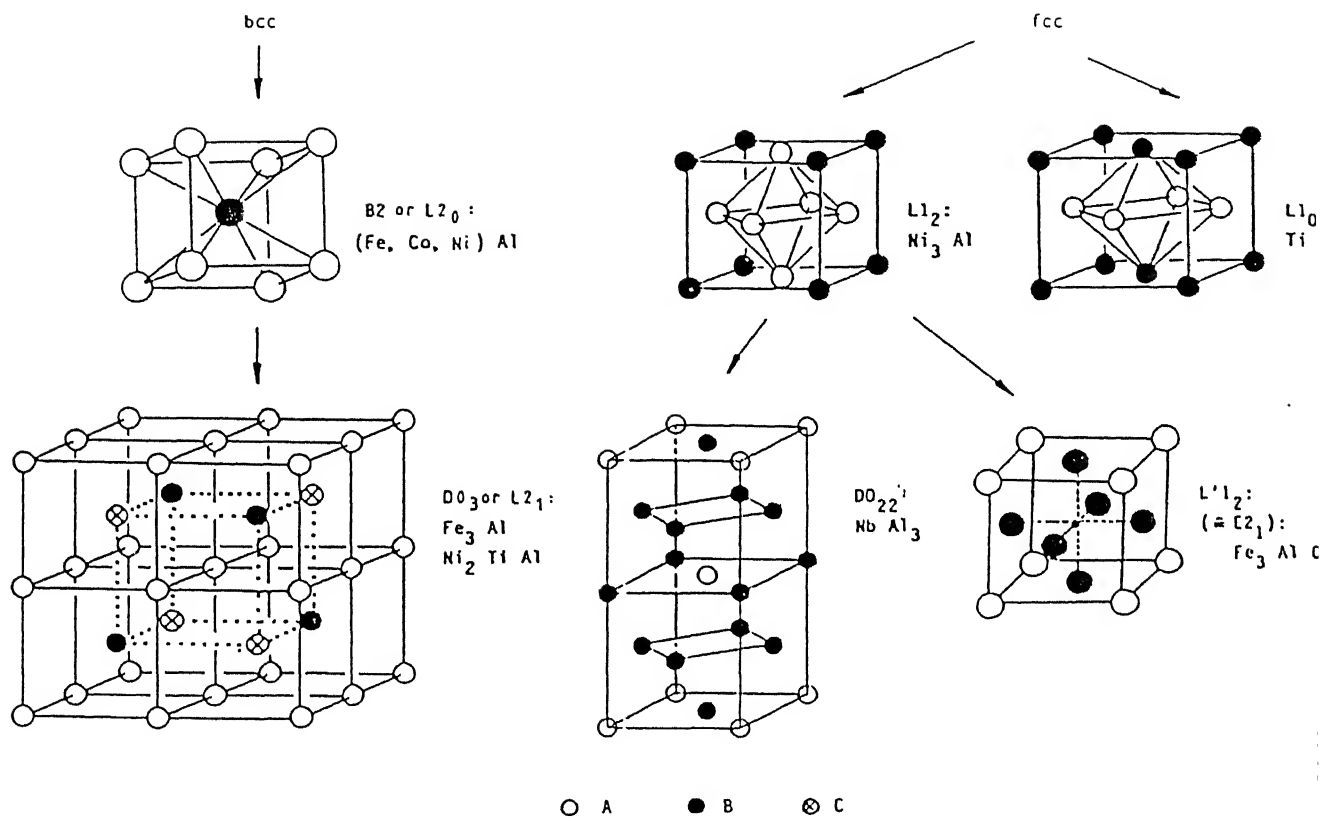


Figure 2.1: Crystal structures of some ordered intermetallic compounds

still retaining their high temperature properties. This has been achieved to an extent using composition /processing /microstructural control and by use of composite concepts in which a ductile phase is incorporated into the intermetallic matrix to deflect crack propagation, and in this way to increase toughness.

Ordered Intermetallic alloys can be divided into several groups, e.g. Aluminides ( e.g. Iron, Nickel, Titanium), Trialuminides (e.g.  $TiAl_3$ ,  $ZrAl_3$ ,  $FeAl_3$  etc.), Berylides ( $NbBe_{12}$ ), Chromides ( $Cr_2Ti$ ) etc. Some applications of intermetallics are shown in table 2.1a and 2.1b<sup>[2]</sup>.

## 2.2 ALUMINIDES

Among intermetallic compounds, aluminides, specifically Iron, Nickel and Titanium aluminides have been the focus of much of the research. These aluminides possess many attributes that make them attractive for high temperature applications (Table 2.2). They contain enough aluminium to form, in oxidizing environments, thin film of aluminium oxide ( $Al_2O_3$ ), that often are compact and protective<sup>[14,15]</sup>. Aluminides have low density (due to presence of lighter aluminium in sufficiently high proportion), relatively high melting points, and good high temperature strength properties (Table 2.3). But like other ordered intermetallics, they also exhibit brittle fracture and low ductility at room temperatures. Poor fracture resistance and limited fabricability restrict the use of aluminides as engineering materials<sup>[1,3-5]</sup>. In recent years, alloying and processing have been employed to control the ordered crystal structure, microstructural features, grain boundary structures

**Table 2.1: Some applications of intermetallic phases.**

**Table 2.1a In past centuries**

Phase	Application	Since about
$\text{Cu}_3\text{As}$	coating of bronze (Egypt)	2500B.C.
$\text{Cu}_{31}\text{Sn}_8$	mirrors (China)	0
$\text{Sn}_8\text{Hg}$	mirror surface (Venice)	1500
$\text{Ag}_2\text{Hg}_3 + \text{Sn}_6\text{Hg}$	dental amalgam (China)	600
$\text{Cu}_4\text{Hg}_3$	dental amalgam (Germany)	1500
$\text{SbSn}$	type metal	1540

**Table 2.1b In this century**

Phase	Application	Since about
$\text{Ni}_3\text{Fe}$	high permeability magnetic Alloy (Permalloy)	1920
$\text{FeCo}(-2\text{V})$	soft magnetic alloy (Permendure)	1930
$\text{Fe}_3(\text{Si},\text{Al})$	magnetic head material (Sendust)	1935
$\text{SmCo}_5$	permanent magnets	1970
$\text{Nb}_3\text{Sn}$	A 15-superconductor	1965
$\text{CuZnAl}$ , $\text{CuNiAl}$	shape memory alloys	1960
$\text{NiTi}$	shape memory alloys (Nitinol)	1965
$\text{MoSi}_2$	heater elements (Mosilit, Super-Kanthal)	1955
$\text{NiAl}$ , $\text{CoAl}$	protective coatings	1965

Table 2.2 : Applications of Structural Intermetallics

---

$\text{Ni}_3\text{Al}$	<ul style="list-style-type: none"><li>- Diesel - engine turbocharger rotors;</li><li>- High - temperature dies and molds;</li><li>- Air craft parts;</li><li>- Turbine blades;</li><li>- Hydro turbines;</li></ul>
$\text{Fe}_3\text{Al}$	<ul style="list-style-type: none"><li>- Toasters, stoves, Ovens;</li><li>- Automotive gas turbines engines;</li><li>- Coal - gasification system;</li><li>- Insulating wrappings for investment casting;</li><li>- Components needing high temperature sulfidation resistance;</li></ul>
$\text{Ti}_3\text{Al}$	<ul style="list-style-type: none"><li>- Transition duct support;</li><li>- Seal housing;</li><li>- Compressor starters;</li><li>- Turbine frames;</li><li>- LP turbine airfoils.</li></ul>

**Table 2.3: Important Aluminides and Their Relevant Properties**

Alloy	Crystal Structure	Melting Point( $^{\circ}$ C)	Density (g/cc)	Yield Strength (MPa)	Young's Modulus (X10 <sup>3</sup> Mpa)
Ni <sub>3</sub> Al	L1 <sub>2</sub> (Ordered fcc)	1190	7.5	250-300	178.6
NiAl	B2 (Ordered bcc)	1640	5.9	250-475	294.4
Fe <sub>3</sub> Al	DO <sub>3</sub> (Ordered bcc)	1540	6.7	385-392	140.7
FeAl	B2 (Ordered bcc)	1250	5.6	360-380	260.6
Ti <sub>3</sub> Al	DO <sub>19</sub> (Ordered hcp)	1600	4.2	700-990	144.8
TiAl	L1 <sub>0</sub> (Ord. Tetragonal)	1460	3.9	400-650	175.8

and composition to overcome the brittleness problem in ordered intermetallics.

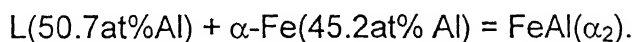
## 2.3 IRON ALUMINIDES

The most studied iron aluminides are FeAl and Fe<sub>3</sub>Al. The combination of low density, excellent oxidation and sulphidation resistance, and lack of strategic alloying elements make these alloys particularly attractive. However the major drawbacks of iron aluminides are their low ductility and fracture toughness at ambient temperatures and their poor strength at elevated temperatures i.e. above 600<sup>0</sup>C<sup>[14,15]</sup>. Recently, considerable efforts have been devoted in improving their mechanical properties through control of grain structure, alloy addition and material processing.

### 2.3.1 Iron – Aluminium Binary System

#### 2.3.1.1 Phase Diagram

Fe-Al binary phase diagram is shown in Figure 2.2<sup>[7]</sup>. Fe-Al system is characterised by a wide  $\alpha$ -Fe solid solution range. There are five stable intermetallic phases in the iron- aluminium system, namely Fe<sub>3</sub>Al, FeAl, FeAl<sub>2</sub>, Fe<sub>2</sub>Al<sub>5</sub>, and FeAl<sub>3</sub>, each of them with a homogeneity range. There are also two metastable phases Fe<sub>2</sub>Al<sub>9</sub> and FeAl<sub>6</sub>. Fe<sub>3</sub>Al is a low temperature phase. It is formed at 552<sup>0</sup>C and 26.5 at% Al by a first order reaction from FeAl ( $\alpha_2$ ). FeAl is formed at 1310<sup>0</sup>C by a peritectic reaction corresponding to:



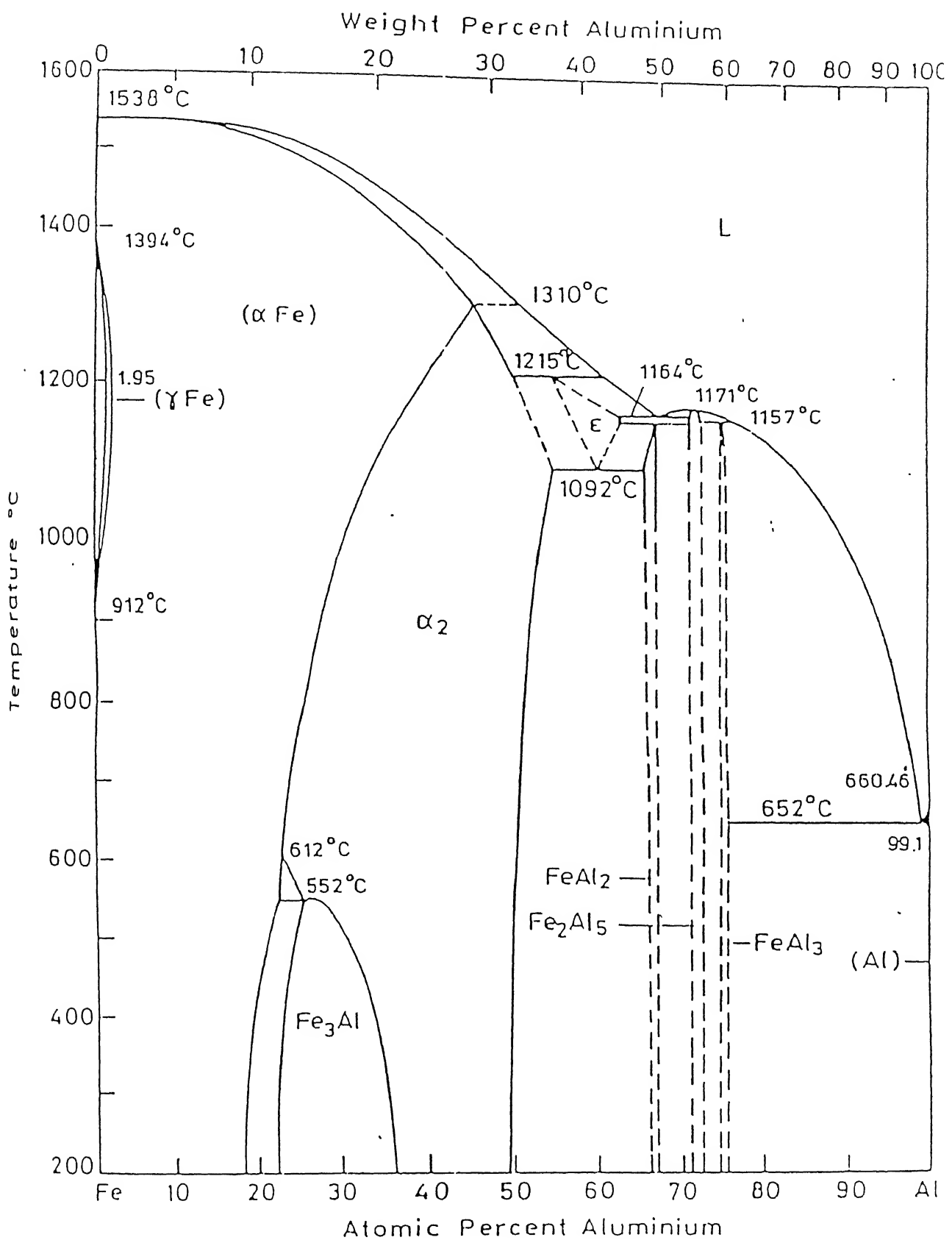


Figure 2.2: Fe-Al Binary Phase Diagram

In Figure 2.2 the formation of  $\alpha_2(\text{FeAl})$  is not shown as a peritectic reaction, but as a second order reaction concordant with the Fe-Si and Fe-Ga system.

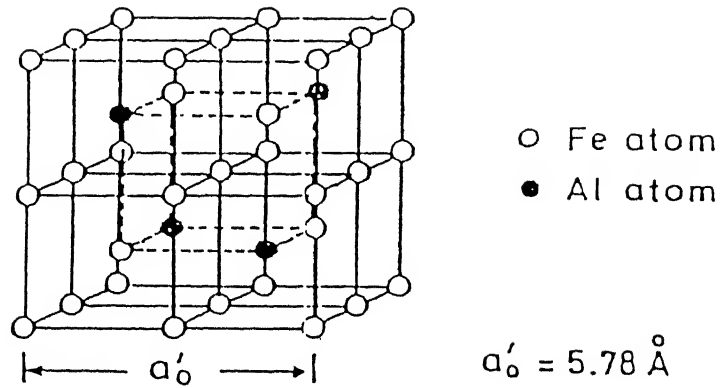
$\text{FeAl}_2$  is formed by a peritectoidal reaction at about  $1153^\circ\text{C}$ . There is general agreement about the congruent formation of  $\text{Fe}_2\text{Al}_5$ . The melting point of stoichiometric  $\text{Fe}_2\text{Al}_5$  is  $1171^\circ\text{C}$ . The Al-richest phase  $\text{FeAl}_3$  is formed peritectically at  $1157^\circ\text{C}$ .

### **2.3.1.2 Crystal Structure:**

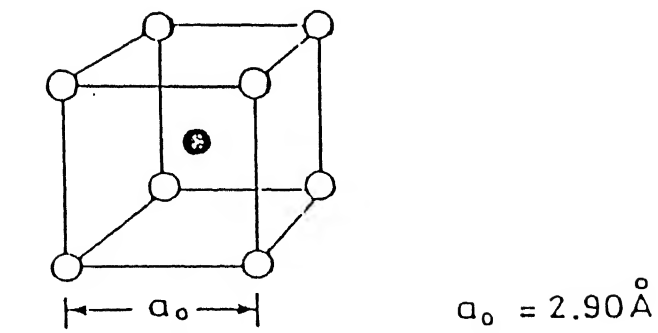
The stable phases studied very much are  $\text{Fe}_3\text{Al}$  and  $\text{FeAl}$ , which have  $\text{DO}_3$  and B2 ordered superlattice structure respectively. Both of these crystal structures are derivatives of BCC structures existing at room temperature over a range of 18 at% to nearly 36 at% Al respectively. The ordered  $\text{DO}_3$  structure consists of eight BCC cells with each unit cell consisting of sixteen atoms. B2 structure on the other hand, has two interpenetrating simple cubic lattices with the atoms of each constituent at the body center of each other (Figure 2.3).

The  $\epsilon$  phase was suggested to be bcc with 16 atoms per unit cell and the  $\zeta$  phase ( $\text{FeAl}_2$ ) to be rhombohedral with 18 atoms per unit cell. The structure of the latter phase was claimed to be more complicated<sup>[26]</sup>.

The  $\eta$  phase ( $\text{Fe}_2\text{Al}_5$ ), first believed to be monoclinic with 56 atoms per unit cell, was reported to be orthorhombic, with 'a=7.67 Å, b=6.40 Å, c=4.20 Å' for 72.0 at% Al.



(a)  $DO_3$  unit cell



(b)  $B2$  unit cell

Figure 2.3: Crystal Structures of FeAl and  $Fe_3Al$  lattices

The  $\theta$  phase ( $\text{FeAl}_3$ ) was previously believed to be orthorhombic. A complete structure analysis, using specimen with about 76.5% Al, revealed the structure to be monoclinic with 100 atoms per unit cell and  $a=15.489 \text{ \AA}$ ,  $b=8.083 \text{ \AA}$ ,  $c=12.476 \text{ \AA}$ ,  $\beta=107^\circ 43' \pm 1'$ <sup>[26]</sup>.

The existence of unstable  $\text{Fe}_2\text{Al}$ , claimed to be present in a complex Fe-Ni-Cr alloy, was reported by Beattie et al<sup>[25]</sup>. It was stated to be isotopic with  $\text{MgZn}_2$ .

A phase characterized as  $\text{FeAl}_6$  is C-centered orthorhombic isotopic with  $\text{MnAl}_6$  with  $a=6.492 \text{ \AA}$ ,  $b=7.437 \text{ \AA}$ ,  $c=8.788 \text{ \AA}$ . Investigations state that this phase is metastable at  $\geq 538^\circ\text{C}$ ; there is no evidence of it being an equilibrium phase<sup>[27]</sup>. Other information regarding crystal structures of iron aluminides are presented in table 2.4<sup>[6]</sup> and 2.5<sup>[7]</sup>.

### 2.3.2 Defects in Ordered Fe-Al Intermetallics:

As for  $\text{NiAl}$  and  $\text{CoAl}$ , anti-structural vacancies appear to form on Fe sites in  $\text{FeAl}$  at Al contents  $>50\%$ <sup>[8]</sup>. Vacancies may be formed in the iron aluminides by quenching from high temperature. Field ion microscopy showed that Fe-49.5% Al quenched from 1273 K contained a high ( $1.85 \pm .05 \text{ at\%}$ ) concentration of quenched-in vacancies, with their concentration being approximately twice as high on Fe sites as on Al sites.

In B2  $\text{FeAl}$  (Figure 2.4), dislocation configuration consists of two like  $a/2<111>$  dislocations connected by the corresponding  $a/2<111>$  antiphase boundary (APB), 'a' being lattice parameter of the B2 unit cell.

Table 2.4: Crystal Structure Data of Fe-Al intermetallics

Phase	% wt Al	Pearson Symbol	Space Group
$\alpha$ -Fe	0 - ~28	CL2	$\text{Im}\bar{3}m$
$\gamma$ -Fe	0 - ~0.6	cF4	$\text{Fm}\bar{3}m$
FeAl	12.8 - ~37	cP8	$\text{Pm}\bar{3}m$
$\text{Fe}_3\text{Al}$	~13 - ~20	cF16	$\text{Fm}\bar{3}m$
$\epsilon$	40 - ~47	cL16	--
FeAl <sub>2</sub>	48 - ~49.4	aP18	P1
Fe <sub>2</sub> Al <sub>5</sub>	53 – 57	oC	Cmcm
FeAl <sub>3</sub>	58.3 – 61.3	mC102	C2/m
Metastable			
Fe <sub>2</sub> Al <sub>9</sub>	68.5	mP22	P2 <sub>1</sub> /c
FeAl <sub>6</sub>	74.3	oC28	Cmc2 <sub>1</sub>

Table 2.5 Lattice parameters of iron aluminides

Phase	a-b-c (nm)	$\alpha$ - $\beta$ - $\gamma$ (°)	Structure type
FeAl	0.2909	90	BCC
		90	
		90	
Fe <sub>3</sub> Al	0.57923	90	BCC
		90	
		90	
FeAl <sub>2</sub>	0.4878	91.75	Complex
	0.6461	73.29	
	0.8800	96.89	
FeAl <sub>3</sub>	1.5489	90	Monoclinic
	0.8083	90	
	1.2476	107.72	
Fe <sub>2</sub> Al <sub>5</sub>	0.7675	90	Orthorhombic
	0.6403	90	
	0.4203	90	

The  $\text{DO}_3$  dislocation configuration consists of four like  $a'/2<111>$  dislocations connected by two types of APBs: (1) the outer pairs of dislocation are connected by an  $a/2<111>$  ( $a'/4<111>$ ) APB which is affected mainly by first nearest neighbour interaction energies and is similar to a B2 APB, and (2) the inner pair of dislocation are connected by an  $a'/2<100>$  APB which is affected by second nearest neighbour interaction energies. Here 'a' is the lattice parameter of  $\text{DO}_3$  unit cell.

These configurations are shown schematically in Figure 2.5. Such a configuration is required to preserve both first and second nearest neighbour order in the  $\text{DO}_3$  structure during deformation. Formation of the  $\text{DO}_3$  structure may be suppressed by quenching alloys from temperatures above  $\text{DO}_3$  ordering temperature ( $T_c$ ). In such cases, the alloys have an imperfect B2 structure and may exhibit  $\text{DO}_3$  and/or B2 order, the APB energy associated with the superlattice dislocations is very low resulting in large extension of the individual dislocation and allowing imperfect configurations (Figure 2.5(c)& 2.5(d)) to exist. Dislocations travel in  $\text{Fe}_3\text{Al}$  as unit dislocations, leaving ribbons of APB behind on their slip planes. In addition, a preponderance of screw dislocations are observed which in turn give rise to wavy slip. The observed preponderance of screw dislocations was attributed<sup>[9]</sup> to the elastic anisotropy of these materials. It was also found that at compositions of  $\text{DO}_3$  ordered alloys containing more than 30 at% Al only two  $a/2<111>$  dislocations moved together. These imperfect dislocations generate a  $'/2<100>$  APBs across the slip plane. The transition from

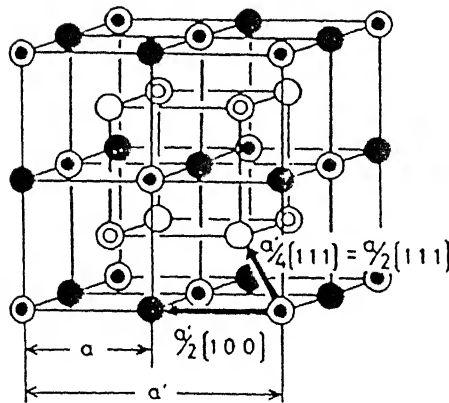


Figure 2.4 Unit cell and antiphase vectors associated with superstructures of Fe-Al system.

(a)  $\perp \dots \perp$

(b)  $\perp \dots \perp \text{-----} \perp \dots \perp$

(c)  $\text{-----} \perp \dots \perp$

(d)  $\dots \perp$

$\dots \text{NNAPB (Nearest Neighbour APB)}$

$\text{----- NNNAPB (Next Nearest Neighbour APB)}$

(a) B2 dislocation configuration

(b)  $\text{DO}_3$  dislocation configuration

(c) Passage of imperfect dislocation in  $\text{DO}_3$  lattice

(d) Passage of unit dislocation in B2 and  $\text{DO}_3$  lattice

Figure 2.5 Dislocation configuration in Ordered Fe-Al Alloys

perfect (four-fold: Figure 2.5(b) ) to imperfect (two fold :Figure 2.5(c)) configuration was explained by Crawford et al<sup>[9]</sup> . They reported B2 and  $DO_3$  APB energies estimated from observation of dislocation separation in superlattice configurations of Figure 2.5(a) and 2.5(b) for Fe-Al alloys containing 26 to 30 at % Al. Their results show that the  $a/2<111>$  ( $a'/4<111>$ ) APB energy increases whereas the  $a'/2<100>$   $DO_3$  APB energy decreases with increasing Al content. Therefore, with increasing Al content, the inner separation of the four-fold dislocations (Figure 2.5(b)) increases because of decreasing  $a'/2<100>$   $DO_3$  APB energy. Therefore, there is an increasing tendency for the outer pair of dislocations to uncouple when the separation is in the range of 0.05 to 0.1  $\mu\text{m}$ .

### **2.3.3 Properties of Ordered Fe-Al alloys**

#### **2.3.3.1 Crystallography of Slip & Twinning**

Slip systems in B2 Fe-Al alloys at 298 K have been reported to be  $\{110\} <111>$ <sup>[9]</sup>. Slip in FeAl single crystal is a strong function of orientation and deformation temperature. At about 0.44  $T_m$  there is a gradual transition from  $<111>$  to  $<001>$  slip with increasing temperature. The dislocation arrangement in crystals deformed by  $<001>$  type slip consists mostly of edge dislocations. There is also a composition dependence of the slip mode. The slip system in  $DO_3$  alloys is  $\{110\}<111>$ . Cohn and Coll<sup>[9]</sup> have shown that in a  $DO_3$  Fe-23.5% Al alloy, mechanical twinning occurred when the degree of long range order

was 0.5 or less. Twinning is more easily accomplished in the B2 than in the  $\text{DO}_3$  modification of  $\text{Fe}_3\text{Al}$ .

### 2.3.3.2 Strength

The hardness ( $H$ )<sup>[9]</sup> of B2 Fe-Al alloys varies with temperature according to the relation  $H = Ae^{-BT}$ , where A and B have one set of values at low temperatures and another set at high temperatures. At low temperatures, the hardness increases with increasing Al content, while at temperatures greater than 873 K, this behaviour is reversed.

The effect of aluminium content on the yield strength and ductility in 24 at% to 30 at% Al was studied by Mckamay et al<sup>[10]</sup> (Figure 2.6) . There is a gradual drop in yield strength (from 800 to 300 MPa) accompanied by a steady increase in ductility (from 1 to 5 % tensile elongation) with increasing Al content in  $\text{DO}_3$  Fe-Al alloys. The drop in strength is attributed to a change in deformation mode, from the dislocation configuration in Figure 2.5(d) to that in Figure 2.5(c), because of the increase in nearest neighbour APB energy with increase in Al content. Also, the transition from high stress value at 26 at% Al to a lower value at 27 at% Al coincides with the boundary between the  $\alpha+\text{DO}_3$  and  $\text{DO}_3$  phase fields at 800°C in the Fe-Al phase diagram (Figure 2.2). Based on this, Inoye<sup>[10]</sup> has shown that the higher ambient strengths at 24-25 at % Al composition is due to age hardening effect of  $\alpha$ -precipitated in  $\text{DO}_3$  phase during the ordering treatment at 800°C in these compositions. The ductility increase from 1% at 24 at% Al to 5% at 30 at% Al is apparently associated with the drop in yield strength

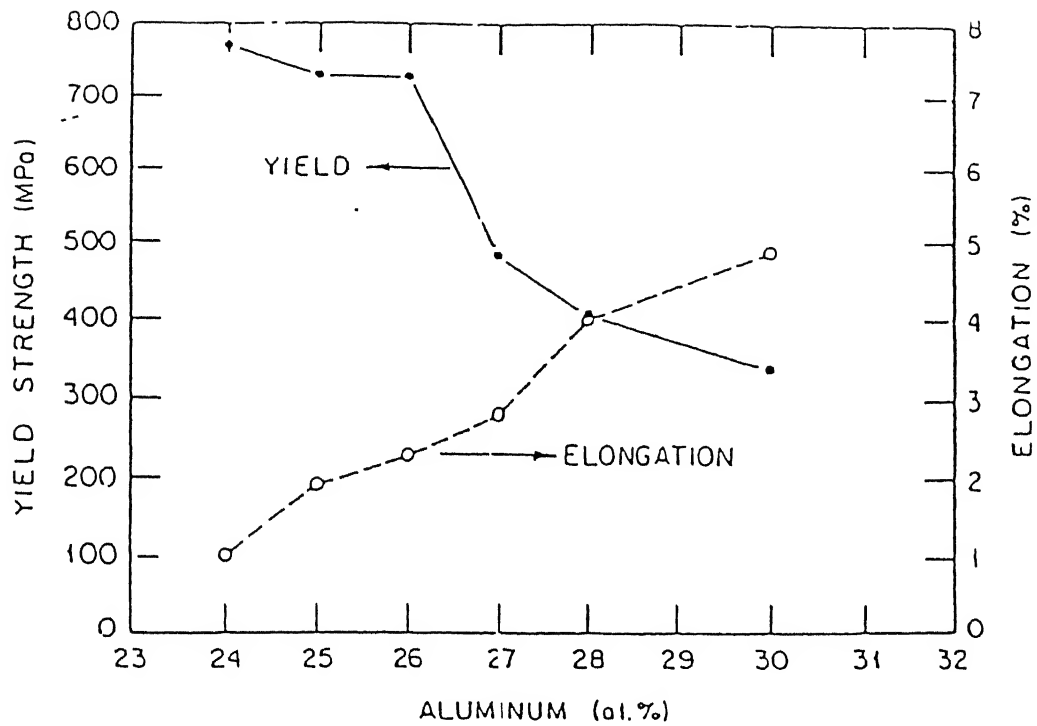


Figure 2.6 Plot showing variation of Yield strength and ductility with Al content

resulting from increasing Al content.

The effect of temperature on the yield strength for the  $\text{Fe}_3\text{Al}$  composition range is shown in Figure 2.7. Here the behaviour of various compositions can be grouped into two regions, one group up to 24 at% Al and another group from 28-30 at% Al composition range. As explained earlier, the highest ambient strength of 24 at% Al composition is attributed to the presence of  $\alpha$ -precipitates in  $\text{DO}_3$  matrix producing age-hardening effect. The second group (28-30 at% Al) exhibit maximum strength peak at approximately  $550^\circ\text{C}$ , which corresponds to the second-order transformation temperature from  $\text{DO}_3$  to B2. This type of yield behaviour has been observed in many other ordered systems including  $\text{Ni}_3\text{Al}$ ,  $\text{CuZn}$ ,  $\text{Ni}_3\text{Mn}$  and  $\text{FeCo}$ . Alloying studies to raise the transition temperature have been successful in improving the strength levels up to  $800^\circ\text{C}$ <sup>[12]</sup>. Figure 2.8 shows a typical compressive yield stress plot with temperature of  $\text{Fe}_3\text{Al}$  alloyed with different amounts of Mo & Ti with their respective transition temperatures. The strength peaks in  $\text{Fe}_3\text{Al}$  alloy may be explained by considering the dislocation structure in these alloys. The spacing between the dislocation pair comprising a superlattice dislocation (Figure 2.5(a)) is inversely proportional to long range order parameter ( $L$ ). At low value of  $L$ , this spacing is large and the energy of the connecting APB is small allowing constituent dislocations to glide independently. This process would leave APB trails creating wrong bonds and hardening the alloy. At high temperatures ( $T > T_c$ ) where  $L=0$ , the strengthening is mostly due to short-range order (SRO) and is less

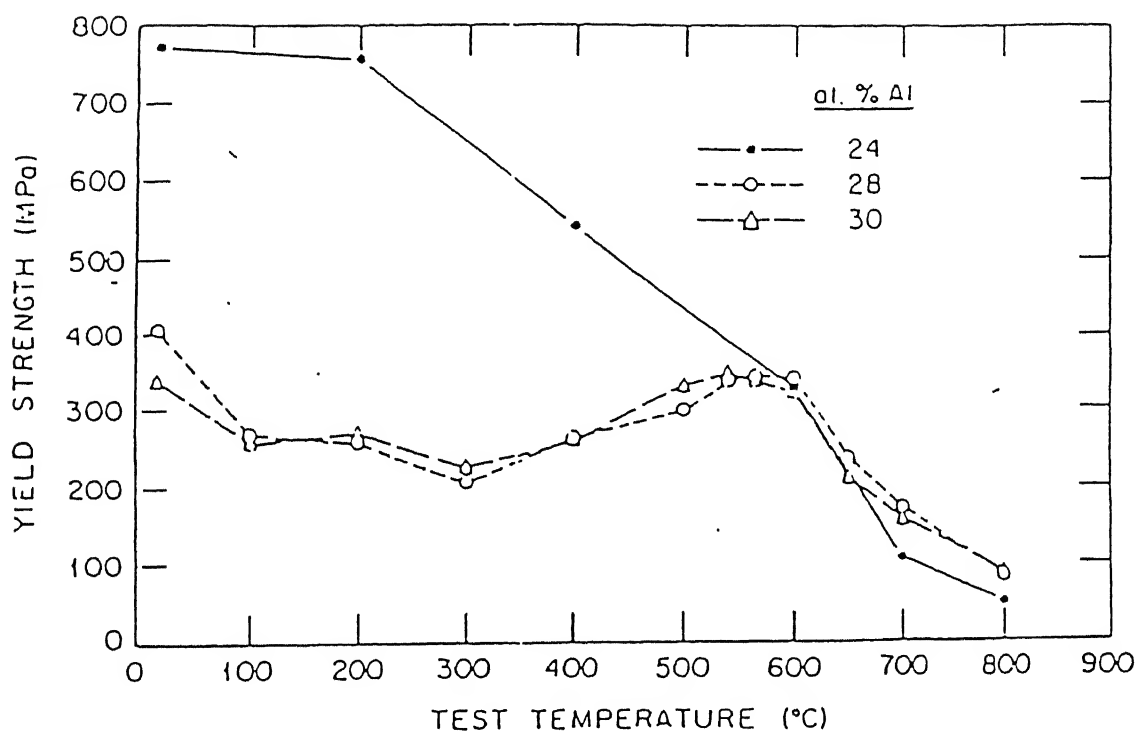


Figure 2.7: Yield strength vs temperature plot for unalloyed  $\text{Fe}_3\text{Al}$

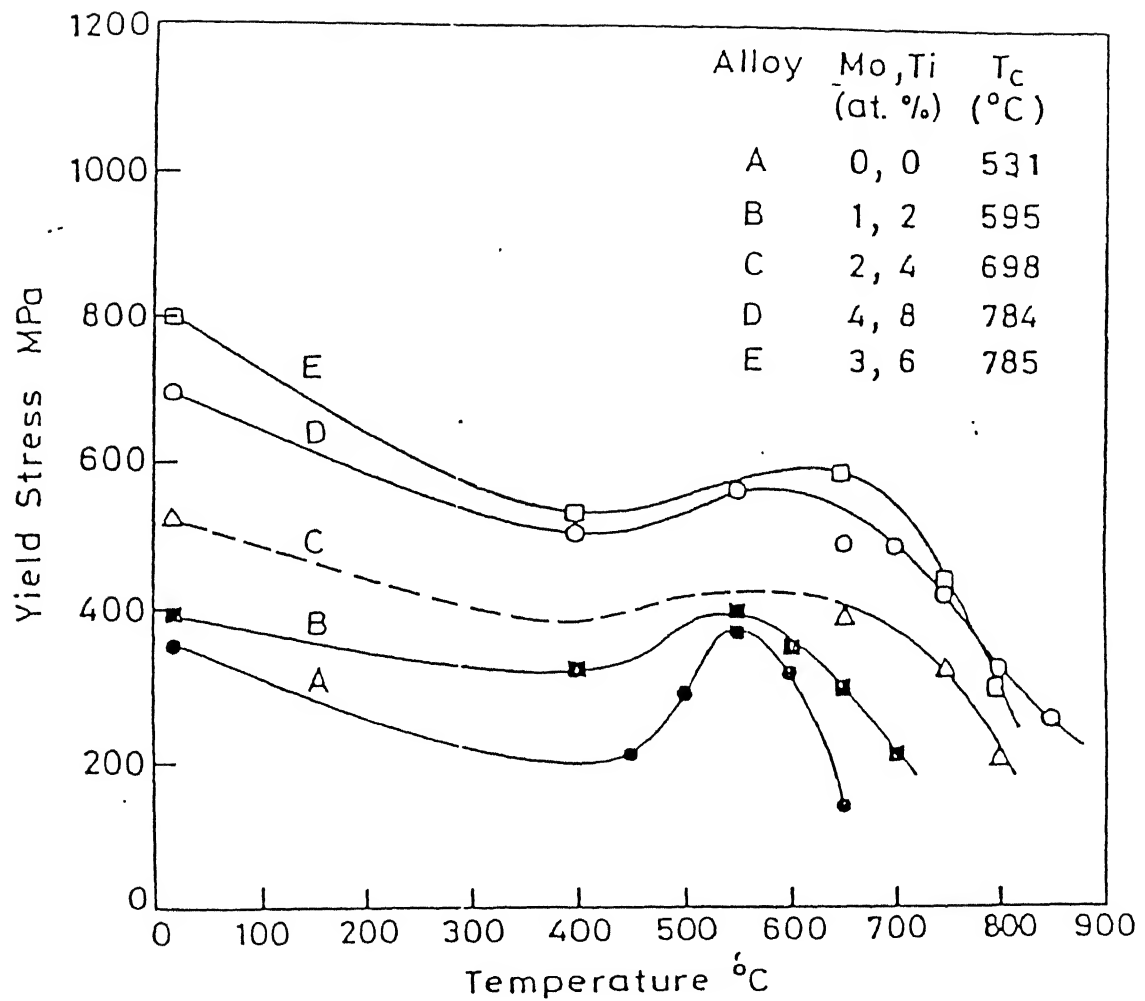


Figure 2.8: Yield Strength vs Temp plot for alloyed  $\text{Fe}_3\text{Al}$

marked compared to the strengthening in the presence of long range order (LRO) . At low temperatures, the value of L is large and the unit dislocations tend to associate in pairs. Their motion does not create extra APB's and hence the strength falls as the proportion of superlattice dislocations increases. The strength is a maximum at intermediate values of L where the superlattice dislocation configuration can dissociate into constituent dislocations and corresponds to a spacing of 0.05 to 0.1 mm. In  $\text{Fe}_3\text{Al}$  alloys, this critical degree of long range order parameter (L) related to the peak strength lies in the range 0.5 –0.6 irrespective of the  $\text{DO}_3$  to B2 transition temperature. Also, the value of L is shown to be 0.8 at room temperature.

#### **2.3.3.3 Work Hardening**

The work hardening behaviour actually observed to be dependent on the deformation temperature (which affects the nucleation of dislocation as the degree of  $\text{DO}_3$  order increases in  $\text{Fe}_3\text{Al}$  alloy, work hardening also increases), the degree of order of the material and its composition which determine the APB energies and hence the shear stresses required to produce them .

#### **2.3.3.4 Ductility**

As shown in Figure 2.6, there is an increase in ductility with increasing Al content in  $\text{DO}_3$  Fe-Al (24 at% to 30 at% Al) alloys. Room temperature ductility of polycrystalline Fe-Al alloys decreases rapidly with the onset of ordering. For Fe-Al alloys containing more than 30 at% Al, the ductility shows a general trend of decreasing with increasing Al

level<sup>[4]</sup> at temperatures up to 400°C. At higher temperatures, the alloys exhibit a peak ductility around 35-38 % Al. FeAl is brittle at higher Al contents because it fractures at grain boundaries before yielding. Lower Al content reduces the yield stress substantially and hence some ductility is observed before fracture.

A number of workers have reported on the elevated temperature ductility of ordered Fe-Al alloys. 100 % elongation were obtained in creep tests on  $DO_3$  Fe-27.8 % Al alloys at 826 K. Elongation of 12-16 % were reported for B2 Fe-Al alloys containing 39-40 % Al in compression tests conducted at 1300K<sup>[19]</sup>.

#### **2.3.3.5 Fracture**

As stated earlier, iron aluminides are inherently brittle at room temperature. The iron aluminides show low tensile elongation at room temperature and fracture mainly by cleavage for alloys with less than 40 at% Al and by brittle grain-boundary separation for alloys with more than 40 at% Al<sup>[4]</sup>. Proposed modes of fracture of Fe-Al alloys are summarized in Table 2.6<sup>[9]</sup>.

The major cause of low ductility and brittle fracture of iron aluminides is mainly by an extrinsic effect i.e. environmental embrittlement<sup>[4]</sup>. The yield strength is insensitive to environment, and the ultimate tensile strength correlates with the tensile elongation, which depends strongly on test environment. The iron-aluminides (Fe-36.5 at% Al) had ductility of 2% in air, 6% in vacuum and 17.6% in dry oxygen.

**Table 2.6 : Modes of Fracture in Ordered Fe-Al Alloys**

---

1. Cleavage on {100} Planes by <100> edge dislocations.
2. Cleavage failure due to hydrogen embrittlement.
3. (a) Cleavage failure due to dislocation APB interactions.  
(b) Intergranular failure in absence of these interaction.
4. Intergranular failure due to dendritic structure.
5. Failure at grain boundaries before yielding in bulk.
6. Intergranular failure due to weak grain boundaries.

---

The lowest ductility was observed in samples tested in water vapour and the samples tested in molecular hydrogen did not cause severe embrittlement of iron-aluminide, so this test indicates that moisture in air is the embrittling agent.

Environmental embrittlement has been explained by the following reaction :



The reaction of moisture in air with aluminium atoms at crack tips results in the generation of high fugacity atomic hydrogen that rapidly penetrates into the crack tips and causes severe embrittlement. The highest ductility is generally obtained in a dry oxygen environment, (rather than in vacuum) because oxygen reacts with the aluminium to form aluminium oxide directly, thereby suppressing the aluminium-moisture reaction and the generation of atomic hydrogen. It should be noted that the maximum degree of moisture induced hydrogen embrittlement occurs around ambient temperatures. At higher temperatures, less hydrogen is concentrated at crack tips, and in-situ protective oxide films can form more readily on specimen surfaces; whereas at lower temperatures, the aluminium-moisture reaction is slowed, and the equilibrium moisture content in air is lowered.

The environmental sensitivity of FeAl is markedly reduced when the aluminium concentration is higher than 38 at%. For Fe-43 at% Al, the ductility is almost nil in air as well as in dry oxygen; all specimens fail intergranularly. The lack of an environmental effect is explained by the

fact that the grain boundaries in FeAl alloys with Al>38 at% are intrinsically brittle. Therefore, environmental embrittlement and intrinsic grain-boundary brittleness must both be recognized in order to establish strategies for reducing overall brittleness in FeAl alloys. This, intrinsic grain boundary brittleness in FeAl as well as other intermetallics, can be alleviated by microalloying with boron, which tends to segregate to the boundaries and enhance their cohesive strength.

Similar air embrittlement has been observed in  $\text{Fe}_3\text{Al}$  alloys. The moisture-induced hydrogen affects not only tensile properties, but also the fatigue and crack growth behaviour. Under cyclic loading conditions, vacuum or oxygen environments raise the fatigue threshold and reduce crack growth rates at ambient temperatures. The degree of embrittlement under cyclic loading conditions is also affected by the crystal structure of  $\text{Fe}_3\text{Al}$ . The  $\text{DO}_3$  structure in a  $\text{Fe}_3\text{Al}$  alloy shows a crack growth rate much faster than that in the B2 structure, indicating that the  $\text{DO}_3$  structure is more susceptible to environmental embrittlement in air.

#### 2.3.3.6 Creep and Fatigue

The creep resistance of ordered intermetallics may be expected to be better than that of disordered alloys because of slower diffusion in the ordered lattice as well as because of more difficult glide processes<sup>[16,17]</sup>.

The creep resistance of the binary  $\text{Fe}_3\text{Al}$  alloy is relatively mediocre, but additions of small quantities of Mo and particularly Nb lead

to considerable improvements in creep rate and life<sup>[18]</sup>. These improvements have been attributed to improved solution hardening (for Mo) which reduces the rate of dislocation recovery, as well as to (for Nb) particle dispersion strengthening.

The stress exponent required for creep was found to be approximately 6 which remained constant over the ranges of Al-content (24 to 28 at%), temperature (843 to 943 K) and stress (15 to 278 MPa) studied. In contrast, the activation energy for creep was sensitive to Al-content. The creep rate was found to drop suddenly with the onset of  $DO_3$  ordering. The creep rate was also found to be dependent on grain size, more for a coarse grain size than for a finer grain size for  $Fe_3Al$  alloys<sup>[9]</sup>.

For B2 Fe-Al alloys of Al content 41 to 49 at%, Whittenberger<sup>[19]</sup> investigated creep phenomena in the temperature range 1100 to 1400 K and established that :

- (a) The activation energy for creep in these alloys was independent of composition.
- (b) Deformation may occur by two different and apparently concentration independent mechanism. One with a stress exponent of about 6 and the other with an exponent of about 3.
- (c) Both the deformation mechanisms are dependent on grain size but in opposite manner. For the low stress exponent mechanism the strength increased with increasing grain size and vice-versa.

(d) Under the high stress exponent mechanism a large-angle grain boundary structure may be replaced by a small-angle structure of similar grain diameter.

The study of high cycle fatigue behaviour of  $DO_3$  and B2 polycrystalline  $Fe_3Al$  ( $Fe$ -23.7 at% Al and  $Fe$ -28.7 at% Al), reveals that  $DO_3$  order is effective in prolonging fatigue life only in  $Fe$ -28.7 at% Al at 298K. This can be explained by the presence of superlattice dislocations, which are not observed in  $Fe$ -23.7 at% Al. This has been attributed to restrictions on cross slip imposed on superlattice dislocations, which delay crack initiation. The fatigue properties of B2 alloys found to degrade sharply with increase in temperature. Among  $DO_3$  alloys,  $Fe$ -23.7 at% Al shows little loss in fatigue life with increase in temperature which is attributable to its two phase microstructure while  $Fe$ -28.7 at% Al shows a sharp drop with increase in temperature over a range of 293 to 773 K<sup>[16]</sup>. At temperatures above the two-phase field, the fatigue life falls sharply as a result of creep-fatigue interaction. Here, crack initiation occurs at grain boundary near specimen surfaces, but propagation is predominantly by transgranular cleavage.

#### 2.3.3.7 Weldability & Corrosion Resistance

$Fe_3Al$  alloys are weldable with careful control of welding parameters and minor alloy additions<sup>[3]</sup>. Additions of  $TiB_2$  promote hot cracking and are detrimental to the weldability of  $Fe_3Al$  alloys. Addition of boron alone is also considered to be harmful that produces hot cracking and reduces the weldability. Carbon, on the other hand, appears to be

beneficial. Sound weldments have been achieved in  $\text{Fe}_3\text{Al}$  and  $\text{FeAl}$  alloys using both gas-tungsten arc welding and electron-beam welding processes. Weld cracking produced by environmental embrittlement is alleviated by pre- and post-weld heat treatments.

The iron aluminides are highly resistant to oxidation and sulfidation at elevated temperature. As stated earlier, resistance stems from the ability of the aluminides to form highly protective  $\text{Al}_2\text{O}_3$  scales. The oxidation resistance generally increases with increasing Al content, the major products are  $\alpha\text{-Al}_2\text{O}_3$  and trace amounts of iron oxides when the aluminides are oxidized at temperatures above  $900^\circ\text{C}$ . Cyclic oxidation of  $\text{Fe-40 at\% Al}$  alloyed with upto 1 at% Hf, Zr and B, produced little degradation at temperatures up to  $1000^\circ\text{C}$ . Aluminides specimen tested at 700 to  $870^\circ\text{C}$  showed no indication of attack in sulfidising environments, except for the formation of a thin layer of oxides with a thickness in an interface colour change. Further, iron aluminides exhibit corrosion rates lower than those of the best existing iron-based alloys by a couple of orders of magnitude when tested in a severe sulfidising environment at  $800^\circ\text{C}$ . In addition, the aluminides with more than 30 at% Al are very resistant to corrosion in molten nitrate salt environments at  $650^\circ\text{C}$ .

#### **2.3.4 Ternary Additions to Iron Aluminides**

Lack of ductility at ambient temperature and a decrease in strength at elevated temperatures have been major obstacles to acceptance of iron aluminides for various structural applications.

Considerable effort has been devoted to improve their mechanical properties by means of alloying process and thermomechanical treatments.

Cr additions<sup>[9]</sup> to Fe<sub>3</sub>Al have been reported to lower the yield strength but the ultimate tensile strength of Cr-modified alloy were higher due to work hardening. The room temperature elongation was raised from 4 % in Fe-28 at% Al to 8.2 to 9.4% in alloys with 2-6 % Cr. This was accompanied by a change in fracture mode from cleavage to a mixed intergranular cleavage failure suggesting that Cr enhances cleavage strength. Also, the Fe-Al-Cr alloys showed fine wavy slip lines as opposed to coarse, straight lines in the binary alloy indicating easier cross slip as a result of the Cr-addition. Such ductility enhancement has been related to the improvement in resistance to environmental embrittlement.

The high temperature strength of the Fe<sub>3</sub>Al intermetallic is determined largely by the stability of the DO<sub>3</sub> structure relative to the B2 structures. It is therefore, necessary to increase the DO<sub>3</sub>→B2 → $\alpha$  transition temperatures to strengthen Fe<sub>3</sub>Al at elevated temperatures. It has been shown that chromium, nickel and molybdenum additions increase these transition temperatures moderately, while silicon and titanium additions in Fe<sub>3</sub>Al increase the transition temperature as well as the elevated temperature strength significantly. However, titanium and silicon reduce the room temperature ductility so severely that they have not been considered for further developments. The combined effect of Ti

and Mo additions on  $\text{DO}_3$  to B2 transition temperature for  $\text{Fe}_3\text{Al}$  alloy is shown in Figure 2.8. The addition of Nb, Cu, Ta, Mn have also been found to raise the transition temperature<sup>[16,18]</sup>.

Boron, beryllium, zirconium, halfnium have also been found to obtain satisfactory high temperature creep properties and improved ambient temperature ductility in  $\text{Fe}_3\text{Al}$ . Many of these additions can introduce fine precipitates or dispersoids that reduce grain boundary sliding and inhibit the  $\text{DO}_3 \rightarrow \text{B2} \rightarrow \alpha$  transformation.

In addition to increase the hardness and tensile strength and to improve the ductility of the  $\text{Fe}_3\text{Al}$  intermetallic, nickel<sup>[21]</sup> addition is found to increase the size and number of pores in  $\text{Fe}_3\text{Al}$  intermetallic made from powder mixtures. Nickel refines the overall grain size and produces a mixture of the fine and coarse grain, in the presence of Ni, fracture of  $\text{Fe}_3\text{Al}$  is mixed transgranular and quasi cleavage.

Small amount of cerium<sup>[22]</sup> addition has been reported in improving ductility as well as strength at ambient temperature. The improvements of tensile properties and creep-resistance at high temperature can also be achieved by combined addition of cerium with molybdenum, zirconium or niobium. Cerium addition changes the fracture mode of  $\text{Fe}_3\text{Al}$  based alloy from transgranular cleavage or mixed transgranular cleavage and intergranular fracture to one of transgranular cleavage with portions of dimple fracture.

Small amount of niobium<sup>[18]</sup> addition to  $\text{Fe}_3\text{Al}$  based alloy has been found to increase the yield strength and creep resistance greatly,

but is not beneficial to room temperature ductility. Results of microanalysis indicate that the addition of niobium causes the formation of a lot of precipitates with complex compositions, which strengthen both matrix and grain boundaries.

The addition of carbon to  $\text{Fe}_3\text{Al}$  based alloys has been reported to decrease the ductility of these alloys<sup>[23]</sup>. When carbon content was reduced from 800 to 80 ppm and carbide precipitates were eliminated, the elongation values were found to increase significantly.

## 2.4 PROCESSING ROUTES FOR IRON ALUMINIDES

Various processing routes followed for production of intermetallic parts are shown in Figure 2.9 as a flow chart. These routes are discussed in detail in following subsections.

### 2.4.1 Ingots Metallurgy Route

Ingots metallurgy route<sup>[24]</sup> has been the focus of attention for the production of  $\text{Ti}_3\text{Al}$ ,  $\text{Ni}_3\text{Al}$ ,  $\text{Fe}_3\text{Al}$  based aluminides for a long period, despite the fact that this route has many problems. The primary fabrication process using the traditional methods of melting and casting poses serious problems, like the alloy inhomogeneity, the elemental losses, the casting defects, fracturing defects etc. The secondary fabrication to obtain necessary shapes and sizes by further deformation and machining, poses still further problem as the aluminides are generally brittle in nature.

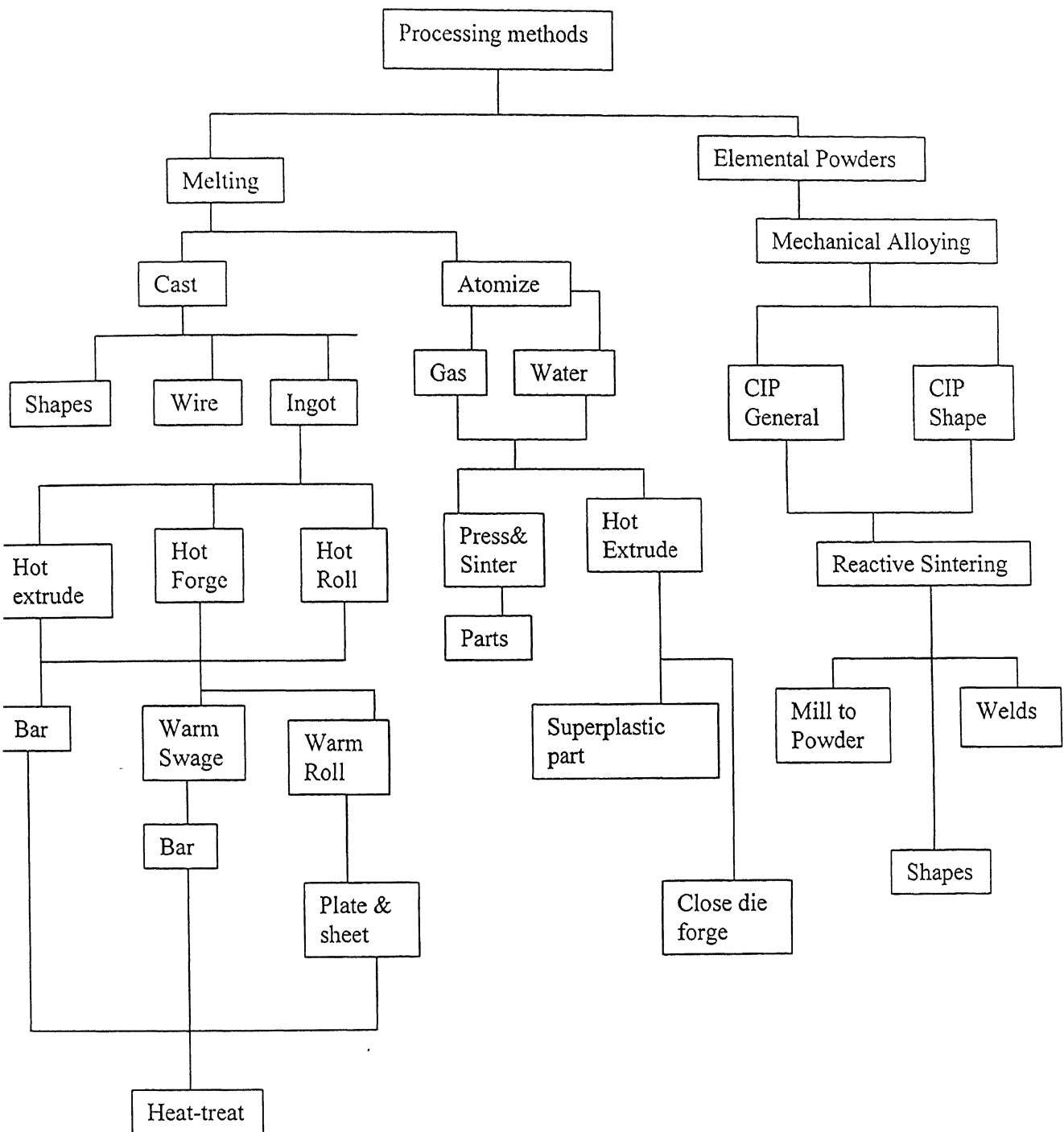


Figure 2.9 : Processing routes used to produce intermetallic parts.

#### **2.4.1.1 Melting**

Air melting is feasible for iron aluminide alloys. Reasonable, but not exceptional, care is needed in treating the melt charge and the selection of crucible material. Both the iron and aluminium need to be dried to minimize the generation of hydrogen. Because of the reaction of aluminium with moisture, a large amount of hydrogen can be generated and dissolved in liquid metal. It is the rejection of this hydrogen during solidification that causes the gas porosity in iron aluminides. Typical hydrogen levels in the  $\text{Fe}_3\text{Al}$  alloy melted in air can be in the range of 3 to 4 ppm. The hydrogen level of the alloy can be further reduced to approximately 2 ppm by blowing argon through the melt. Vacuum melting of the alloy can yield hydrogen level as low as 1 ppm. The protective aluminium oxide slag formation during melting yields low levels of oxygen and nitrogen in the melt and also provides nearly 100% recovery of most of the alloying elements. A combination of vacuum melting and electro-slag remelting processes further reduce oxygen and nitrogen contents of the  $\text{Fe}_3\text{Al}$  based alloys.

#### **2.4.1.2 Casting**

The  $\text{Fe}_3\text{Al}$  based alloys are castable in to shapes by both sand and investment casting processes. The casting parameters such as type of sand, melt superheat, cooling rates and post-cast treatments are not fully developed for sand castings. In case of investment castings, issues such as shell material, use of grain refiner, shell temperature, melt superheat, cooling rates, and post cast treatments need additional work.

The low room temperature ductility in the as cast condition is the primary concern in the handling and use of castings.

#### **2.4.1.3 Mechanical Working**

Fe<sub>3</sub>Al based alloys are hot workable with typical hot working temperature ranging between 900 – 1100°C. The hot worked material can be warm finished at temperature as low as 180°C. The Fe<sub>3</sub>Al based alloys are not cold workable.

#### **2.4.2 Powder Metallurgy Route**

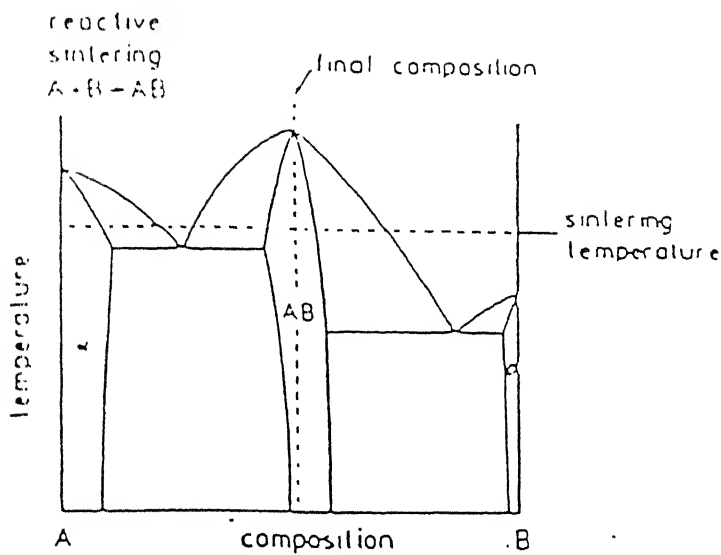
Powder metallurgy processing is becoming increasingly important for obtaining desirable microstructures, improved properties, and near net shape manufacturing capabilities for iron aluminides. Also, powder metallurgy processes bypass requirement of melting and casting large ingots and thus greatly reduce the problems associated with them. There are two types of powder metallurgical processes, one uses prealloyed aluminide powder and second uses elemental Fe and Al powders as starting materials.

##### **2.4.2.1 Powder Metallurgical Processes Based on Elemental Fe and Al Powders.**

Reactive sintering (also known as combustion synthesis, or self-propagating high temperature synthesis) is a novel process to produce ordered intermetallics from elemental powders through self-sustaining reaction. This approach utilizes an exothermic reaction between powder constituents to synthesize compounds<sup>[28]</sup>. Process advantages include the use of inexpensive and easily compacted elemental powders, low

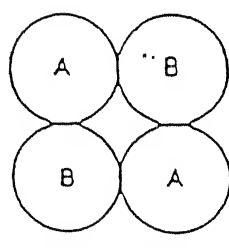
processing temperatures, short processing times and considerable flexibility in terms of compositional and microstructural control. Depending upon thermodynamic properties and phase diagram features, a variety of reaction products are possible, ranging from highly porous to full dense materials.

Reactive sintering is controlled by a transient liquid phase that forms during rapid exothermic heating. The initial compact is composed of mixed powders, which are heated to a temperature where they react to form a compound product. Figure 2.10 shows a schematic binary phase diagram where reaction sintering can be anticipated with various steps associated. Here, a stoichiometric mixture of A and B powders is used to form an intermediate compound product AB. The reaction occurs above the lowest eutectic temperature in the system yet at a temperature where the compound is solid. Heat is liberated because of the stability of the high melting temperature compound. Consequently, reactive sintering is nearly spontaneous once the liquid forms. The liquid provides a capillary force on the structure, which leads to densification. The liquid is transient as the process is conducted at a temperature below the melting point of the compound, typically near the eutectic. Reaction sintering involves a transient liquid phase, duration and amount of which depends on several processing parameters and which in turn controls the sintering characteristic. The reaction sintering is highly sensitive to parameters such as amount of additive and the particle size, green

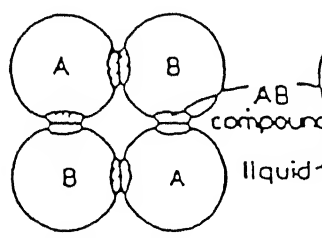


- start with a mixture of A and B powders
- finish with a sintered compact of AB compound

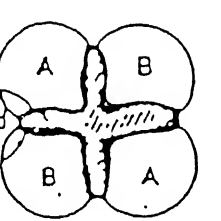
reactive sintering  $A + B \rightarrow AB$  : — increasing temperature —



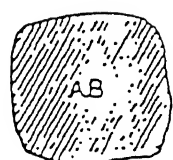
initial state  
 mixed powder



solid-state  
 diffusional  
 reaction



solid-liquid  
 rapid reaction



final state  
 densified  
 compound

Figure 2.10: Reactive sintering schematic diagram

Density of initial compact, heating rate, sintering atmosphere and sintering time.

The intent of prior studies on Fe-Al was not to form intermetallic compounds as products, nevertheless, the observations reported emphasize the problems encountered in this system. Elemental iron-aluminium mixture represent a particular challenge for powder processing because of extensive swelling during sintering. Swelling is predicted based upon phase diagram features (Figure 2.2), notably, there is a large solubility for aluminium in iron, low reverse solubility, and a large melting point difference, suggesting imbalanced diffusion rates. Systems that exhibit a large driving force for compound formation are particularly susceptible to the formation of porosity during alloying. Synthesis of iron aluminide from elemental powders has been reported in the literature. Reaction chemistry in Fe-Al, studied using differential scanning calorimetry (DSC) is shown in table 2.7.

The conventional reactive sintering involves no pressure i.e. it is pressureless sintering. The highest sintered densities obtained by Rabin and Wright<sup>[28]</sup> were approximately 75% of the theoretical for Fe-15wt%Al and 69% of theoretical for Fe-32wt%Al in pressureless reactive sintering. The higher sintered density can be obtained by applying an external pressure to the compact during sintering. This process is known as hot pressing. Here, pressure assisted densification is carried out by applying a load to the samples during the exothermic reaction. Rabin and

Table 2.7 Reaction Chemistry of Fe-Al

Atom%	Reaction Temp.(K)	Heating Rate (K/Min)	$-H_{298}^{\circ}$ KJ/g atom	Phase Present
50 Fe-50Al	911	15K/min	19.6	AlFe, $Fe_2Al_5$ , Fe
75 Fe-25Al	916-984	15K/min	7.69	$Fe_3Al$ , Fe

Wright also observed the effect of applied pressure on density for both the compositions, which is shown in Figure 2.10. Near full density was achieved for both compositions when an applied pressure of 70 MPa was used. Significantly higher densities were also obtained for a given applied pressure when the larger powder charge was used. This suggests that the larger thermal mass resulted in slower cooling from the reaction temperature, thus allowing more densification to take place.

#### **2.4.2.2 Powder Metallurgical Processes Based on Prealloyed Iron-Aluminide**

##### **Powder**

Though iron aluminides can be prepared by reactive sintering of elemental powders of iron and aluminum, this method does not have such control and flexibility as synthesis from prealloyed iron aluminide powders.

Mechanical alloying, rapid solidification and physical vapour deposition, far from equilibrium techniques for synthesis of prealloyed iron aluminide powders allow novel constitutional and microstructural effects and hence potentially enhanced physical and mechanical properties in powders and therefore in products made from them.

These techniques lead to various combinations of the following attributes in powder<sup>[30]</sup>:

- 1) Production of, a fine dispersion of second phase particles.
- 2) Extension of solubility limits.
- 3) Refinement of the matrix microstructure down to the nanometer range.

- 4) Synthesis of novel crystalline phases.
- 5) Development of amorphous (glassy) phases.
- 6) The possibility of alloying elements which are difficult to alloy.
- 7) Inducement of chemical reaction at low temperatures.
- 8) Scalable process.

These attributes can be maintained in the product made out of these pre alloyed powders by proper processing.

Prealloyed intermetallic powders are generally brittle and therefore it is difficult to process them via classical P/M route. Hot pressing, Hot isostatic pressing, Shock consolidation, Hot extrusion processes are main routes to process these brittle powders. Near full density had been achieved by these processes with the special attributes mentioned above<sup>[29]</sup>.

## CHAPTER 3

### EXPERIMENTAL PROCEDURE

#### 3.1 STARTING MATERIAL

Iron and iron-aluminide powders were used as starting material.

##### 3.1.1 Iron Powder

Electrolytic iron powder of purity > 99.0% supplied by Sudhakar Products, Mumbai, were used. Scanning electron micrographs of the powder are shown in Figure 3.1. Iron particles are shown to be of somewhat round shape. Size distribution of iron powders in histogram is shown in Figure 3.2. As shown, iron powder particle size lies in narrow range of 80 to 100  $\mu\text{m}$ . BET surface area measurement results as obtained from COULTER (machine to measure surface area), gives specific surface area of the iron powder as 0.538 sq.m/g.

##### 3.1.2 Iron Aluminide Powder

Scanning electron micrograph of the iron-aluminide powder is shown on Figure 3.3. As shown in the Figure, iron aluminide particles were found to have roughly planar surfaces and straight and sharp corners. Such powder shapes are typical of powders produced by mechanical milling of brittle materials.

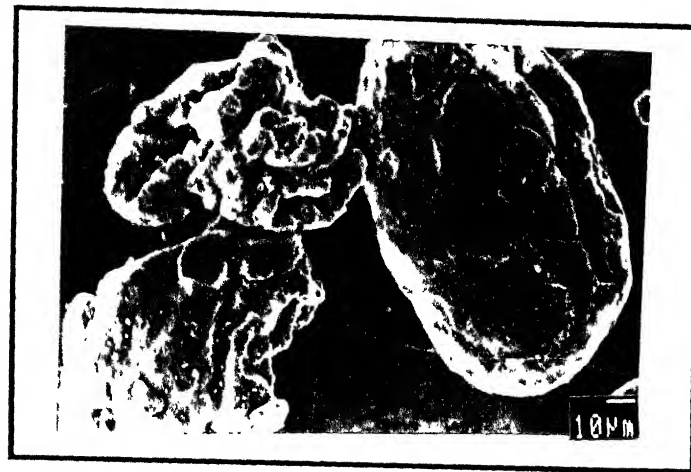


Figure 3.1 SEM micrographs of Iron powder

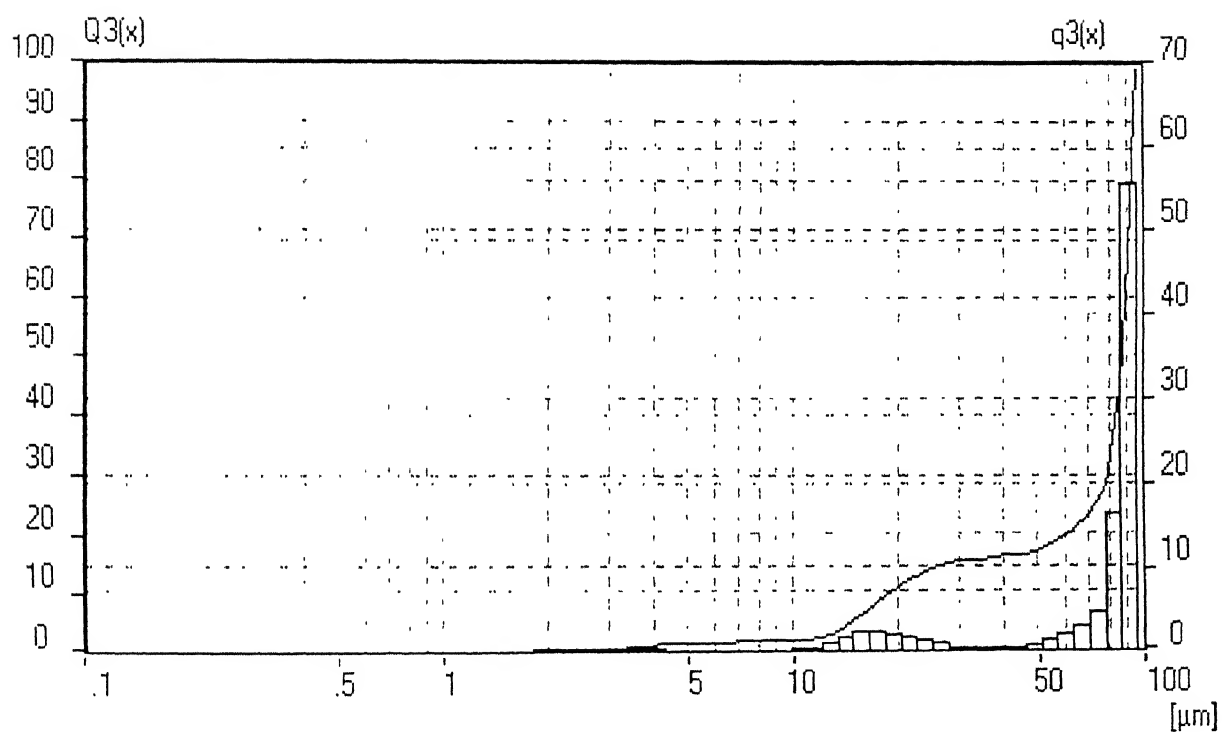


Figure 3.2: Histogram showing particle size distribution of iron powder



Figure 3.3 SEM micrograph of Iron Aluminide powder

The particle size distribution of iron-aluminide powder is shown in Figure 3.4. According to the histogram shown in Figure 3.4 iron-aluminide powders were distributed mainly in the  $<1\text{ }\mu\text{m}$ ,  $2\text{-}5\mu\text{m}$  and  $7\text{-}11\mu\text{m}$  size ranges .

BET specific surface area for aluminide powder used is 0.242 sq.m/g as obtained from COULTER' surface area results .

### **3.2 REDUCTION OF IRON POWDER**

The iron powder available was containing some oxide impurities. These impurities may affect densification during sintering by hindering the diffusion process. Therefore reduction of iron powder was thought necessary. The set up used for reduction is schematically shown in Figure 3.5. Hydrogen gas was used as the reducing agent. The iron powder was put in a quartz glass tube, closed at one end. Hydrogen inlet and outlet both were on the same side for better thermal and reduction efficiency. Reduction was done at  $500^{\circ}\text{C}$  for four hours. Hydrogen atmosphere was maintained during cooling of reduced powder to  $50^{\circ}\text{C}$ . This reduced iron powder was used in further experiments directly.

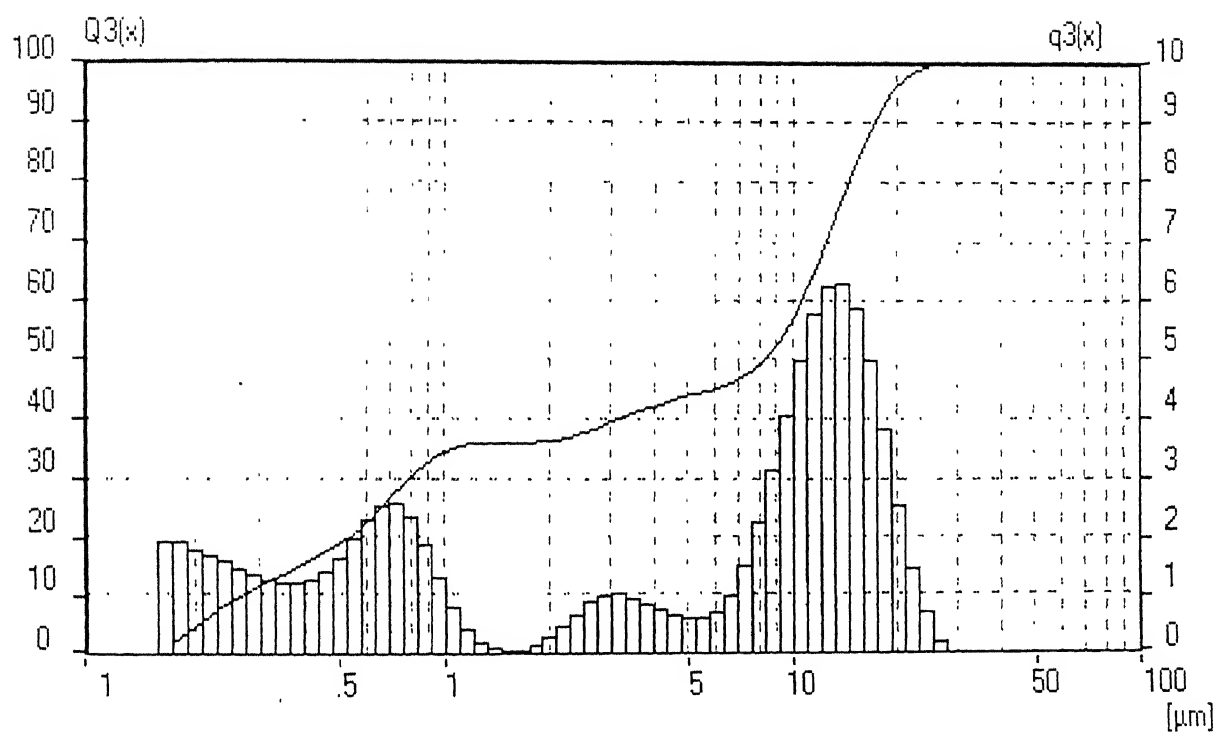


Figure 3.4: Histogram showing particle size distribution of the iron aluminide powder used.

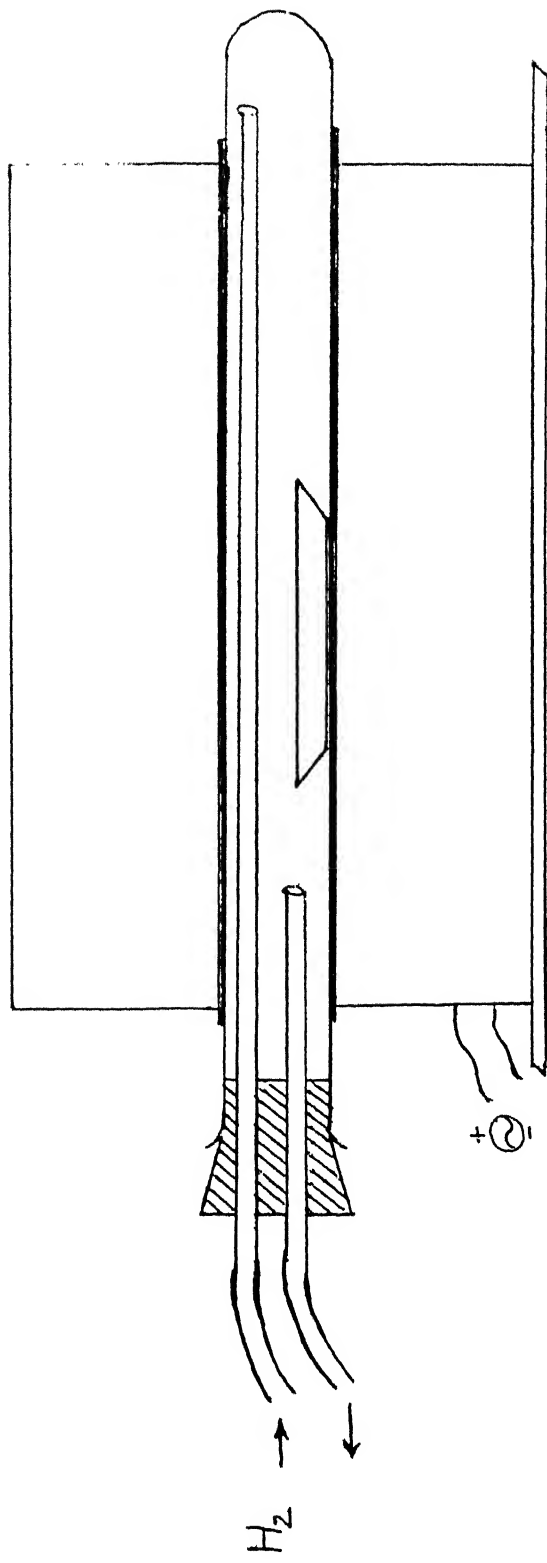


Figure 3.5: Schematic diagram of the apparatus used to reduce iron powder

### **3.3 COLD COMPACTION AND SINTERING OF IRON AND IRON –**

#### **ALUMINIDE POWDER MIXTURE**

##### **3.3.1 Cold Compaction**

Powder mixture with 3 different iron contents 0%, 5% and 12% were prepared by mixing them manually for 10 minutes each. Powder mixtures were pressed in steel die of diameter 18.62 mm in 50 T hydraulic press under 19.6 Mpa pressure. The weight of the powder taken for each compact was approximately 10 g. Zinc stearate was used as the lubricant.

##### **3.3.2 Sintering of Green Compacts**

The green compacts so obtained were sintered in a horizontal tube INCONEL furnace with SiC heating rods. The furnace was closed from one end and had the provision for maintaining a protective atmosphere.

Green compacts of three different compositions 0% Fe, 5% Fe and 12% Fe were sintered at three temperatures: 1100°C, 1150°C and 1200°C and duration of sintering were 1, 2 and 4 hours. The argon gas (IOLAR-1 grade) was used as sintering atmosphere throughout the experiment.

### **3.4 HOT ROLLING OF SINTERED COMPACTS**

Some of the sintered samples were hot rolled after soaking them for one hour at 1100°C to increase the density of the samples. For this

purpose 2 high rolling mill were used and furnace was brought near to the nip of the roller to decrease the drop of temperature during transfer of sintered compacts from the furnace to the rolling mill. This experiment was discarded because all samples fractured in brittle manner during rolling.

### **3.5 HOT PRESSING OF IRON –IRON ALUMINIDE POWDER MIXTURE**

Hot pressing experiments were done in the hot press of Dr. FRITSCH K. G.,West Germany. Powder mixture was filled in 10mm. Diameter graphite die. It was then loaded with graphite punch.

The hot pressing was done at three temperatures of 650°C, 700°C and 800°C. The requisite temperatures were obtained by resistance-heating of the graphite die. The temperature was continuously monitored by chromel-alumel thermocouple inserted into the graphite die wall. It took 1 hour for one hot pressing including 5-10 minutes holding time at the hot pressing temperature under 0.2 ton/s.inch .

A schematic sketch depicting hot pressing set-up is shown in Figure 3.6.

Samples containing 0%, 10%, 15%, 20%, 30%,40%and 50% Fe were prepared for hot pressing temperature of 800°C and with 20%,30%,40% and 50% Fe were prepared for hot pressing temperature of 650°C and 700°C.

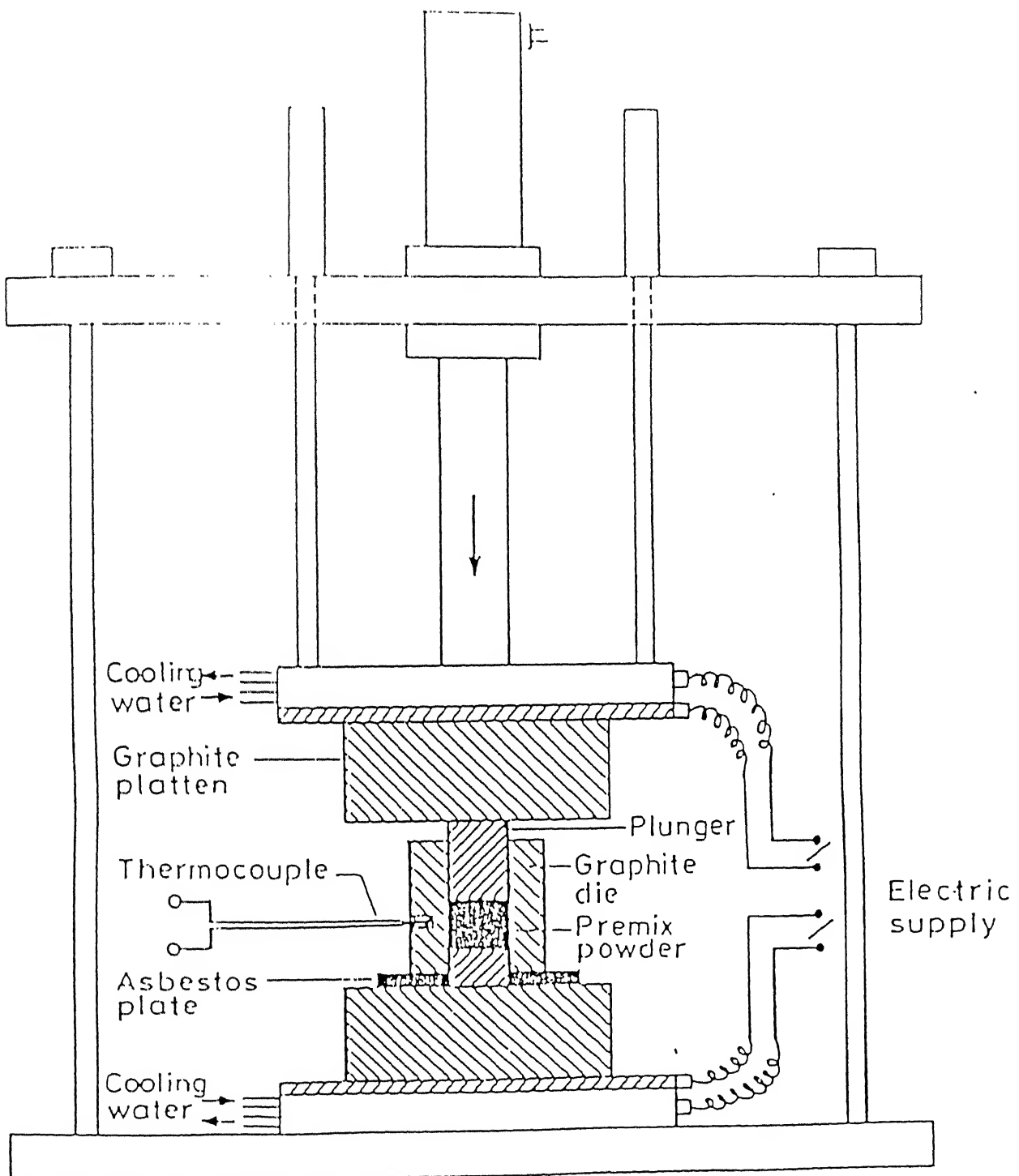


Figure 3.6: Schematic diagram of the hot pressing unit used.

### **3.6 CHARACTERIZATION OF POWDERS, SINTERED AND HOT PRESSED SAMPLES**

#### **3.6.1 X-ray Diffraction Analysis**

X-ray analysis of powders and hot pressed samples was done on ISO-DEBYEFLEX 2002 with Cu-K $\alpha$  radiation and on ISO-DEBYEFLEX 1001 with CrK $\alpha$  radiation. The 2 $\theta$  values were obtained directly through X-ray diffraction. These 2 $\theta$  values were compared with standard 2 $\theta$  values given in JCPDS Powder Diffraction Data files for identification of the phases.

#### **3.6.2 Scanning Electron Microscopy**

Powders and hot pressed samples were observed under JEOL JSM 840A scanning electron microscope (with EDAX facility) at an operating voltage of 15 kV.

The hot pressed samples for SEM were prepared by first polishing the samples, cut by diamond cutter, on SiC emery paper of grades 180, 320, 400, 600 followed by coarse and fine wheel polishing alumina powder suspension in water. Nital was used as etchant.

#### **3.6.3 Density Measurements**

Densities of samples were measured by dividing weight by the volume of samples. For cold pressed samples volume was calculated from the dimension of the cylindrical samples.

### **3.6.4 Hardness Testing**

Microhardness measurements were done on sintered and hot pressed samples using Leitz Miniload Microhardness Tester. At least 20 readings were taken to note the variation of hardness from one region to another. Rockwell hardness was also tried on C and A scale but samples broke under the load. Therefore Rockwell hardness measurement could not be done.

### **3.6.5 Compresssion Testing**

Compression tests were carried out using an INSTRON universal testing machine on a full scale load of 20 kN and with cross-head speed of 0.2mm/min. The compressive strengths were calculated from the load applied divided by the final area of the compacts .

### **3.6.6 Electron-Probe-Micro-Analysis**

To obtain point analysis of compacts, electron probe micro analysis technique has been used. In this micro-analysis, a small electron probe(0.1  $\mu\text{m}$  diameter) is used to generate x-rays from a defined area of a polished specimen and the intensity of various x-rays measured using Wavelength Dispersive Spectrum (WDS) spectrometer .

EPMA was used primarily to study the effect of hot pressing on the local variation of composition in the hot pressed samples.

### RESULTS AND DISCUSSION

#### 4.1 IDENTIFICATION OF PHASES IN THE STARTING IRON ALUMINIDE POWDER

The binary Fe-Al phase diagram, as shown in Figure 2.2, shows that several iron aluminides, namely  $\text{Fe}_3\text{Al}$ ,  $\text{FeAl}$ ,  $\text{FeAl}_2$ ,  $\text{Fe}_2\text{Al}_5$  and  $\text{FeAl}_3$  exist in the system. The wet chemical analysis results showed that the starting iron aluminide powder contained ~51 wt% Fe and ~49 wt% Al, implying that the starting material may contain a mixture of  $\text{Fe}_2\text{Al}_5$  and  $\text{FeAl}_2$  phases. X-ray diffraction results obtained from the starting iron aluminide powder are shown in Figure 4.1. In order to identify the phases present in the starting material, the standard diffraction data for all the five intermetallic phases was taken from the JCPDS files. Diffraction angles, i.e. 2 $\theta$ , for the first five high intensity peaks of all the intermetallic phases are presented in table 4.1. From the knowledge of these values, the peaks obtained from the diffraction pattern of the starting powder were identified with the probable Fe-Al intermetallic phases. Peaks in Figure 4.1, are labelled with respect to the phases from which they are likely to occur. Detailed analysis of all peaks thus suggested the presence of  $\text{Fe}_2\text{Al}_5$  and  $\text{FeAl}_2$  phases confirming the results obtained from the wet chemical analysis also.

Table 4.1: 20 Values for 5 High Intensity Peaks of Iron Aluminide

Phase	Intensity	2θ		h	k	l
		CuK $α$ $λ=1.54056\text{ Å}$	CrK $α$ $λ=2.20897\text{ Å}$			
FeAl	100	44.369	67.975	1	1	0
	20	81.503	151.194	2	1	1
	12	30.916	46.521	1	0	0
	8	64.177	104.287	2	0	0
	4	54.935	86.556	1	1	1
Fe <sub>3</sub> Al	100	44.186	67.975	2	2	0
	19	81.286	150.967	4	2	2
	12	64.256	104.450	4	0	0
	8	114.474	—	6	2	0
	7	26.627	40.029	1	1	1
FeAl <sub>2</sub>	100	18.988	28.381	1	1	1
	80	20.994	31.421	0	4	0
	80	24.836	37.279	2	1	1
	80	25.201	37.838	1	4	0
	80	26.790	40.280	0	3	1
Fe <sub>2</sub> Al <sub>5</sub>	100	42.823	65.719	0	0	2
	100	44.141	67.899	1	3	0
	40	27.857	41.926	0	2	0
	25	23.022	34.974	2	0	0
	16	62.726	101.347	2	4	0
FeAl <sub>3</sub>	100	44.832	69.049			
	83	43.472	66.790			
	20	64.177	104.287			
	17	21.819	32.674			
	11	24.164	36.281			
Fe <sub>4</sub> Al <sub>13</sub>	100	43.253	66.429	3	2	5
	100	44.369	68.275	2	3	4
	100	44.832	69.049	4	0	6
	60	24.164	36.251	3	0	3
	60	25.135	37.738	2	2	0

## 4.2 COLD COMPACTION BEHAVIOUR OF IRON ALUMINIDE AND IRON – IRON ALUMINIDE POWDER MIXTURES

### 4.2.1 Compaction Behaviour of Iron Aluminide Powder

Compacts prepared from only iron aluminide powder were found to be loosely bonded and had very poor strength. Thus, efforts to consolidate iron aluminide powder alone by cold die compaction were not successful. This poor compactability of the aluminide powder can be attributed to the brittle nature of iron aluminides, in general, and the angular shape of the powder, as shown in Figure 3.3.

### 4.2.2 Effect of Iron Addition

To increase the bonding among particles of iron aluminide powder, additions were made of 5% and 12% iron powder respectively. Such additions lead to green compacts of better handlability. However, most of the compacts made by iron additions were found to suffer from the lamination problem. Efforts were made to remove the lamination problem in the iron-iron aluminide powder mixture compacts by varying the amount of the lubricant, i.e. zinc stearate, but no improvement was achieved in the case of powder mixtures containing 5 wt% iron. The lamination problem in the case of powder mixture containing 12 wt% iron, on the other hand, could be substantially reduced.

As mentioned previously the goal of the present work was to prepare multi-phase iron aluminides and iron– iron aluminide composites by the P/M route. Therefore, five different powder mixtures containing

10%, 20%, 30%, 40% and 50% Fe by weight were cold pressed. The compaction pressure in all cases was kept at 200Kg/cm<sup>2</sup>. Compacts thus prepared were found to be coherent with good handling strength.

The variation of density of iron – iron aluminide powder compacts with iron content is shown in table 4.2. Relative density of green compacts prepared from different iron-iron aluminide powder mixtures was calculated as given below:

$$\text{Relative Density, } \rho_{\text{rel}} = (\rho / \rho_0) \times 100,$$

Where

$\rho$  = density of the green compact

$\rho_0$  = density of fully dense material with a particular composition

$$\rho_0 = 100 / (\text{wt\%Fe}/\rho_{\text{Fe}} + \text{wt\%Aluminide}/\rho_{\text{Aluminide}})$$

Variation of the relative density,  $\rho_{\text{rel}}$ , with the wt% of iron in iron – iron aluminide green compacts is shown in Figure 4.2. It is clear that the relative density of the green compacts increases with increase in iron content.

It is worth noting that the iron, being the softer phase in the powder mixture, works as a binder and thus improves the compaction behaviour of the iron-iron aluminide powder mixture. The consolidation of the powder mixture thus improves with increase in its iron content and leads to higher green density of compacts. On the other hand, the density of iron is higher than that of the iron aluminide. Thus increase in the density of iron-iron aluminide powder compacts, as a function of their iron content, can be considered to be due to two reasons namely (a) an

**Table 4.2: Density Measurement Results Of Cold Compaction Of Iron-Iron**

**Aluminide Powder Mixture (Pressure = 200 Kg/Cm<sup>2</sup>)**

Sl. No.	%Fe	$\rho$ (g/cc)	$\rho_0$	%Density
1	10	3.229	4.5375	71.16
2	20	3.660	4.7627	76.85
3	30	3.905	5.0115	77.92
4	40	4.281	5.2877	80.96
5	50	4.575	5.5961	81.75

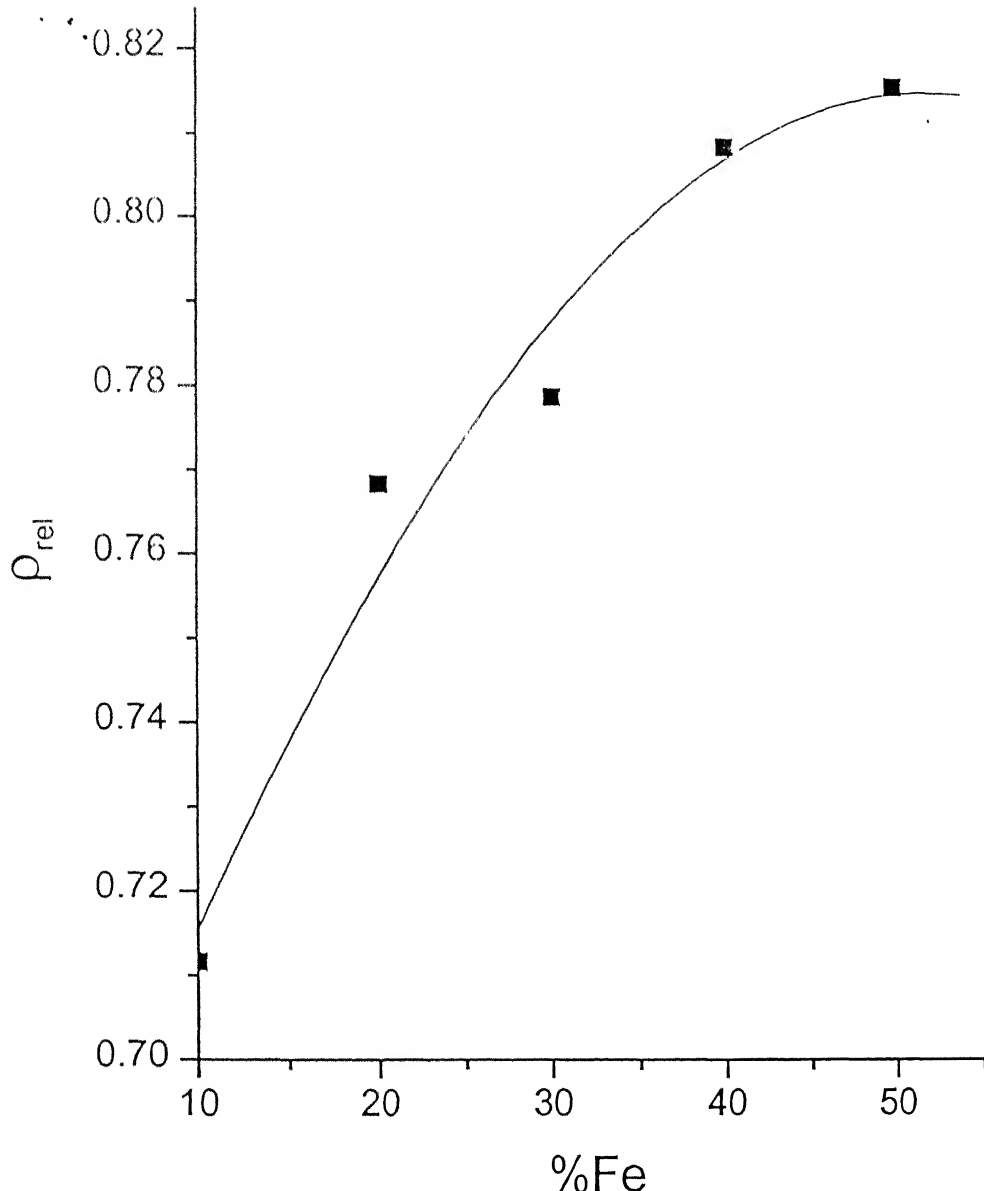


Figure 4.2: Plot showing variation of relative density of iron–iron aluminide green compacts (compressed under a constant load of 200Kg/cm<sup>2</sup>) with iron content

improved consolidation behaviour of powder mixture as explained above and (b) higher density of iron. Variations of the green density of iron-iron aluminide powder compacts,  $\rho$ , and the theoretical density of fully dense compacts,  $\rho_0$ , with the iron addition are shown in Figure 4.3 and Figure 4.4 respectively. The effect of iron in increasing the theoretical density,  $\rho_0$ , is obvious from the Figure 4.4. Similarly, it can be seen that the green density of iron-iron aluminide powder compacts keeps increasing with wt% of iron.

It is worth recalling that while iron powder consisted of coarse particles with the mean particle size of about 100  $\mu\text{m}$ , iron aluminide powder particles were finer with the mean size of about 10  $\mu\text{m}$  (Chapter 3, Section 3.1). It is well understood that a bimodal distribution of particles gives rise to a continuous variation of packing density with volume fractions of the powders, which passes through a maximum in the packing density of the powder mixture. In the present experiments this peak is yet not achieved as shown in the Figure 4.2, where the slope of the relative density vs %Fe curve is found to decrease with increase in %Fe but not being negative. This suggests that iron content in the powder mixture can be increased beyond 50% without loss of packing density. But the relative effect of the iron addition decreases with increasing iron as clear by the decrease in slope in figure 4.2.

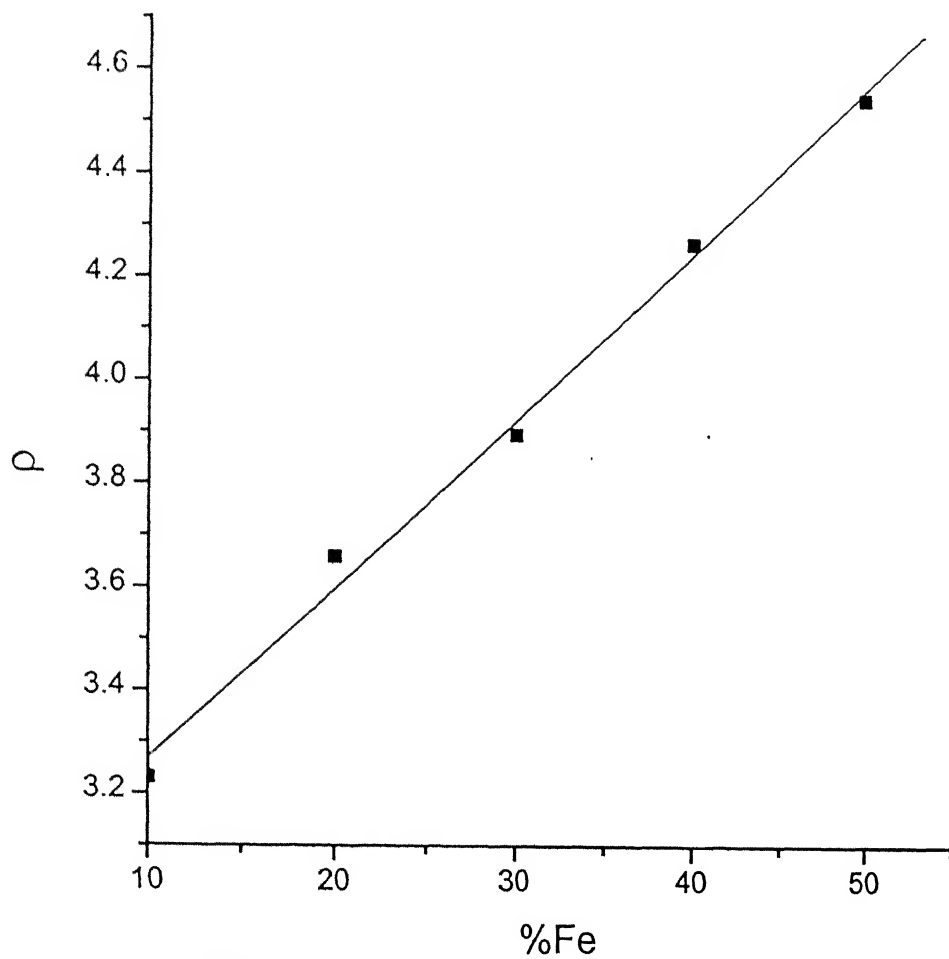


Figure 4.3: Plot showing variation of green density of iron-iron aluminide compacts with change in iron content

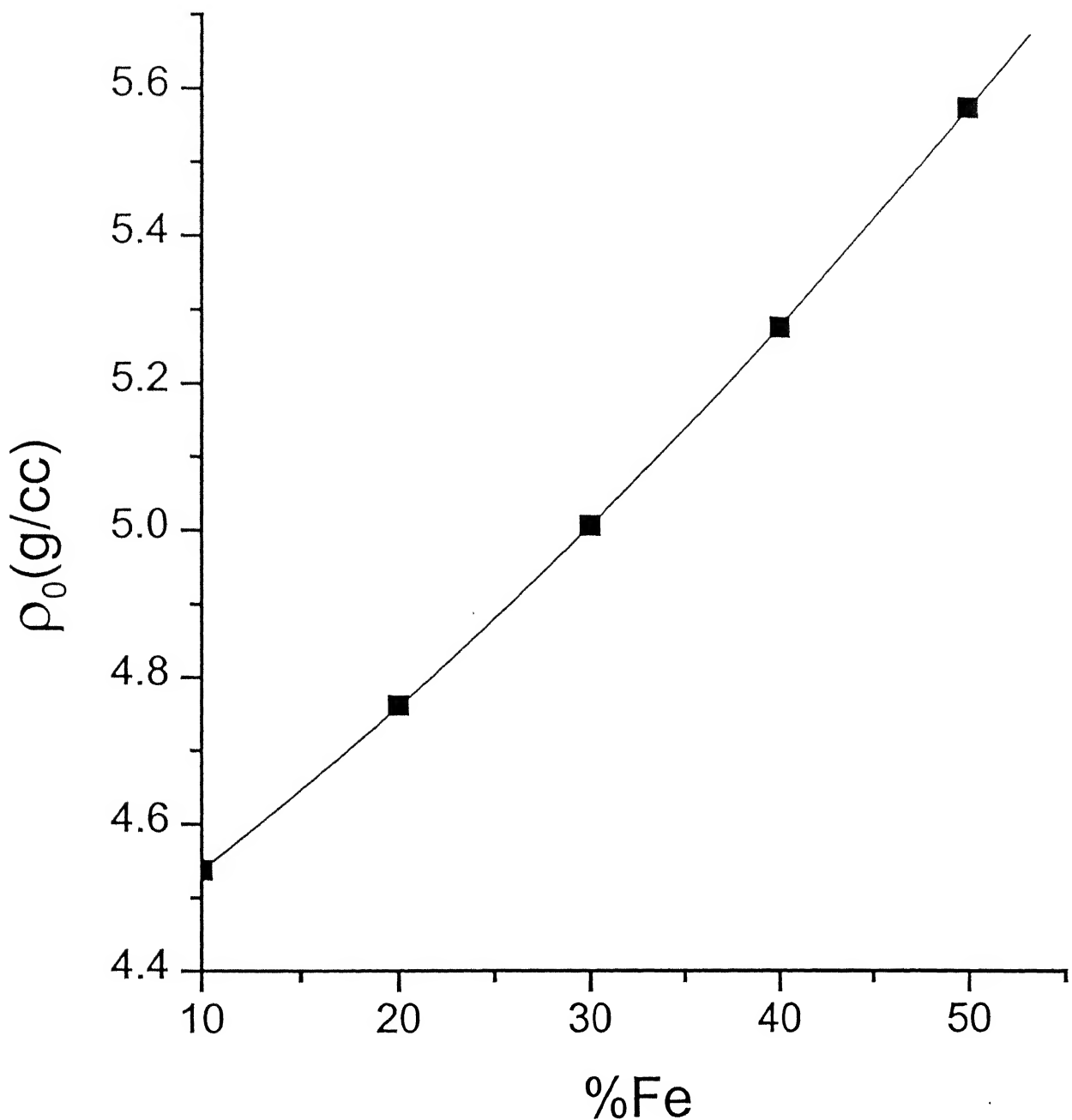


Figure 4.4: Plot showing variation of theoretical density of the fully dense iron-iron aluminide composite material( $\rho_0$ ) with variation in iron content (%Fe)

#### 4.2.3 Effect of Pressure

Effect of pressure on 50 wt% Fe compact is shown in Figure 4.5 and table 4.3. Figure 4.5 shows the variation of relative density  $\rho_{\text{rel}}$  with the applied pressure. This behavior is typical of powder samples under cold compaction.

### 4.3 SINTERING OF IRON-IRON ALUMINIDE GREEN COMPACTS

It is desirable to study the microstructural evolution during sintering of iron aluminide and iron-iron aluminide powder mixtures and/or their compacts. However, due to the limited amount of iron aluminide powder available, the sintering experiments could not be done on a large number of samples. Therefore, as explained in chapter 3, sintering experiments were undertaken on green compacts prepared from iron-iron aluminide powder mixtures containing 0% Fe, 5% Fe and 12% Fe respectively. The sintering was carried out under LR grade pure argon atmosphere at the temperatures of 1100°C, 1150°C and 1200°C, i.e. at 0.90  $T_m$ , 0.94  $T_m$  and 0.97  $T_m$  respectively, where  $T_m = 1250^\circ\text{C}$  corresponding to  $\approx 60\%$  Fe in the binary mixture, for periods of 1, 2, 3 and 4 hrs at 1100°C and 1150°C and 1 and 2 hrs at 1200°C. However, it was observed that some of the compacts underwent delamination during sintering presumably due to the micro-level lamination and poor bonding occurring during cold pressing. Therefore, reliable measurements related to sintered density could not be undertaken in the present study. The

**Table 4.3**  
**% Density Vs. Load (% Fe=50)**

$$\rho_0 = 5.5961$$

Sl.No.	Pressure (kg/cm <sup>2</sup> )	$\rho$ (g/cc)	$\rho_{rel}$
1	50	3.864	69.04
2	100	4.075	72.81
3	200	4.579	81.82
4	300	4.660	83.27
5	325	4.753	84.93

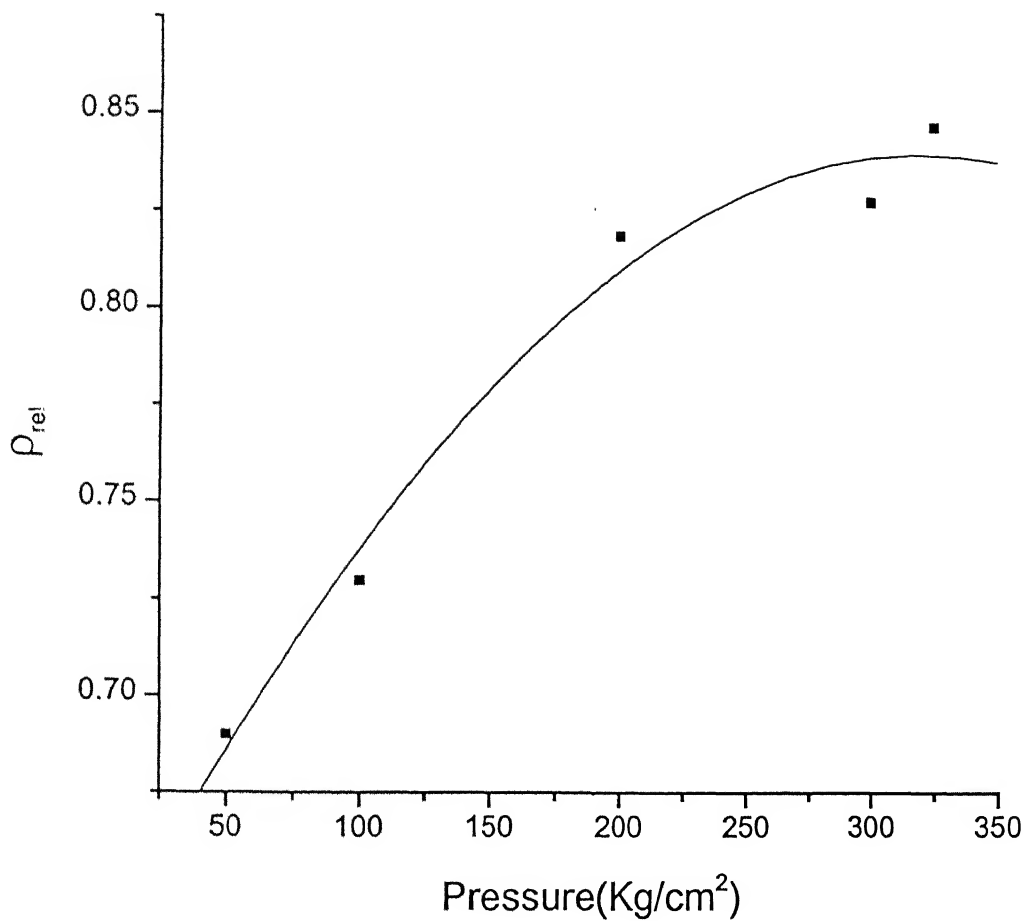


Figure 4.5: Plot of variation in  $\rho_{rel}$  with compaction pressure

following sub-sections describe results obtained on microstructural development and micro-hardness of sintered iron aluminide and iron-iron aluminide compacts.

#### **4.3.1 Microstructural Evolution during Sintering**

Optical micrographs of sintered compacts prepared from only iron aluminide powder are shown in Figures 4.6-4.8. As shown in these Figures, iron aluminide particles at all sintering temperatures maintained their characteristics regarding flat and sharp-edged surfaces. Further, as shown clearly in Figure 4.8 (i.e. for the compact sintered at 1200°C for 2 hours) the finer aluminide particles formed by the fracture of some of the particles during cold compaction also maintained their surface characteristics. Such observations indicate that the sintering in iron aluminide, inspite of being carried out at a temperature as high as 0.97  $T_m$ , occurs in a very sluggish manner. Though the diffusivity data for  $\text{FeAl}_2$  and  $\text{Fe}_2\text{Al}_5$  is not available in the literature, the diffusion in intermetallic phases is known to be sluggish. The retention of particle surface characteristics in sintered iron aluminide compacts can thus be interpreted in terms of slower diffusion in the ordered intermetallic structure of the aluminide phase. Due to the very sluggish sintering kinetics of iron aluminide compacts, the density of sintered compacts was found to be non-uniform in most compacts. The inhomogeneous densification of compacts is clear from figures shown.

Optical micrographs of sintered compacts prepared from iron-iron aluminide powder mixtures are shown in Figures 4.9-4.12. The general

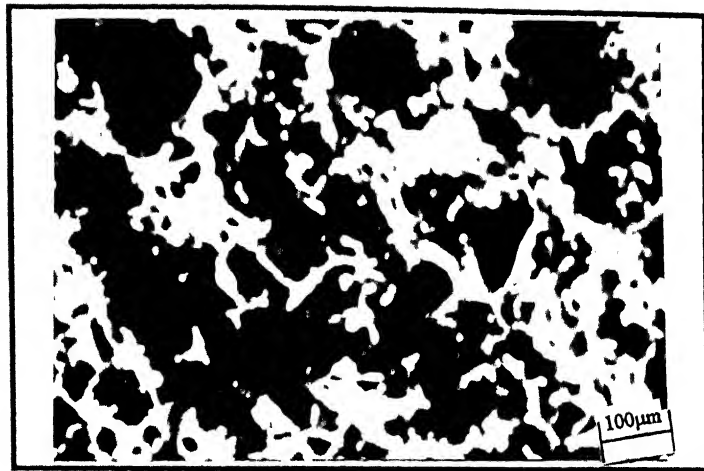


Figure 4.6     Optical micrograph of Iron aluminide compact sintered at  $1100^{\circ}\text{C}$  for 1 hr.

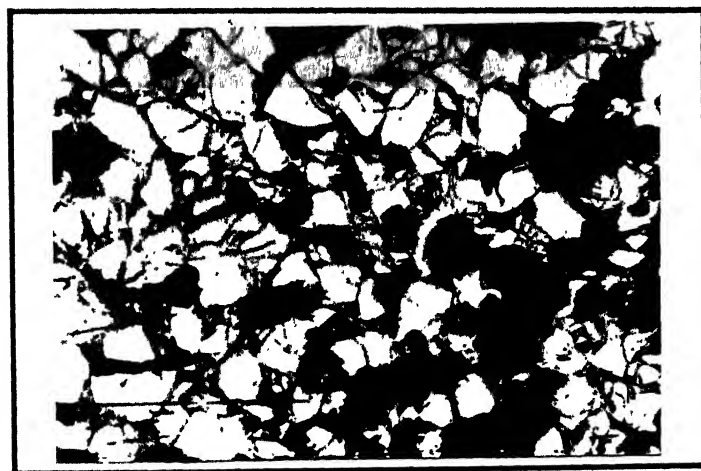


Figure 4.7     Optical micrograph of Iron aluminide compact sintered at  $1200^{\circ}\text{C}$  for 1 hr.

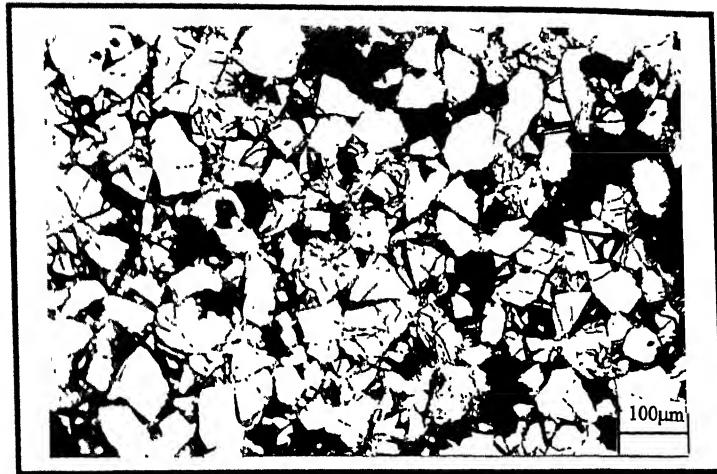


Figure 4.8      Optical micrograph of iron aluminide compact sintered at  $1200^{\circ}\text{C}$  for 2 hrs.

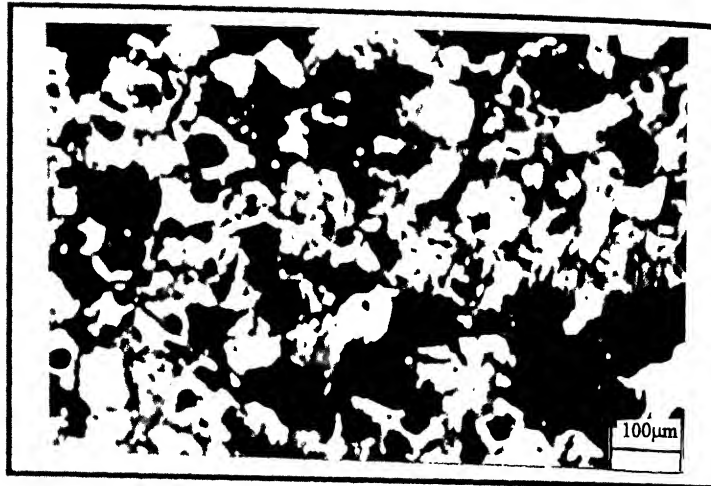


Figure 4.9(a) Optical micrograph of Iron(5%)-Iron aluminide compact sintered at  $1100^{\circ}\text{C}$  for 2 hr.



Figure 4.9(b) Optical micrograph of Iron(5%)-Iron aluminide compact sintered at  $1100^{\circ}\text{C}$  for 3 hr.

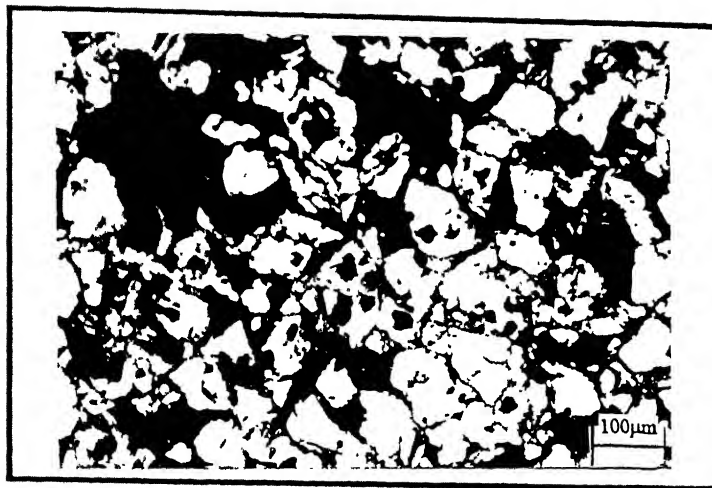


Figure 4.10(a) Optical micrograph of Iron(5%)-Iron aluminide compact sintered at  $1150^{\circ}\text{C}$  for 4 hr.



Figure 4.10(b) Optical micrograph of Iron(5%)-Iron aluminide compact sintered at  $1200^{\circ}\text{C}$  for 2 hr.



Figure 4.11(a) Optical micrograph of Iron(12%)Iron aluminide compact sintered at  $1150^{\circ}\text{C}$  for 4 hr.

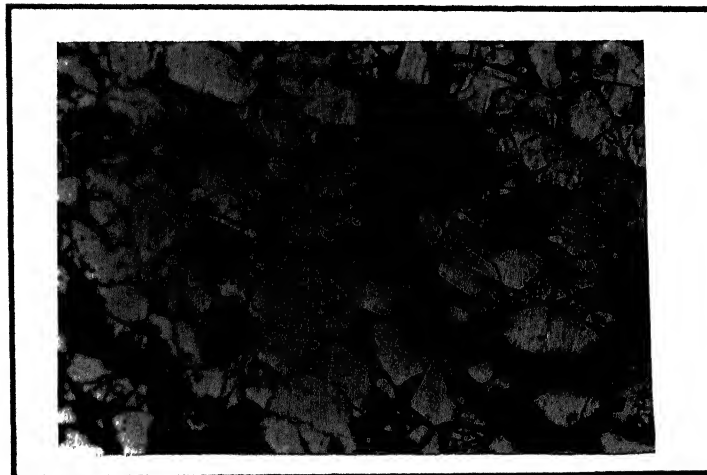


Figure 4.11(b) Optical micrograph of Iron(5%)-Iron aluminide compact sintered at  $1200^{\circ}\text{C}$  for 2 hr.



Figure 4.12 Optical micrograph of Iron(12%)-Iron aluminide compact sintered at  $1200^{\circ}\text{C}$  for 1 hr.

feature, as observed through metallography of sintered iron-iron aluminide compacts, was that the pores were distributed in an inhomogenous manner similar to that found in the case of sintered iron aluminide compacts (Figure 4.6). However, definite changes in particle shape characteristics were observed in these compacts. As pointed out in the previous section, angular shape and flat surfaces of aluminide particles were maintained even after sintering at as high as  $0.97 T_m$  in iron aluminide sintered compacts which had no iron addition. In contrast, the particle surfaces became rounded after the sintering of iron-iron aluminide compacts containing both 5% as well as 12% Fe. The rounding of aluminide particle surfaces may be attributed to an enhanced diffusion of atoms due to the presence of iron particles in the compacts. Though diffusivity data for Fe and Al atoms in crystal lattices of  $FeAl_2$  and  $Fe_2Al_5$  is not available, it may be concluded from the binding energy considerations that the diffusivity of Al atoms in the lattice of Fe is more than the diffusivity of Fe and/or Al atoms in the ordered crystal lattices of  $FeAl_2$  and  $Fe_2Al_5$ . This enhanced diffusivity of Al atoms in iron-iron aluminide compacts thus promotes the rounding of particles as clearly visible in Figures 4.9-4.12. However, the extent of rounding of surfaces was generally found to be increasing with the sintering temperature, sintering time and reduction in aluminide particle size.

Another noticeable feature observed in sintered compacts prepared from iron-iron aluminide powders was the presence of rounded pores within several particles. This observation is in contrast to features

observed in microstructures of sintered compacts prepared from aluminide powder. As suggested above, the diffusivity of Al atoms is expected to be much higher than that of Fe atoms in the present system. Therefore, the difference in rates of transportation of these atoms is likely to give rise to Kirkendal porosity. The presence of round pores within particles of sintered iron-iron aluminide compacts may thus be attributed to the Kirkendal effect.

#### 4.3.2 Hardness of Sintered Compacts:

It has been shown in the previous section that the angular shape of aluminide particles acquired rounded shape in sintered iron-iron aluminide compacts. The rounding of particles was attributed to the diffusion of Al atoms in iron particles during the sintering. In order to assess the process of homogenization of the chemical composition in iron-iron aluminide compacts during their sintering microhardness measurements were made. At least 10-15 indentations were made on each sintered sample. The values obtained on compacts sintered for shorter periods were observed to be falling in two distinct hardness value ranges. From the microhardness measurements, therefore, the average hardness values for softer and harder regions were calculated. The variation of microhardness values of softer and harder regions in samples prepared from 12% iron-iron aluminide compacts, sintered at 1100°C, as a function of sintering time is shown in Figure 4.13 as a bar chart. It is obvious from this Figure that while the hardness of the harder phase, i.e. aluminide particles, decreased with increasing the sintering

time, that of the softer phase, i.e. iron particles, increased during this interval. From the Figure 4.13 it can also be inferred that a sintering time of 4 hours at 1100°C was sufficient for the homogenization of iron-iron aluminide compacts containing 12% Fe. To study the effect of Iron/Aluminium content of the chemically homogeneous aluminide formed during sintering the microhardness measurements were made on compacts containing 0%, 5% and 12% Fe sintered for 4 hours at 1100°C. Microhardness values of these compacts as a function of their iron content are shown in Figure 4.14. It is clear from this Figure that as %Fe increases in the compact the hardness value of the chemically homogenized aluminide phase decreases.

The binary Fe-Al phase diagram, Figure 2.2, shows the presence of several intermetallic iron-aluminium compounds. While  $Fe_3Al$  and  $FeAl$  compounds exist in a wide compositional range,  $FeAl_2$ ,  $Fe_2Al_5$  and  $FeAl_3$  are confined to very narrow compositional range and can be considered as line compounds. The latter phases are, therefore, more brittle in nature. As described in Section-4.1, the iron aluminide powder used in the present study comprised of  $FeAl_2$  and  $Fe_2Al_5$  phases. Its consolidation behaviour by cold compaction was therefore found to be difficult and could be improved by the addition of Fe, which served as a binder. The sintering of compacts prepared from (a) iron aluminide powder and (b) iron-iron aluminide powder mixtures, was aimed for achieving an improved densification of the aluminide compacts and an

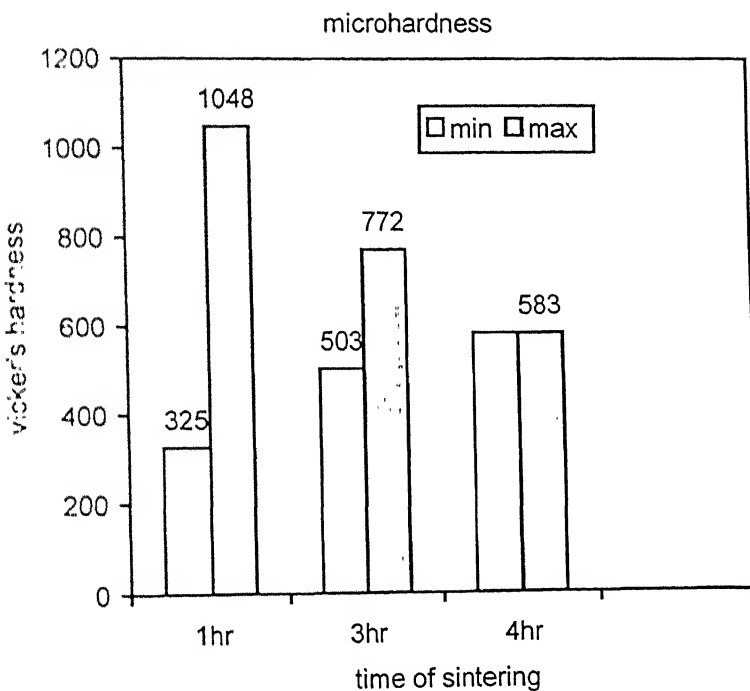


Figure 4.13: Bar Chart showing variation of microhardness with duration of sintering for compacts containing 12% Fe and sintered at  $1100^{\circ}\text{C}$ .

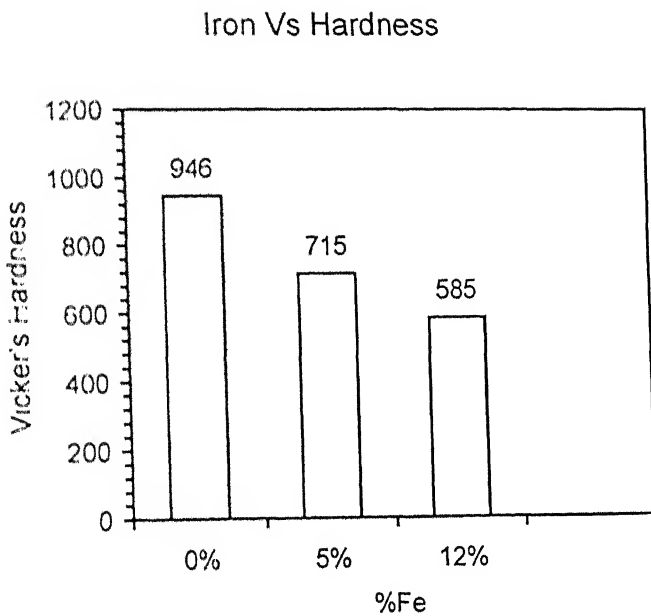


Figure 4.14: Bar chart showing average microhardness values of samples with varying iron content after sintering for 4 hours at  $1100^{\circ}\text{C}$  .

improved densification as well as chemical homogenization of iron-iron aluminide compacts.

The results described in the current section show that elimination of porosity in aluminide as well as in iron-iron aluminide compacts did not occur in a very effective manner during sintering at 1100°C, 1150°C and 1200°C. The distribution of pores is also found to be somewhat inhomogeneous in sintered compacts. Due to the lower sintered-density of compacts, the Rockwell hardness of samples could not be measured as efforts made in this direction lead to their fracture.

On the other hand, as shown by the microhardness data, the near-complete homogenization of the chemical composition is achieved for the sintering time interval of 4 hours. Homogenization of the chemical composition of sintered compacts appears to be occurring by the diffusion of Al atoms and is reflected by: (a) the presence of rounded particles as obtained in iron-iron aluminide sintered compacts in contrast to pure aluminide sintered compacts (b) the presence of round Kirkendal pores within particles (c) the decrease in the difference of microhardness values of softer and harder particles with increasing sintering time. Further, it has been shown that the hardness of iron-aluminium intermetallic compounds increases by increasing their aluminium content. The decrease of the average hardness values of iron-iron aluminide sintered compacts as a function of (a) sintering time in Figure 4.13 and (b) the increasing iron content in Figure 4.14 can be understood in this manner.

## 4.4 HOT PRESSING OF IRON ALUMINIDE AND IRON-IRON ALUMINIDE POWDER MIXTURES

### 4.4.1 General

As discussed earlier, the objective of the present study was the development of multi-phase iron aluminides and iron-iron aluminide composites by the P/M route. Results described in sections 4.2-4.3 of the present chapter show that:(a) cold die-compaction of the given iron aluminide powder, which essentially comprises of  $FeAl_2$  and  $Fe_2Al_5$  phases, was not very effective, (b) cold-die compaction of iron-iron aluminide powder was possible provided that sufficient care is taken to eliminate the lamination in green compacts, (c) porosity in sintered compacts is high and the distribution of pores in sintered iron-iron aluminide compacts is not homogeneous and (d) a nearly complete chemical homogenization occurs in iron-iron aluminide compacts during their sintering at  $1100^{\circ}C$  for 4 hours. Study of hot consolidation behaviour of iron aluminide and iron-iron aluminide powder mixtures was therefore, undertaken by the hot processing route. Thus, an effort was made to hot roll a limited number of porous compacts prepared by the sintering of iron-iron aluminide powder compacts. The hot rolling was done at  $1000^{\circ}C$  after a soaking time of 30 minutes. However, the hot-rollability of these sintered compacts was found to be very poor and compacts completely crumbled during their hot rolling.

Hot pressing, being a commercially viable consolidation route for P/M processing of materials, was tried for the development of multi-

phase iron aluminides and iron-iron aluminide composites. Further, in view of the nearly complete chemical homogenization obtained in iron-iron aluminide powder mixtures containing 12 wt% iron during their sintering, the powder mixtures used for hot pressing studies contained 0%, 10%, 15%, 20%, 30%, 40% and 50% of Fe by weight. The hot pressing details are already described in chapter 3. Essentially, most of the hot pressing experiments were done at the temperatures of  $0.6 T_m$ ,  $0.63 T_m$  and  $0.7 T_m$  of the starting aluminide powder. All hot pressed compacts, including those containing no iron, were found to be coherent without any lamination problem.

#### 4.4.2 Identification of Phases Formed During Hot Pressing

Phase identification in hot pressed samples was done using the X-ray diffraction technique. Characteristic plots from a few of the hot pressed samples are shown in Figures 4.15-4.20. Identification of phases was done using the diffraction data given in table 4.1 and peaks were marked with their corresponding phases. The data from all the samples are shown in table 4.4.

It is to be noted that up to the hot pressing temperature of  $700^\circ\text{C}$ , no new phase forms and the phases present in the compacts are only those which are already there in the starting material, i.e. Fe,  $\text{FeAl}_2$  and  $\text{Fe}_2\text{Al}_5$ .

On the other hand, for the hot pressing temperature of  $800^\circ\text{C}$ , iron added in the starting powder mixtures was not found to be present in detectable amount, in hot pressed samples. This is clear from the X-ray

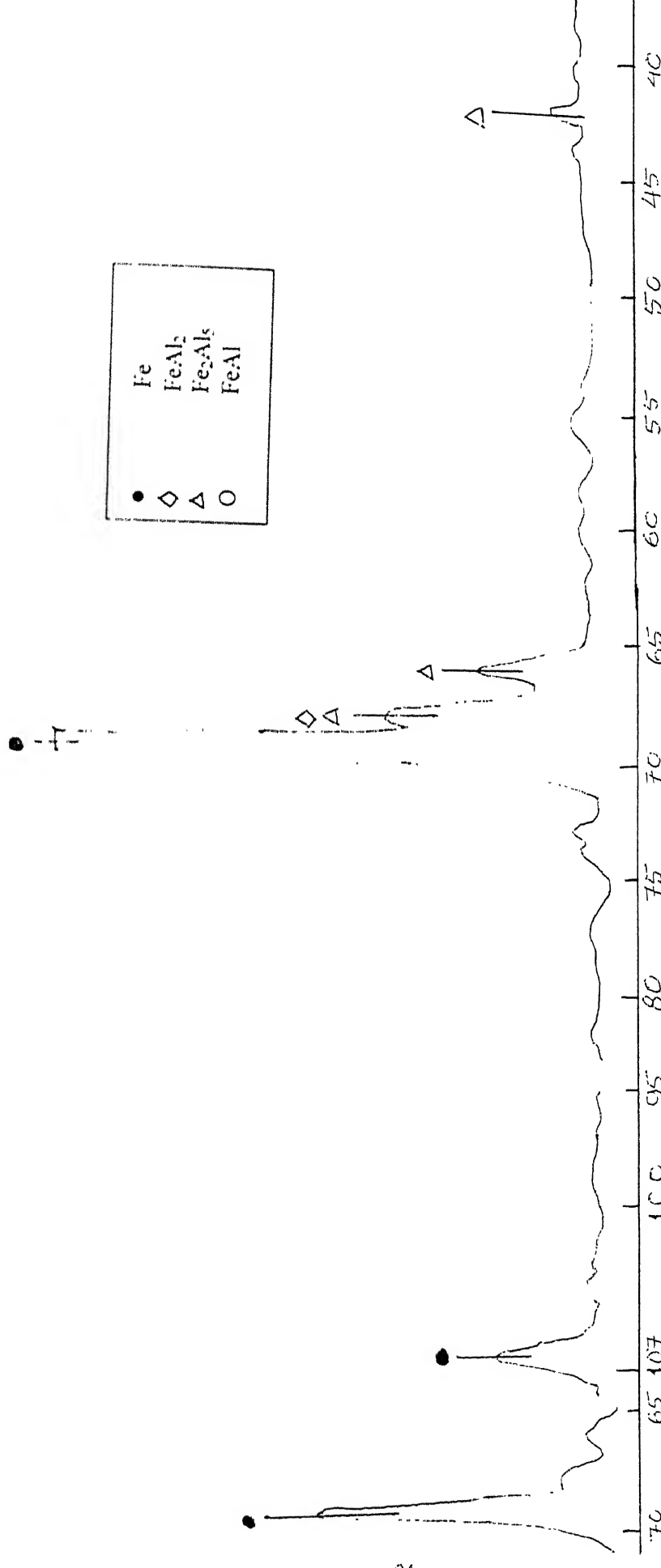


Figure 4 |5: X-Ray diffraction results of iron-iron aluminide sample Hot pressed at 650°C and containing 50% Fe by weight.

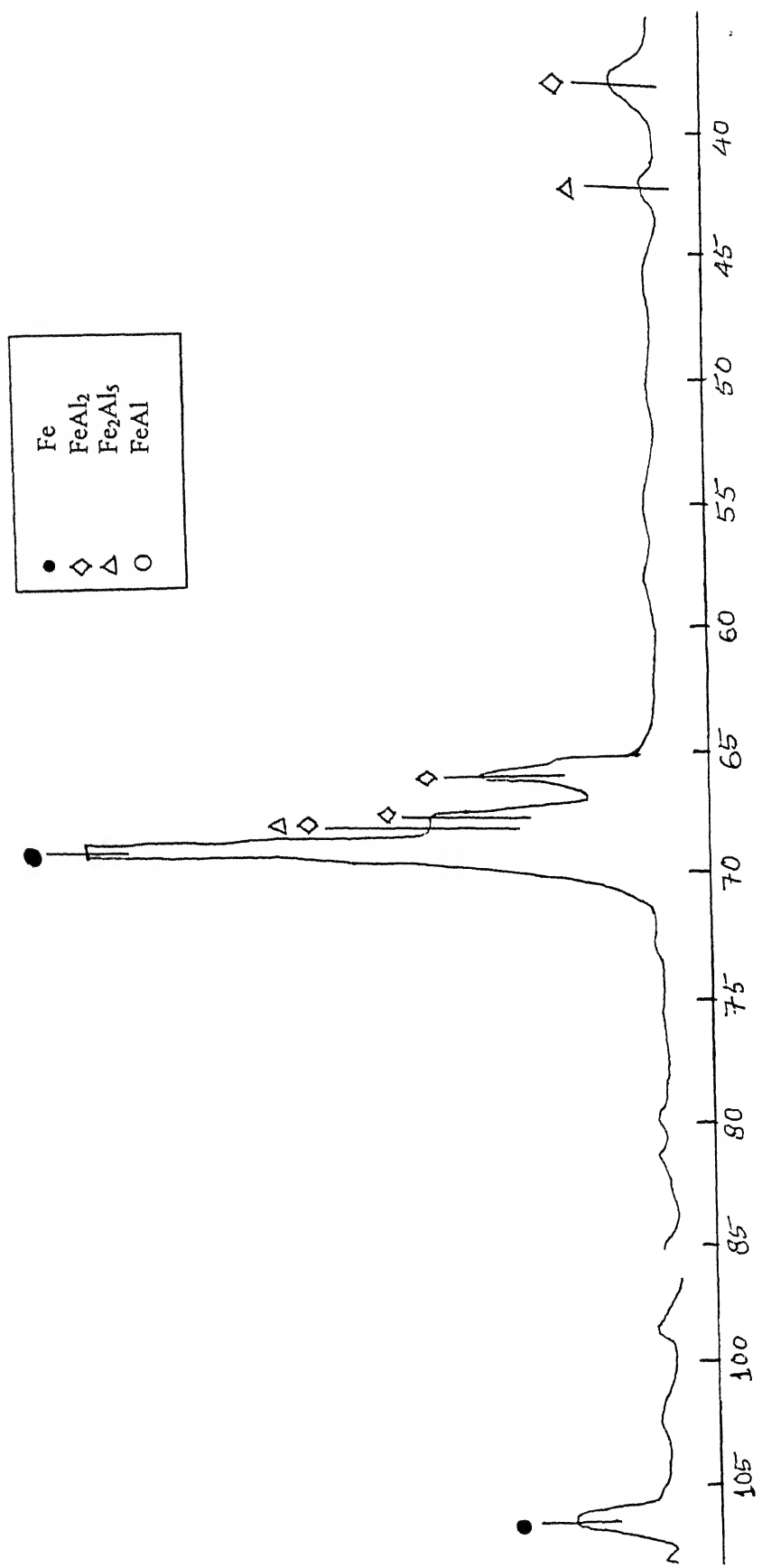


Figure 4.16: X-Ray diffraction results of iron-iron aluminide sample Hot pressed at 650°C and containing 40% Fe by weight.

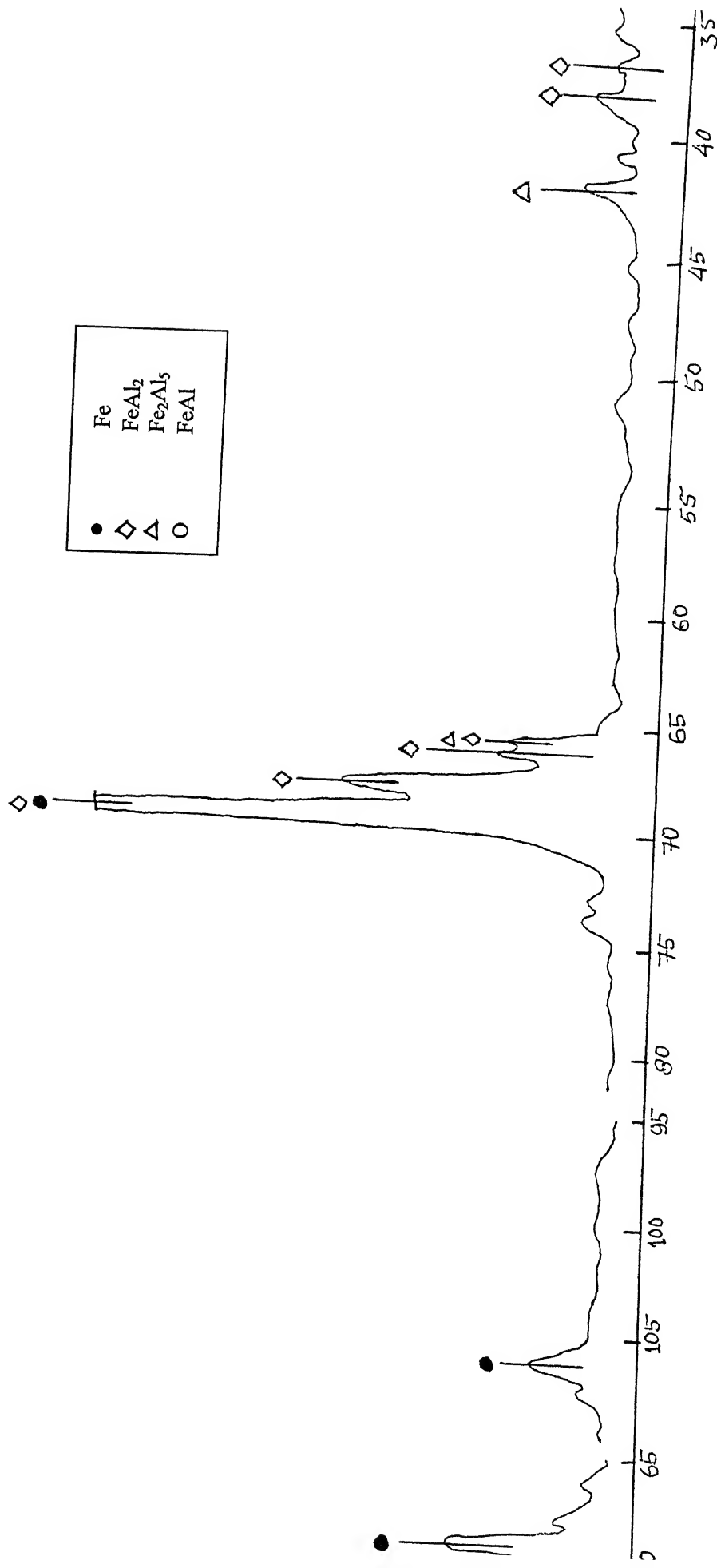


Figure 4.17: X-Ray diffraction results of iron-iron aluminide sample Hot pressed at 700°C and containing 30% Fe by weight.

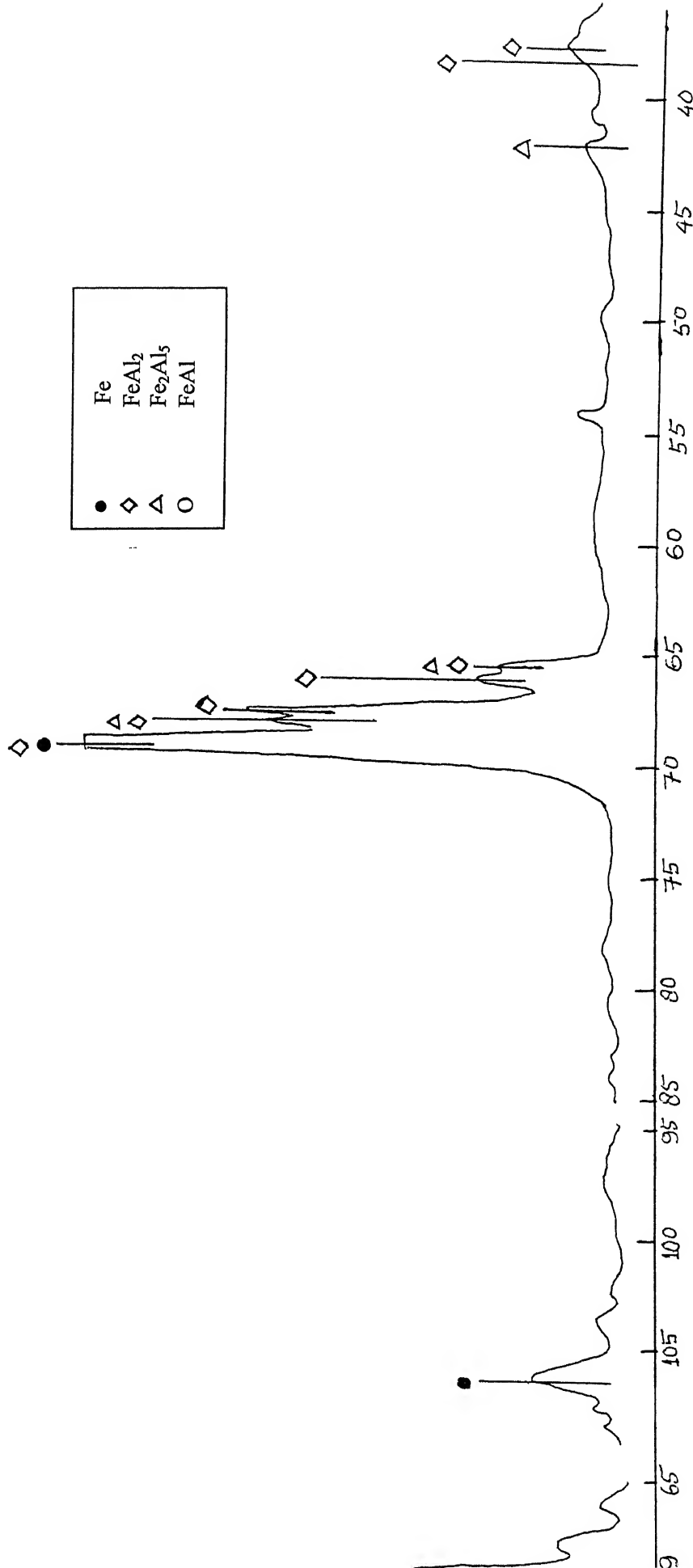


Figure 4.18 : X-Ray diffraction results of iron-iron aluminide sample Hot pressed at 700°C and containing 40% Fe by weight.

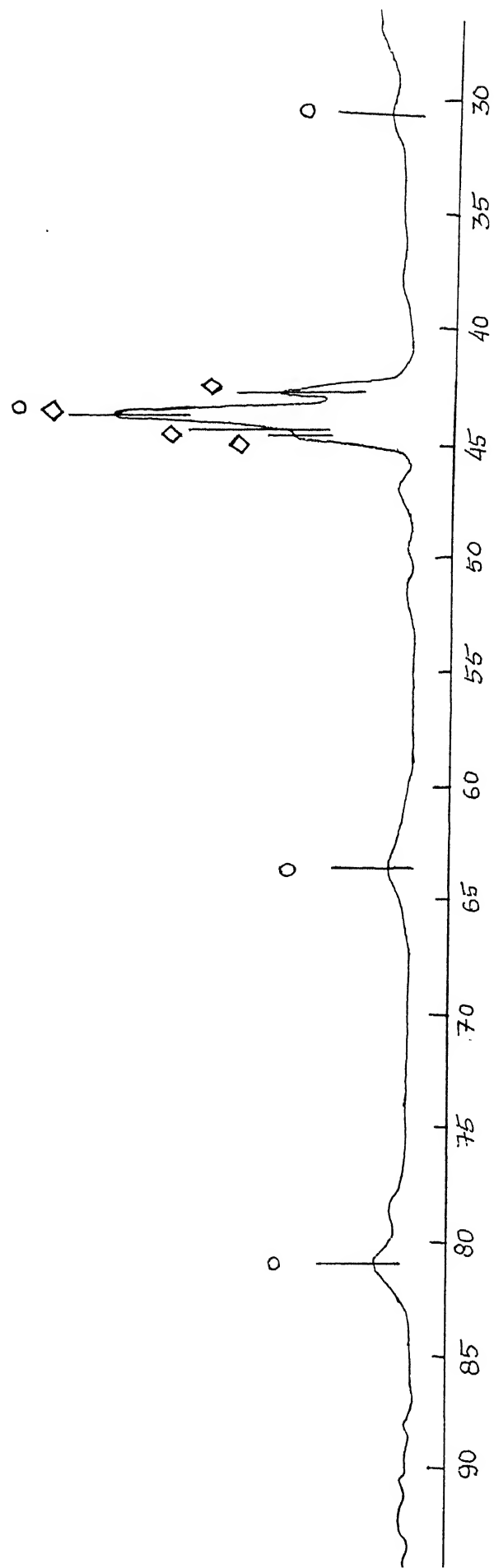
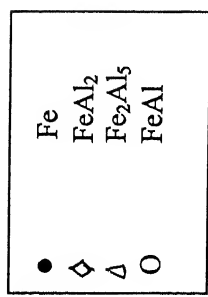


Figure 4.19 : X-Ray diffraction results of iron-iron aluminide sample Hot pressed at 800°C and containing 15% Fe by weight.

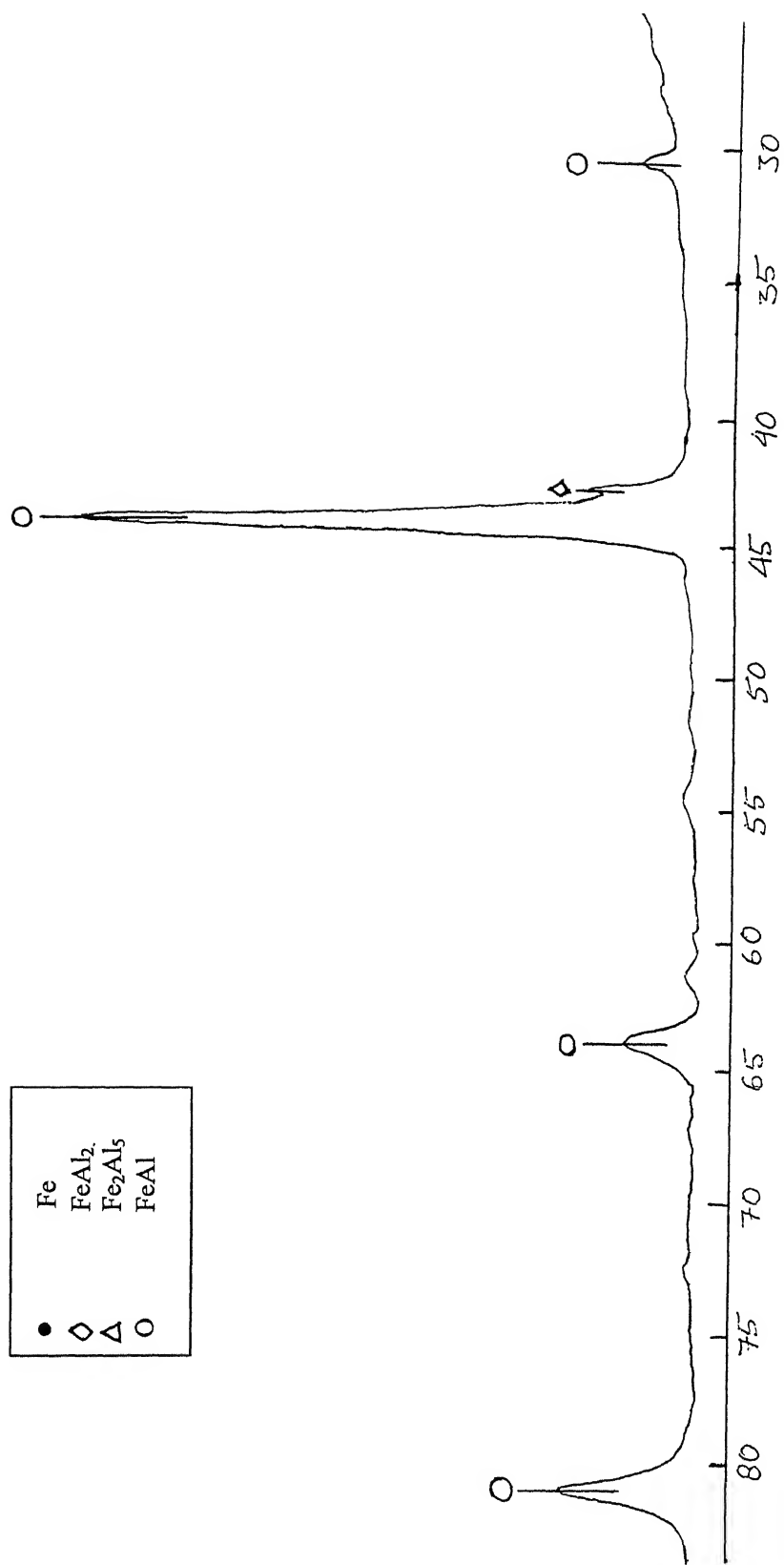


Figure 4.20: X-Ray diffraction results of iron-iron aluminate sample Hot pressed at 800°C and containing 40% Fe by weight.

**Table 4.4: X-Ray Diffraction Results Of Hot Pressed Samples.**

%Fe	650 °C	700 °C	800 °C
0	FeAl <sub>2</sub> , Fe <sub>2</sub> Al <sub>5</sub>	FeAl <sub>2</sub> , Fe <sub>2</sub> Al <sub>5</sub>	
10	Fe, FeAl <sub>2</sub> , Fe <sub>2</sub> Al <sub>5</sub>	Fe, FeAl <sub>2</sub> , Fe <sub>2</sub> Al <sub>5</sub>	
15	Fe, FeAl <sub>2</sub> , Fe <sub>2</sub> Al <sub>5</sub>	Fe, FeAl <sub>2</sub> , Fe <sub>2</sub> Al <sub>5</sub>	FeAl,FeAl <sub>2</sub>
20	Fe, FeAl <sub>2</sub> , Fe <sub>2</sub> Al <sub>5</sub>	Fe, FeAl <sub>2</sub> , Fe <sub>2</sub> Al <sub>5</sub>	
30	Fe, FeAl <sub>2</sub> , Fe <sub>2</sub> Al <sub>5</sub>	Fe, FeAl <sub>2</sub> , Fe <sub>2</sub> Al <sub>5</sub>	
40	Fe, Fe <sub>2</sub> Al <sub>5</sub> ,FeAl <sub>2</sub>	Fe,Fe <sub>2</sub> Al <sub>5</sub> ,FeAl <sub>2</sub>	FeAl
50	Fe, Fe <sub>2</sub> Al <sub>5</sub>		

diffraction results of hot pressed samples containing 15%Fe and 40% Fe shown in Figure 4.19 and Figure 4.20.

Another important observation made from X-ray diffraction results of samples hot pressed at 800°C was that the phases originally present in the initial powder started undergoing their modification. In 15% Fe hot pressed sample  $\text{Fe}_2\text{Al}_5$  phase was absent and a new phase FeAl was formed, whereas in 40% Fe sample both of the intermetallic phases which were present in the starting powder were almost absent in the hot pressed compact and the new phase FeAl was observed from the X-ray results.

Thus, the following interpretations may be made from X-ray diffraction results of hot pressed samples, as shown in table 4.4:

- (a) Iron–iron aluminide powder mixtures hot pressed up to 700°C provide the structures which contain iron as well as iron aluminide(s) and thus present the opportunity for developing composites containing varying amount of iron and iron aluminides in the material.
- (b) Hot pressing of iron-iron aluminide powder mixtures at temperatures of 800°C and above leads to the development of single/multiphase iron aluminide structures. For example, the structure formed by hot pressing the powder containing 15% Fe was found to comprise predominantly of FeAl and  $\text{FeAl}_2$  whereas hot pressed compact containing 40% Fe primarily comprised of FeAl.

#### **4.4.3 Densification and Microstructural Evolution During Hot Pressing:**

As discussed in Section 4.3 of this Chapter, compacts prepared by the cold pressing and sintering route had large volume fraction of porosity with non-uniform distribution of pores through out the sample as shown in figures 4.6-4.12. Further, iron aluminide particles, which to begin with had sharp edges and corners, became rounded during the course of sintering. Nearly full-density microstructures of samples prepared from iron-iron aluminide powder mixtures containing 10%, 15% and 40% Fe respectively by hot pressing at 800°C are shown in figures 4.21-4.23. These microstructures clearly indicate that it is possible to produce fully dense multi-phase iron aluminide or iron-iron aluminide composites by the hot pressing route provided that the right conditions for hot pressing are selected. The present section discusses the results of the densification of iron-iron aluminide powder mixtures and the development of other microstructural details in hot pressed compacts.

It is expected that the densification during hot pressing of iron-iron aluminide powder mixtures would depend on:(i) the iron content of the powder mixture, (ii) temperature of hot pressing, (iii) pressure applied and the homogeneity of its transmission through the powder aggregate in the die and (iv) the holding time. In addition particle sizes of iron as well as iron aluminide powders are also expected to play an important role during the densification by the hot pressing route.

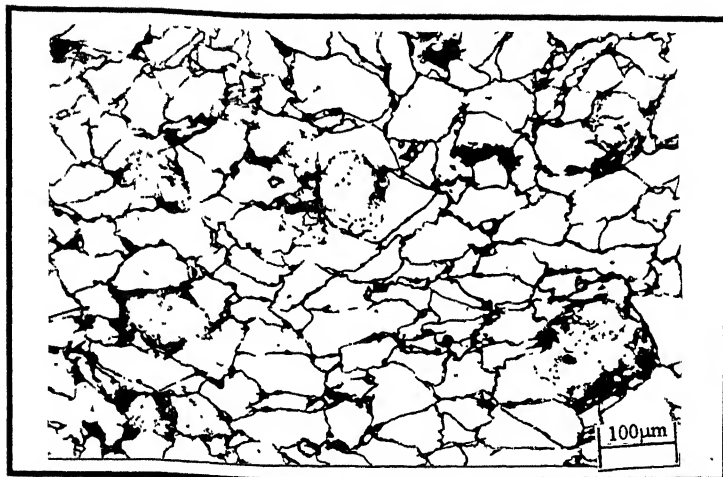


Figure 4.21 Full density Optical micrograph of 10%Fe sample Hot pressed at 800°C

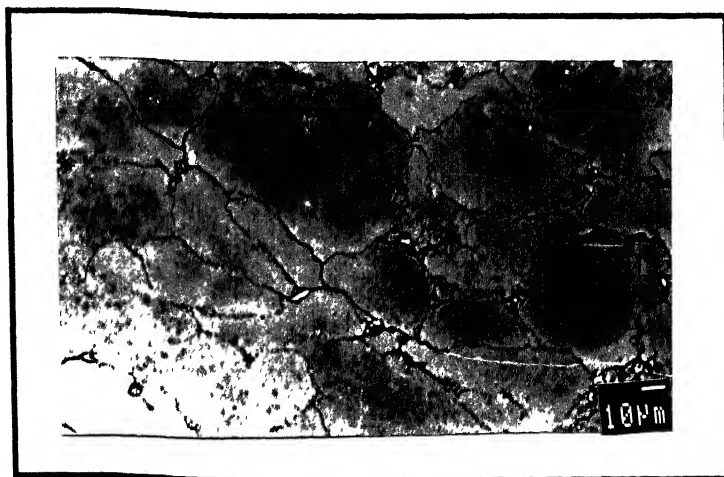


Figure 4.22 Full density scanning electron micrograph of 15%Fe sample Hot pressed at 800°C

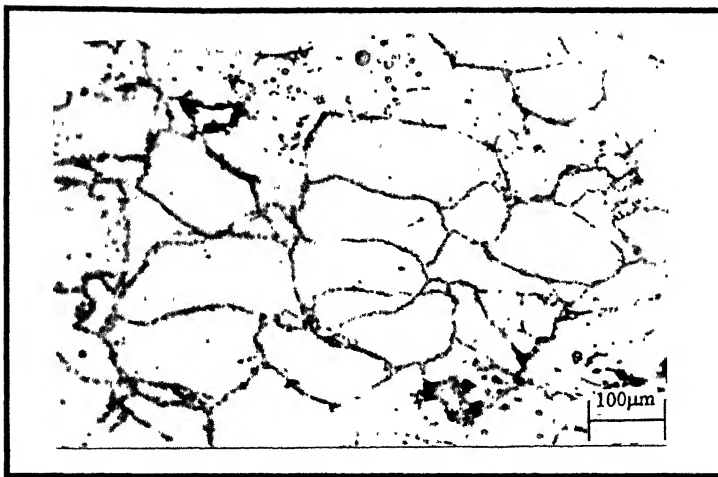
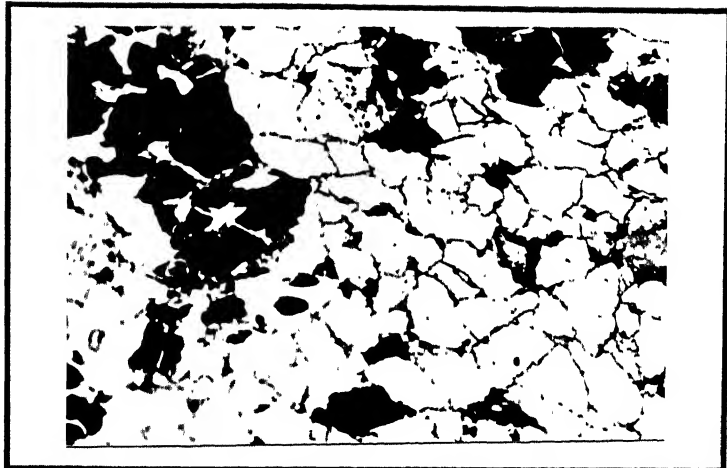


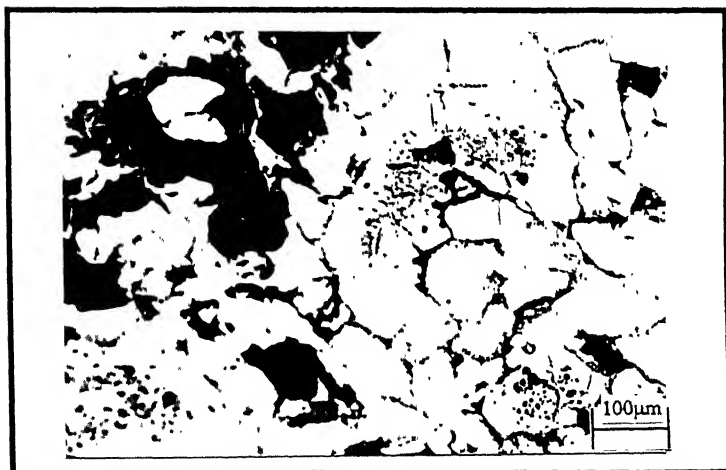
Figure 4.23 Full density scanning electron micrograph of 40% Fe sample Hot pressed at 800°C

Optical micrographs showing the elimination of porosity, as observed in different parts of the compact containing 10% Fe and hot pressed at the temperature of 800°C are shown in figure 4.24(a)-(e). These micrographs may be assumed to represent different stages of densification occurring in iron-iron aluminide powder mixtures. Similarly, micrographs of compacts showing advance stages of densification in compacts containing 15% and 40% iron respectively obtained by hot pressing at 800°C are shown in figure 4.25. The following observations regarding densification during hot pressing can be made from the micrographs shown in figures 4.24 and 4.25.

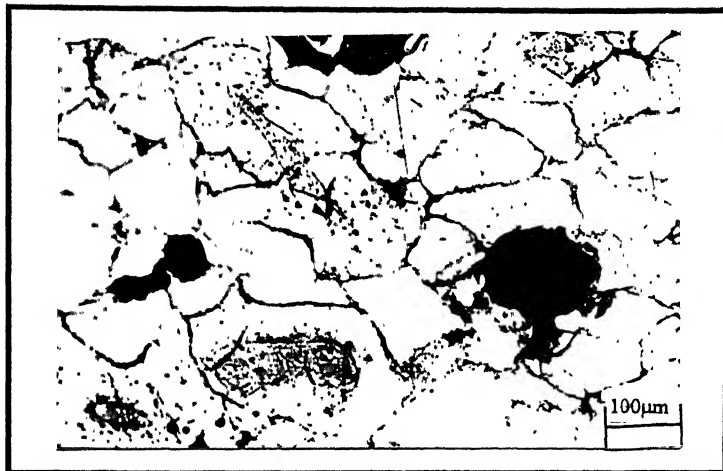
- (i) While a few particles in compacts, supposedly of iron, were found to undergo their substantial elongation, many other particles, presumably that of iron aluminide, were observed to maintain their original shape with angularities of edges and corners.
- (ii) The tendency for elongation in more particles increased with increasing the iron content in iron-iron aluminide powder mixtures [figure 4.24(c) and 4.25(a)].
- (iii) Some particles, specially during advanced stages of densification were observed to undergo their fracture, as shown in figures 4.25(b) and (c). For example the micrograph in figure 4.25(b) from the compact containing 15% Fe reveals small



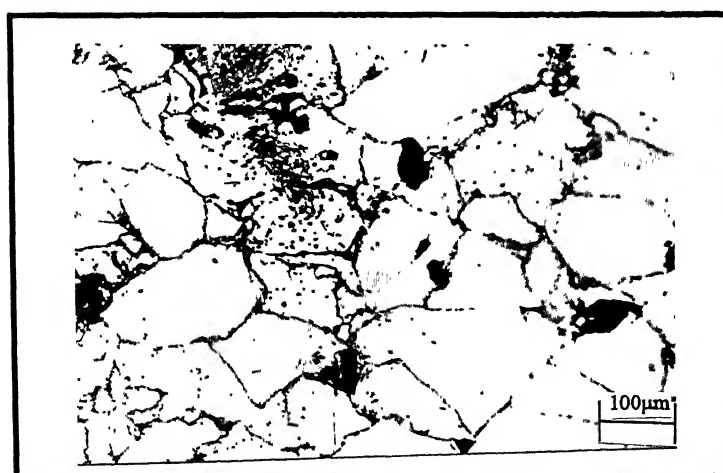
(a)



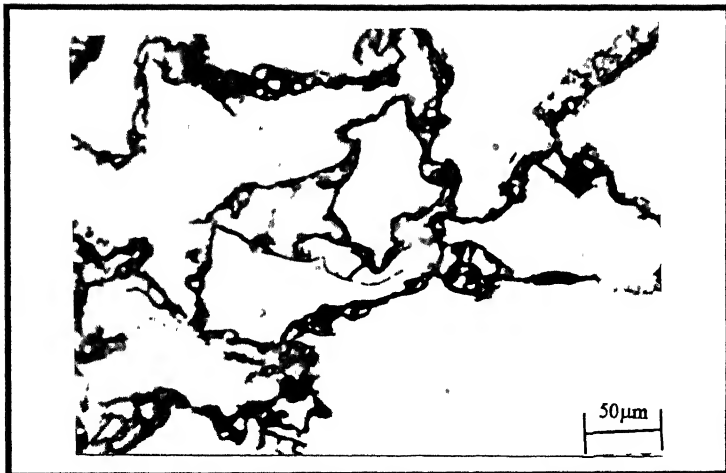
(b)



(c)

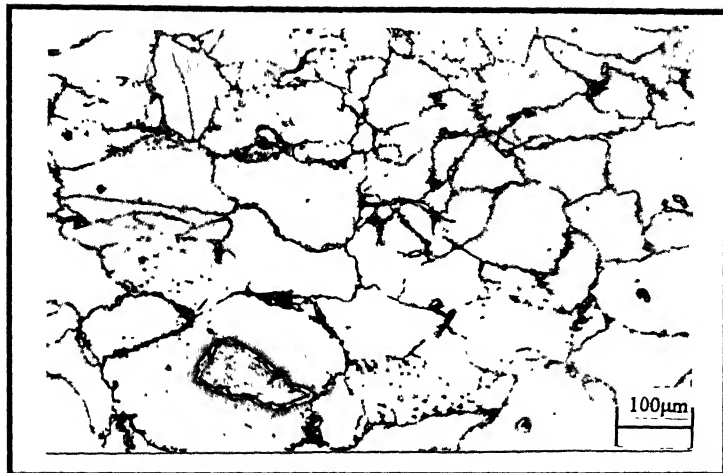


(d)



(e)

Figure 4.24(a-e) Optical micrograph of 10%Fe sample Hot pressed at  $800^{\circ}\text{C}$



(a)



(b)



(c)



(d)

Figure 4.25 Micrographs of Hot pressed samples showing advanced stages of densification during hot pressing at  $800^{\circ}\text{C}$ :  
(a) Optical micrograph of 40%Fe sample  
(b) Scanning micrograph of 15% sample  
(c) Scanning micrograph of 15% sample  
(d) Scanning micrograph of 15% sample

fragmented particles situated in a pore as well as some fragmented fines present in between coarse particles. These very small fragmented particles are also present at the particle boundaries in compact containing 40% Fe [Figure 4.25(c)], which shows a more dense region of the hot pressed sample. This micrograph can be thought of as an advance stage of densification to the earlier micrograph.

It is worth mentioning that hot pressing of iron-iron aluminide powder mixtures not only causes densification of the powder, it also helps in phase modification, as revealed by X-ray diffraction results shown in section 4.4.2, and consequent evolution of their morphology. These other aspects of microstructural changes involving formation of new phase(s) and their morphological distribution in the structure was indeed found to be occurring in samples prepared by the hot pressing route.

Figures 4.26(a) and 4.26(b) clearly show a well developed lamellar structure in sample containing 40% Fe prepared by hot pressing at  $800^{\circ}\text{C}$ . However, as shown in figure 4.26(b), the lamellar distribution of the phases was not found to be present in all the particles. The development of similar microstructural features was also found to be present in 15% Fe sample, as shown in figure 4.27. This type of morphology suggests that the two phases present in the sample get arranged in the form of lamellæ.



Figure 4.26(a) Scanning micrograph of 40%Fe sample Hot pressed at  $800^{\circ}\text{C}$  showing lamellar microstructure.



Figure 4.26(b) Similar micrograph as 4.26(a) but taken on EPMA at lower magnification.



Figure 4.27 Scanning micrograph of 15%Fe sample Hot pressed at  $800^{\circ}\text{C}$  showing lamellar microstructure.



Figure 4.28 An EPMA micrograph of 40%Fe sample (Hot pressed at  $800^{\circ}\text{C}$ ) showing typical trace of electron probe.

In order to find out the composition (at% Al) in the lamellar region, EPMA studies were done on the above two samples. These tests were done using a probe of  $0.1\mu\text{m}$  by traversing it in intervals of multiples of  $1\mu\text{m}$ . A typical micrograph showing the probe marks of the EPMA analysis in 40% Fe hot pressed sample is shown in figure 4.28. Results from the EPMA analysis thus obtained are shown in Figure 4.29(a) and 4.29(b). It is to be noted from figure 4.28 that the width of lamellae in well developed regions was either smaller or equal to that of the EPMA probe size. These EPMA results show that the composition in the two-phase regions of 40% Fe sample varies between 62.8 to 66 at% Al and that in 15% Fe sample lies in the range of 62 - 62.8 at% Al and centred around  $\approx 62$  at% Al. Dot-maps indicating the concentration of Fe and Al in such regions using EDAX analysis are shown in figure 4.30(a) and (b). It is worth mentioning that both of these compositions fall in  $\text{FeAl} - \text{FeAl}_2$  two-phase field in the Fe-Al binary phase diagram shown in Figure 2.2.

It has already been shown in figure 4.26(a) and (b) that the development of the lamellar structure was not uniform and several grains in hot pressed compacts had either undeveloped or partially developed two-phase microstructures. Therefore, EPMA studies were also done in such regions in two mutually perpendicular directions. Variation of composition as a function of distance in one such region of a sample containing 40% Fe, hot pressed at  $800^\circ\text{C}$ , is shown in Figures 4.31(a) and 4.31(b). These results show that there existed a continuous variation of Al in grains, from nearly 0 at% Al at the centre to a maximum at grain

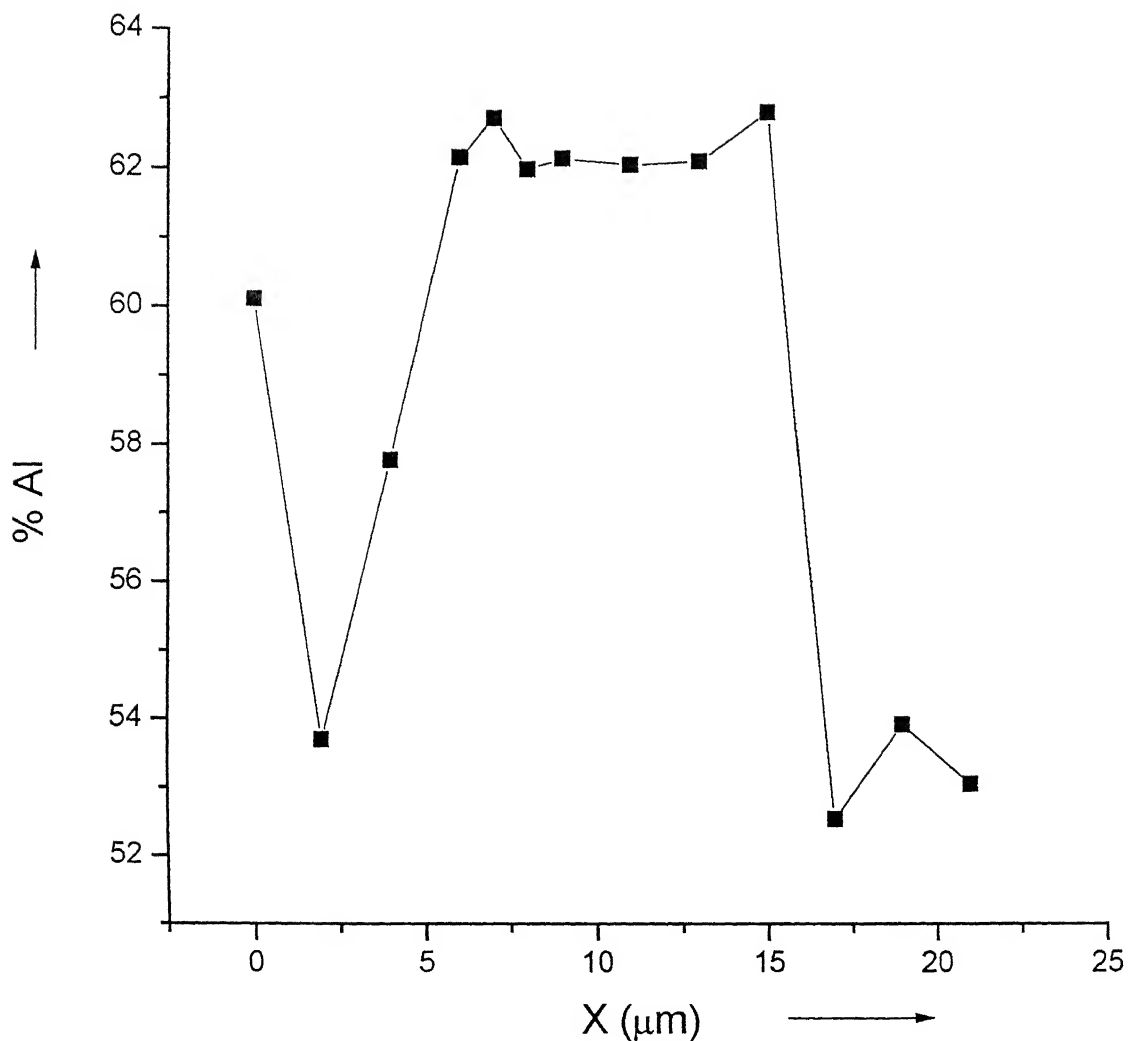


Figure 4.29(a) Plot showing variation of %Al in the 15%Fe sample(Hot pressed at  $800^0\text{C}$ ) around lamellar region.

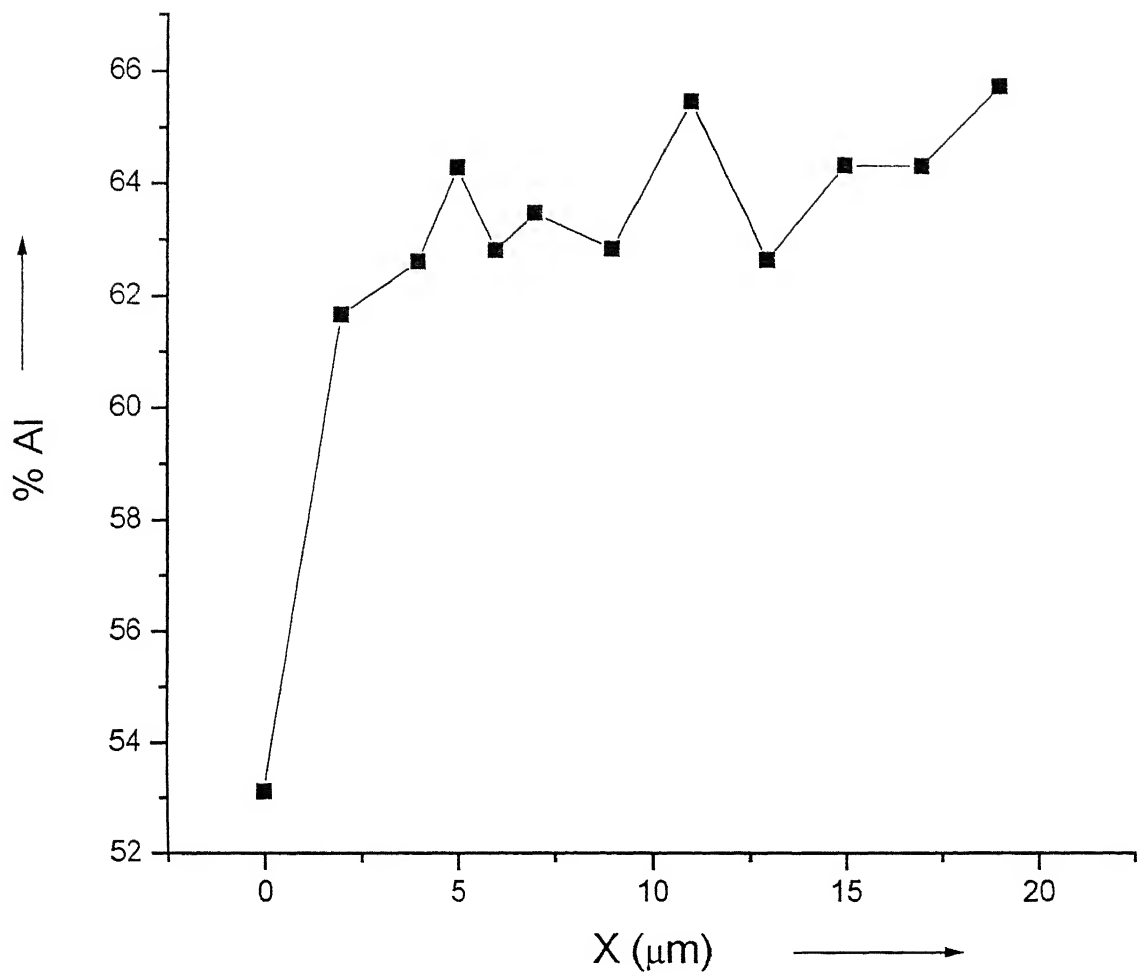


Figure 4.29(b) Plot showing variation of %Al in 40%Fe sample (Hot pressed at  $800^0\text{C}$ ) around lamellar region.

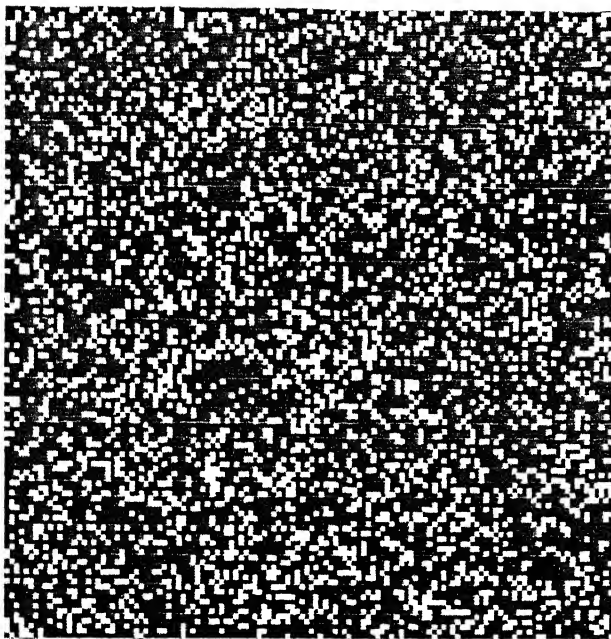


Figure 4.30(a) EDAX dot map showing distribution of Al in 40% sample.

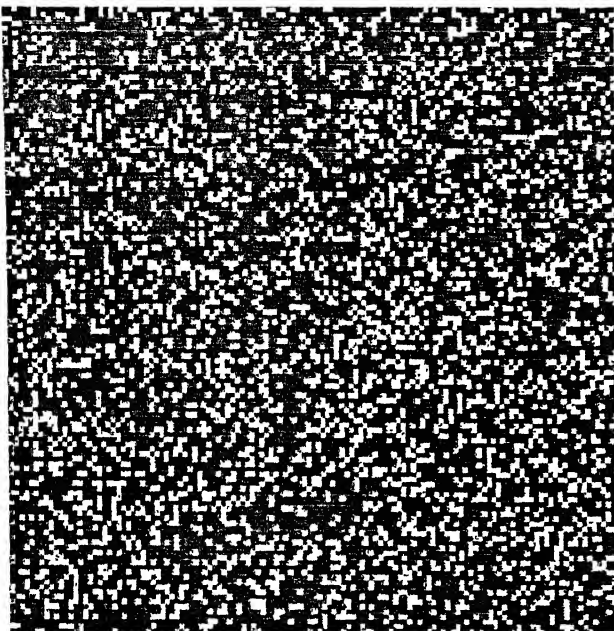
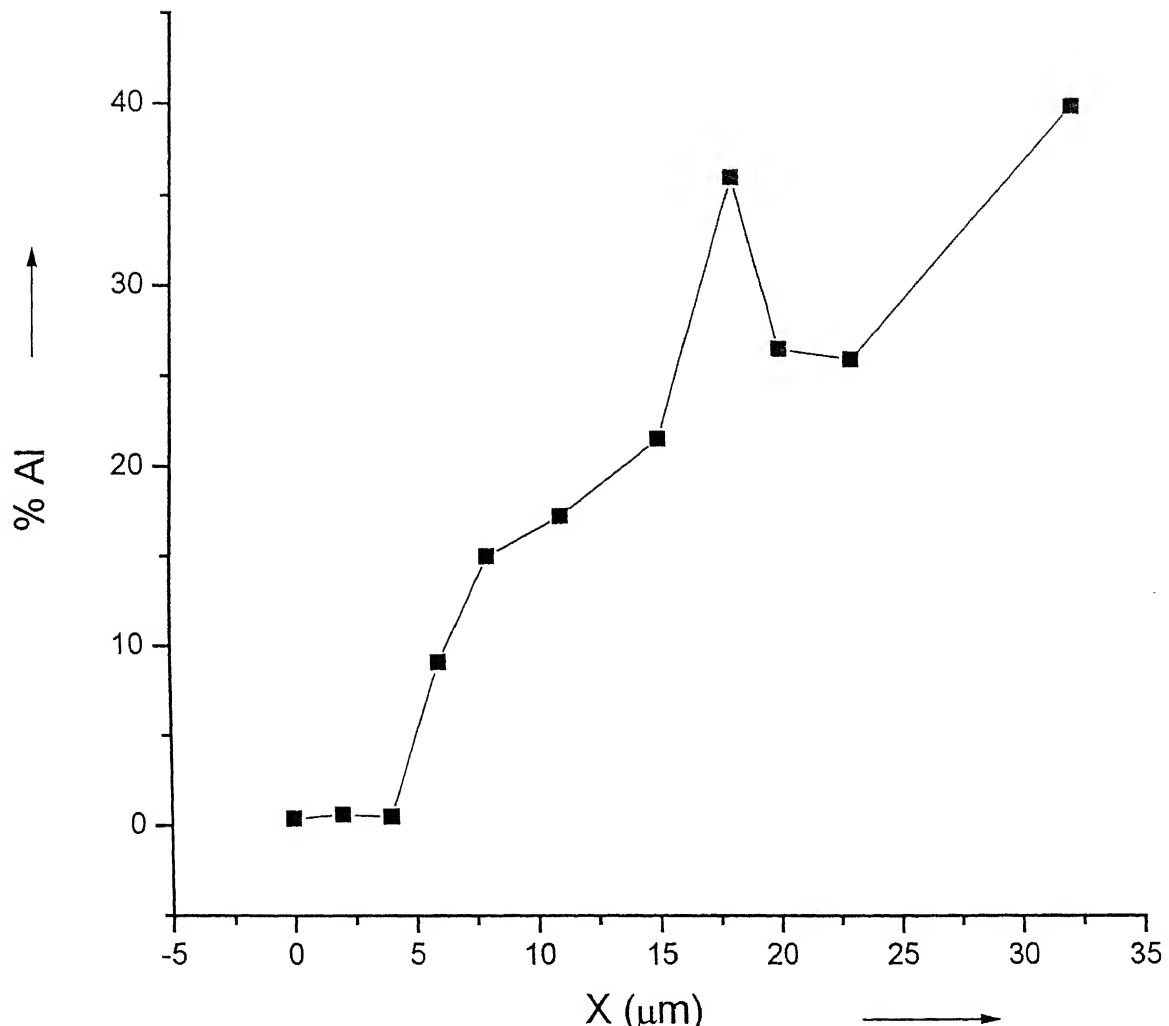
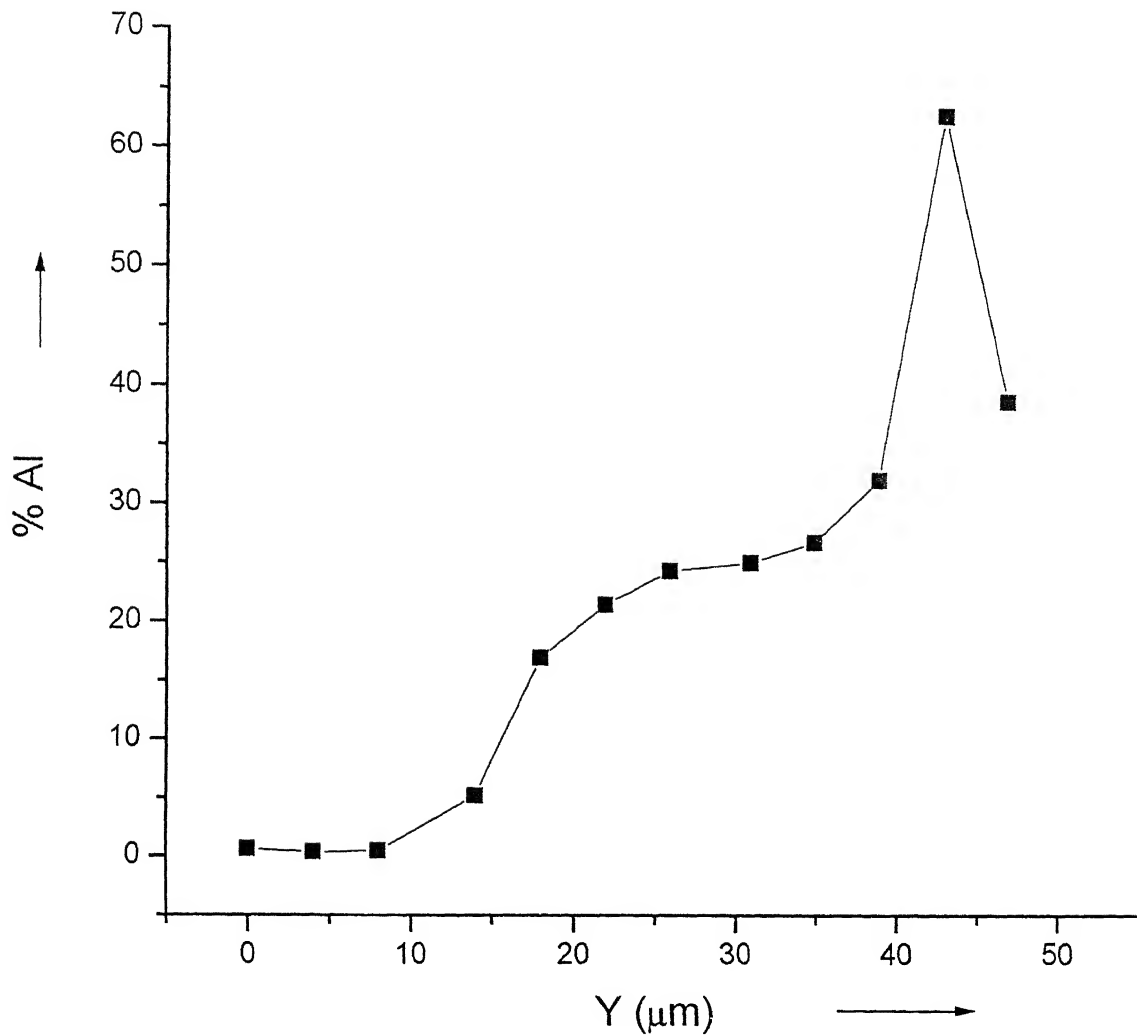


Figure 4.30(b) EDAX dot map showing distribution of Fe in 40% sample.



( $\alpha$ )



(b)

Figure 4.31 Plots showing variation of %Al in 40%Fe sample((Hot pressed at  $800^0\text{C}$ ) in non lamellar region in two mutually perpendicular direction

boundary. Though there was a steady increase of Al content from the grain centre to grain boundaries, a peak in Al content was also observed at the boundaries.

These EDAX (figure 4.30) and EPMA (figures 4.29 and 4.31) results suggest that under the given hot pressing conditions though a reasonably good chemical homogeneity in hot pressed compacts occurred at the macro-level, there existed micro-level chemical inhomogeneities within some grains. Such micro-level inhomogeneities occurred because there existed a local variation in the progress of the diffusion process. Thus, while in some regions complete chemical homogenisation occurred with the development of a lamellar microstructure, a gradient of Al content existed across grains with traces of Al at their cores in other regions. Moreover, the sudden increase in composition at the grain boundary suggests the presence of iron aluminide particles at the grain boundary from which Al is diffusing into the iron particle.

From the above observations the following mechanism can be put forward for densification and development of microstructure during hot pressing of iron-iron aluminide powder mixture:

During initial stages of hot pressing the particles are pressed against each other while the temperature of the system is not high enough. Under such conditions neighbouring aluminide particles, because of their brittle nature, get fractured leading to finer particles. These fractured particles concurrently rearrange themselves under the

applied load resulting into a better packing. Subsequently, with the rise in temperature of the system the yield strength of iron decreases leading to the plastic flow of iron particles under the increased load. Iron particles thus flow plastically and fill the pores present in between particles. The increased number of elongated grains, which were often observed with the increase in iron content of the powder mixture, can thus be understood.

The diffusion of Al into the iron particles at higher temperatures gets enhanced with the better packing of particles. Portions of the hot pressing compact, which owing to the non-uniformity of the applied pressure do not possess good inter-particle contacts, undergo slower diffusion kinetics. Therefore a composition gradient is found in some regions.

Iron particles surrounding aluminide particles transform to aluminide particles due to the diffusion of Al and may undergo their fracture during further pressing [figures 4.25(a) and (b)]. Therefore, (i) fracturing and rearrangement of aluminide particles in the very early stages of hot pressing, (ii) plastic flow of iron particles to fill up neighbouring pores, (iii) diffusion of Al in Fe particles through the existing as well as newly formed Fe-aluminide interfaces gives rise to full density iron aluminide microstructures in hot pressed compacts. However, results of the present study indicate that more uniform full-density aluminide microstructures in hot pressed compacts can be obtained

**Table 4.5** Compression Test results of hot pressed samples

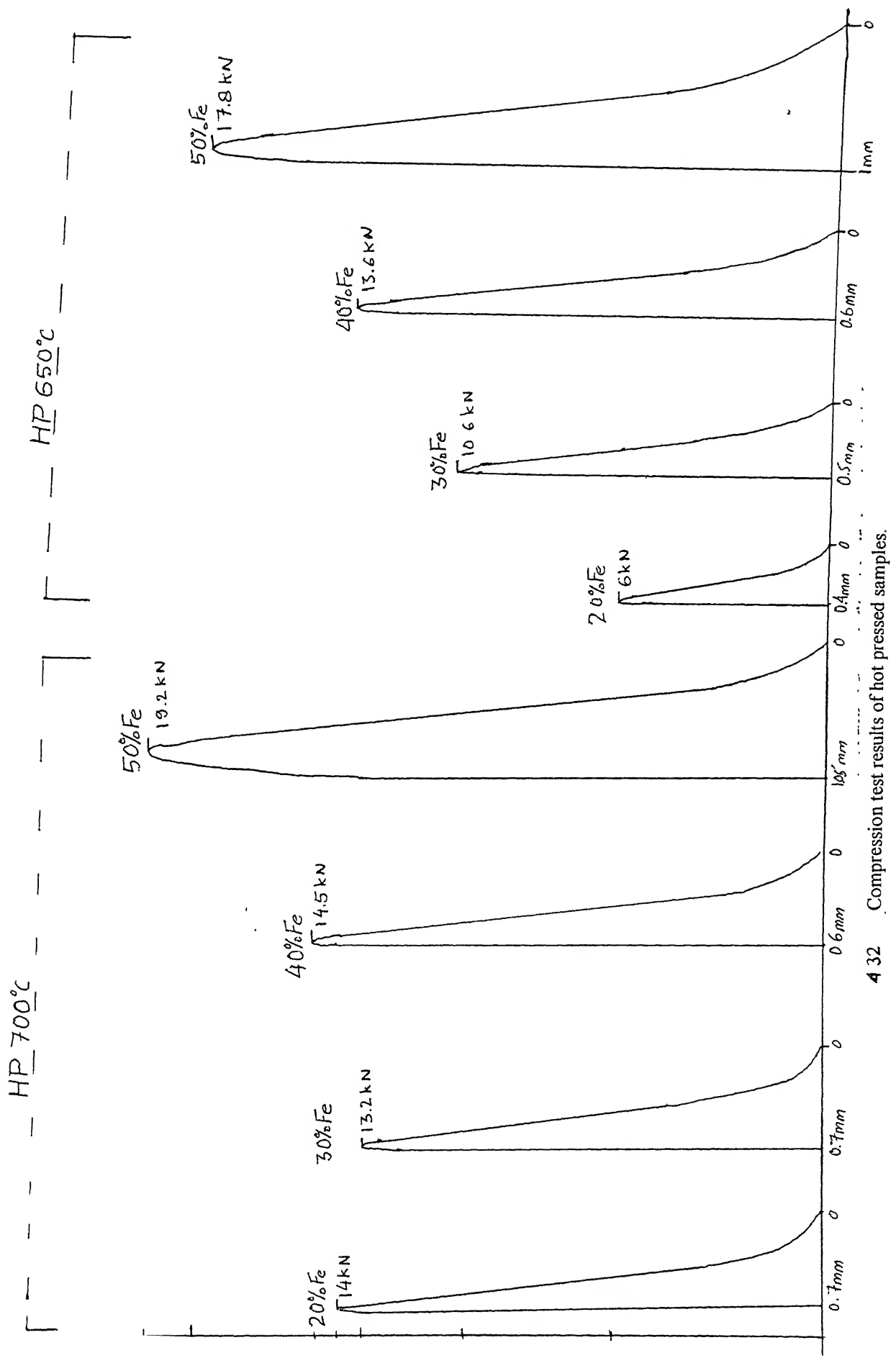
S.No.	%Fe	Compression Strength(MPa)	
		$650^{\circ}\text{C}$	$700^{\circ}\text{C}$
1	20	69.33	160.61
2	30	122.48	152.53
3	40	157.15	167.55
4	50	205.68	220.70

either by increasing the hot pressing time itself or adding another step of high-temperature homogenizing annealing in the processing route.

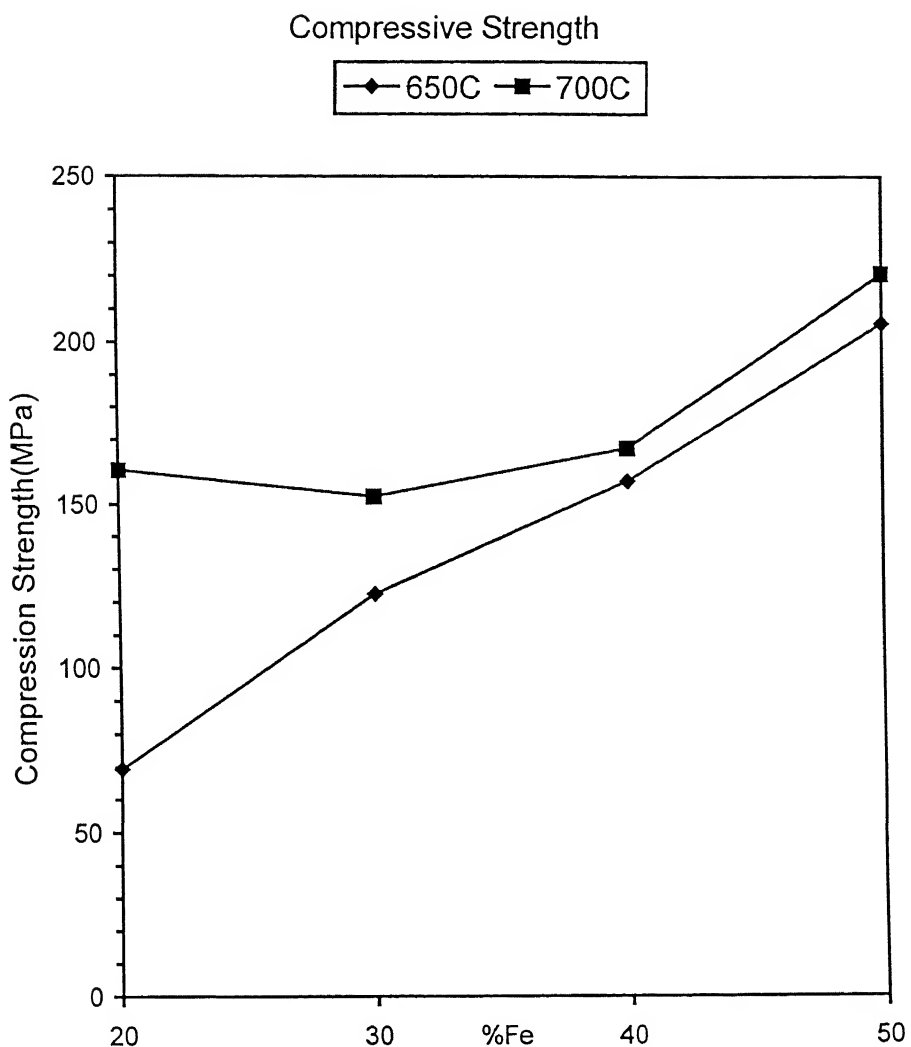
#### 4.4.4 Compressive Strength of Hot Pressed Compacts:

Due to the limited availability of iron aluminide powder, room temperature compression tests could be done on samples prepared at the hot pressing temperatures of 650°C and 700°C only. Thus, as indicated by X-ray diffraction results shown in table 4.4, the samples for compression tests comprised of  $Fe_2Al_5$ ,  $FeAl_2$  and Fe in varying amounts and therefore represented iron-iron aluminide composites. These tests were done at the cross-head speed of 0.2 mm/min. Typical stress-strain curves obtained from compression tests done on samples hot pressed at 650°C are shown in figure 4.32. It is clear from these curves that while the sample containing 20% Fe exhibited a totally brittle behaviour, the hot pressed compact made with 50% Fe shows some amount of ductility before fracturing. Further, though no separate tests were done to measure the toughness of iron-iron aluminide composites, areas under compressive stress-strain curves for various iron contents clearly indicate that their toughness increases as the Fe content increases in the starting iron-iron aluminide powder mixtures.

Compression strength of hot pressed iron-iron aluminide composites containing 20%, 30%, 40% and 50% Fe in the starting iron-iron aluminide powder mixtures, calculated from the compression test data, is shown in table 4.5 and figure 4.33. As shown here, while the compressive strength of composites prepared by hot pressing at 650°C



4.32 Compression test results of hot pressed samples.



increased with increase in iron content, that of composites prepared by hot pressing at 700°C remains more or less constant up to the iron content of 40% and increases subsequently. Moreover these data also indicate that the composites prepared at higher hot pressing temperature, i.e. 700°C, show a higher compressive strength for all the compositions.

In principle, the strength of iron-iron aluminide composites is expected to increase by (i) decreasing their porosity content, (ii) increasing their aluminide content and (iii) achieving a finer distribution of the phases present in the material. The presence of a higher iron content in the starting iron-iron aluminide powder mixture improves its compressibility. The volume fraction of pores in compacts containing higher Fe content is therefore expected to be lower. Further, since the reduction of porosity in iron-iron aluminide powder compacts during early stages of hot pressing is achieved by the plastic flow of iron particles, the contiguity between aluminide and iron powder particles improves in powder mixtures containing higher iron content. This better contiguity leads to more efficient diffusion kinetics during later stages of hot pressing and hence a higher volume fraction of aluminide in the compact. The increase in strength of composites as a function of their iron content and the hot pressing temperatures used in the present study, namely 650°C and 700°C, can be understood in the above manner. However, strength levels obtained in composites containing less than 40% Fe and hot pressed at 700°C require further investigation.

As indicated by the shape of compression test curves, shown in figure 4.32, the iron-iron aluminide composites containing different iron contents underwent failure in different modes. Thus, while composites prepared from 20% Fe collapsed completely and became a powdery mass consisting of coarse lumps at the time of their failure, composites containing 40% and 50% Fe maintained their shapes and developed fine cracks at the time of their failure. Fractographs obtained from composites prepared from powder mixtures containing 20% and 50% Fe respectively are shown in figure 4.34(a) and (b). It is clear from these figures that while compacts containing 20% Fe failed by almost the intergranular fracture those containing 50% Fe underwent a mixed failure mode comprising of ductile fracture in some regions and brittle fracture in others. The ductile failure in some regions of 50% Fe composites may be attributed to the higher iron content present in hot pressed samples. The results of the compression tests therefore indicate that iron-iron aluminide composites of higher strength, higher toughness and better ductility can be prepared by hot pressing of iron-iron aluminide powder mixtures containing as high as 50% of iron in them.



Figure 4.34(a) Scanning electron photograph showing fracture surface in 40%Fe sample hot pressed at 700°C



Figure 4.34(b) Scanning electron photograph showing fracture surface in 50%Fe sample hot pressed at 700°C

### CONCLUSIONS

- (1) Single/multiple phase iron aluminide as well as iron-iron aluminide composites can be prepared by the P/M processing of mixture of iron and prealloyed iron aluminide powder containing  $Fe_2Al_5$  and  $FeAl_2$  intermetallic phases.
- (2) Compressibility of Iron aluminide is very poor and compacts made by its cold pressing suffer from lamination defects. The compressibility of the aluminide powder significantly improves by the addition of iron above 12% by weight in the powder mixture.
- (3) For the particle sizes of the powders used in the present study i.e. iron aluminide particles with an average size of about 10  $\mu m$  and iron powder particles with an average size of about 100  $\mu m$ , the porosity in iron-iron aluminide green compacts can be decreased by increasing the iron content of the powder mixture up to 50 wt%.
- (4) Sintering behaviour of iron aluminide powder is very poor which can be improved by iron additions.
- (5) Hot pressing is found to be a more suitable P/M route than that involving cold pressing and sintering for the preparation of fully dense microstructures of single/multi-phase iron aluminide and iron-iron aluminide composites.

(6) The mechanism of densification and microstructural evolution during hot pressing of iron-iron aluminide powder mixtures involves the following stages:(i) fracturing and rearrangement of aluminide particles in the very early stages of hot pressing, (ii) plastic flow of iron particles to fill up neighbouring pores during further heating of the compact and (iii) at higher temperatures diffusion of Al from iron-aluminide particle into Fe particles through the existing as well as newly formed Fe-aluminide interfaces giving rise to evolution of equilibrium phases with full density microstructures.

(7) Iron-iron aluminide composites can be developed from powders containing up to 50 wt% Fe by their hot pressing up to  $700^{\circ}\text{C}$  under the present experimental conditions.

(8) Single-phase FeAl compacts with full density microstructures can be developed by hot pressing of 15 wt% Fe–iron aluminide powder mixture at the temperature of  $800^{\circ}\text{C}$ . On the other hand,  $\text{FeAl}_2$ -FeAl two-phase iron aluminide compacts can be obtained by the hot pressing of 40 wt% Fe-iron aluminide powder mixture by its hot pressing at the temperature of  $800^{\circ}\text{C}$  under the present experimental conditions.

(9) Compressive strength and toughness of iron-iron aluminide composites prepared by hot pressing increases with increase in the iron content of the initial powder mixture.

(10) Hot pressing at  $700^{\circ}\text{C}$  provides better compressive strength to iron-iron aluminide composites of all compositions than that at  $650^{\circ}\text{C}$ .

- (11) Application of the Iron-Iron aluminide composite is limited to the low temperatures since at higher temperature the diffusion of Al from iron aluminide particles will tend to change the initial composition of the material.
- (12) By proper selection of initial composition of the powder mixture, fully dense compacts of desired final composition, in terms of phases present, can be prepared by hot pressing route.

## CHAPTER 6

### SUGGESTIONS FOR FUTURE WORK

Cold pressing and Sintering route does not seem to be suitable for the preparations of materials based on iron aluminide from prealloyed iron aluminide powder. Therefore, future research on this material should involve primarily hot pressing and hot isostatic pressing P/M processes. Following suggestions in this direction can be given for the research on iron aluminide :

- 1) Hot pressing and Hot isostatic pressing in more controlled apparatus for other temperatures and times of sintering may be done to get composites of different compositions and fully dense compacts of a particular iron aluminide phase or a mixture of aluminide phases.
- 2) Modelling of the process can be done to predict the product compositions by utilising the data obtained from the above experiments.
- 3) Few alloying additions suggested in the literature can be made in the initial powder mixture for the improvement in the properties of the product.
- 4) More experiments are needed to understand the effect of hot pressing temperature and iron content on the strength and toughness of the material thus prepared.

## REFERENCES

1. N. S. Stoloff; "Ordered Alloys – Physical Metallurgy and Structural Applications" ; Int. Met. Review ; 29 (1984); pp123-135.
2. Gerhard Sauthoff ; " Intermetallic Phases – Material Developments and Properties" ; Z.Metallkde.; 80(1984); pp-337-344.
3. C.T.Liu, J.O.Stiegler; "Ordered Intermetallic"; Properties and Selection : Non-ferrous Alloys and Special Purpose Materials; Metal's Handbook; vol.3; 10<sup>th</sup> ed; ASM International; 1990; p-913.
4. C.T.Liu, K.S.Kumar; "Ordered Intermetallic Alloys,Part I, Nickel & Iron Aluminides" ; JOM; 1993 ; p-38.
5. C.T.Liu, K.S.Kumar ; "Ordered Intermetallic Alloys , Part II , Silicides, Trialuminides and Others"; JOM ; June 1993 ; p-28.
6. Hugh Baker; "Alloy Phase Diagram"; ASM Handbook ; vol. 3 ; 1992; p-2.44.
7. R.A.Buckley, H.jones, C.M.Sellers; "Structure and Properties of Ordered Intermetallics Based On The Fe-Al System"; ISIJ International; vol.31; 1991; no.10; p-1113.
8. U.Prakash, R.A.Buckley, H.jones, C.M.Sellers; "Structure and Properties of Ordered Intermetallics Based On The Fe-Al System"; ISIJ International; vol.31; 1991; no.10 ; p-1113.

9. C.G.McKamey, J.A.Herton, C.T.Liu; "High Temperature Ordered Intermetallic Alloys II" ; ed. by N.S.Stoloff, C.C.Koch, O.I.Zumi, C.T.Liu; MRS Symp. Proc. ; vol.81; MRS; Pittsburgh;1987 ;p-32.
10. C.C.Koch, C.T.Liu, N.S.Stoloff; eds., High Temperature Ordered Intermetallic Alloys (Pittsburgh, PA:MRS,1985).
11. N.S.Staloff et al; eds., High Temperature Ordered Intermetallic Alloys II (Pitsbergh,PA:MRS,1987).
12. C.T.Liu et al; eds., High Temperature Ordered Intermetallic Alloys II; (Pitsbergh,PA:MRS,1987).
13. C.G.McKamey et al; J. Mater.Res.; 6(1991) ; p-177.
14. J.H.Devon; "Oxidation of High Temperature Intermetallic" ; ed. T.Grodstein, J.Doychak; (Warrendale, PA:TMS , 1989); p-107.
15. D.G.Morris, M.Nazmy, C.Noreda; "Creep Resistance In A New Alloy Based On  $Fe_3Al$ " ; Scr. Met. et Mater. ; vol.31 ; no.2 ; 1994 ; p-173.
16. I.Jung, M.Rudy, G.Sauthoff; "High Temperature Ordered Intermetallic Alloys II; ed. By N.S.Stoloff, C.C.Koch, O.I.Znmy, C.T.Liu; MRS Symp. Proc. ; vol.81; MRS; Pittsburgh(1987) ; p-321.
17. Z.Zhonghur, S.Yanashan, G.Jun; "Effect of Niobium Addition On The Mechanical Properties of  $Fe_3Al$  Based Alloys" ; Scr.Met. et Mater.; vol.33 ; no. 12; 1995; p-2013.
18. J.D.Whitenberger; "The Influence of Grainsize and Composition On Slow Plastic Flow In FeAl Between 1100 to 1400 K"; Mat. Sc. & Engg.; vol.77 ; 1986 ; p-103.

19. N.S.Stoloff, G.E.Fuchs, A.K.Kuruvilla, S.Cho; "High Temperature Ordered Intermetallic Alloys II"; ed. by N.S.Stoloff, C.C.Koch, O.Izumy, C.T.Liu; MRS Symp. Proc.; vol.81; MRS; Pittsbergh; 1987; p-247.

20. X.Wang, J.V.Uood;"Role of Nickel In  $Fe_3Al$  Intermetallic Compound Formation"; Powder Metallurgy; vol.38; no.1; 1995; p-59.

21. S.Yangshan, Y.zhengium, Z.Zhonghur, H.Haibo; "Mechanical Properties of  $Fe_3Al$  based Alloys with Cerium Addition"; Scr. Met. et Mater.; vol.33; no.5; 1995 ; p-811.

22. W.B.Kerr; "Fracture of  $Fe_3Al$ "; Met. Trans. A; vol.17A; Dec.1986. p-2298.

23. V.K.Sikka, C.G.McKamey, S.Viswanathan; "development and commercialization Status of  $Fe_3Al$  Based Intermetallic Alloys"; Structural Intermetallics, ed. by C.T.Liu, N.S.Stoloff, C.C.Koch; The Mineral, Metals & Materials society ;1993 ; p-433.

24. H.J.Beattic, F.L.Versnyder; Trans. ASM; vol.45; 1953; pp-397 423.

25. Dr. Phil. Max Mansan; "Constitution of Binary Alloys"; ed. by T. Rer. Nat. kurt. Anderko; McGrawhill Book Company, INC; 1958.

26. E.H.Hollingsworth, G.R.Frank,Jr., R.E.Willet; Trans. AIME; 224; 1962; pp188-189.

27. D.U.Rabin, R.N.Wright; "Synthesis of Iron Aluminide  $Fe_{3-x}Al_x$  Elemental Powders, Reaction mechanism and Densification Behavior"; Met. Trans. A; vol.22a; Feb.1991; p-277.

28. D.K.Mukhopadhyay, C.Suryanarana, F.H.fores; Structure Evolution in Mechanically alloyed al-Fe Powders.”

29. F.H.Fores, C.Suryanarayana, P.R.Taylor, C.M.Ward-Close, and P.Goodwin; “Syntesis of Advanced Light Weight Metals by Powder Metallurgy techniques”.